To Popper's World 3

Abstract

Results of the characterisation of three different pixel detectors are presented. The first is an energy resolving detector (ERD1) which has been characterised using laboratory sources and the synchrotron radiation source (SRS) at Daresbury. The ERD1 is a 16 by 16 array of 300 μm by 300 μm square pixels, the detector is 300 μm thick Si and is bump-bonded using gold studs to the RAL PAC5 read out. Energy spectra and diffraction lines acquired at the SRS are presented and show the imaging and simultaneous spectroscopic capabilities of the ERD1. The energy resolution was investigated using X-rays of energies between 6 and 60 keV from laboratory sources. The achieved full-width-at-half-maximum (FWHM) of the photo peaks is in the range of 300 eV to 500 eV with an electronic noise of 227 ± 43 eV. Charge sharing was investigated for different energy X-rays and is shown to be significant with up to around 10 % of events sharing some charge.
The second detector is a large area detector (LAD1). It is based on single photon counting and is designed for imaging in synchrotron radiation applications. Results of tests performed with a single chip module at the Daresbury SRS are presented. The detector is 300 μm thick Si with 150 μm by 150 μm pixels bump-bonded to an (RAL ALADIN) array of 64 by 64 read out channels. The spatial resolution was determined using the modulation transfer function (MTF) with a result of (5.1 ± 0.1) lp/mm at an MTF value of 0.3. Theoretical studies of the spatial resolution predict a value of 5.3 lp/mm. The image noise in photon counting systems is investigated theoretically and experimentally and is shown to be given by Poisson statistics. The rate capability of the LAD1 was measured to be 250 kHz per pixel.
Theoretical and experimental studies of the difference in contrast for ideal charge integrating and photon counting imaging systems were carried out. It is shown that the contrast differs and that for the conventional definition (contrast = (background - signal)/background) the photon counting device will, in some cases, always give a better contrast than the integrating system.

Simulations in MEDICI are combined with analytical calculations to investigate charge collection efficiencies (CCE) in semiconductor detectors. Different pixel sizes and biasing conditions are considered. The results show charge sharing due to the limited mean free drift lengths of the charge carriers, the improvement of the CCE in unipolar detectors with decreasing pixel size and the "small pixel effect" which shows the improved CCE of the photo peak with smaller pixels.
The third detector is a graphite pixel detector for ion beam profiling. The system was tested in the ion implanters at the University of Salford and Surrey. Results are presented showing real time profiling of the ion beam and the measurement of the beam current. The secondary electron emission was qualitatively measured for different beam energies and different positions on the detector. The loss of secondary electrons follows the profile of the detector and increases with higher energy ions.

Acknowledgements

This work was only possible due to the vital help of a number of people.
My sincere thanks first of all go to my supervisor **K. M. Smith**. I have enjoyed an exceptionally positive time in his group. I thank him for his interest in my work, the educative discussions and not least for the freedom and the possibilities I was given to carry out my research.
Very many thanks, also, to **M. Rahman**, my second supervisor, for his support and for offering me the work on the ion beam detector. I have greatly benefited from his amazing knowledge in physics and electronics and his willingness to answer all my questions.
Without the support of **P. Seller** this work could not have been done. I thank him sincerely for providing us with his detectors and involving me in their characterisation. I have thoroughly enjoyed the trips to RAL and Daresbury, which have been hugely successful and provided main parts of the data for this work.
My colleagues here must be given credit for putting up with me! I greatly appreciate the discussions I have had with **V. O'Shea** and **R. L. Bates** and thank them for the great time I enjoyed. **K. Mathieson** has been most closely attached to my work. Working with him has been immensely profitable for me. I must thank him for a lot more than the lessons in simulation.
I also thank my office mates for their support and company. I was by far the least in the room of gods and kings. **S. Devine** and **P. Roy** must together be the ideal comrades imaginable. I have also enjoyed the company of **J. Marchal** on our trips to Salford and Surrey. Working with him has been very fruitful and his involvement in the ion beam project was vital to the success of this project.
Thanks go also to **A. Meikle** for the preparation of detectors and the wire bonding and to **I. McVicar** for the photographs. **C. MacIntyre** needs a special mention for her caring and help with any problem I had. I also wish

to thank a number of people which have helped and supported me. These include **F. Doherty**, **D. Livingston**, **P. Thornton**, **J. Melone**, **J. Watt**, **C. Whitehill**, **D. Davidson** and **M. Abdallah**.
I have also benefited from the excellent work of our Head of Dept. **D. Saxon**. His competence and expertise have been noticeable at all levels.

Declaration

Except where explicit reference is made to the work of others, this dissertation is the result of my own work. None of this material has been submitted for any other degree at the University of Glasgow or any other institution.

M. S. Passmore

Contents

List of Figures

List of Tables

Chapter 1

Introduction

Most detectors are based on the electromagnetic interaction, and are used to extend the range of electromagnetic radiation we can perceive. Film and gaseous detectors such as the Geiger-Müller counter were the first to be used. These are now increasingly challenged by solid state detectors, which allow a better energy resolution, and offer benefits from the recent advances in semiconductor processing and material growth. The areas of applications range from the basic sciences such as physics, chemistry, biology and medicine, to military (infra-red sensors), industrial (e.g. quality assurance) and civil requirements (e.g. baggage control systems). Detector characteristics of interest may be the frequency (energy resolution), spatial distribution and range of intensity of the radiation to which they will respond.

Our eye is an example of an excellent detector with an amazing performance in all three of these aspects, within its sensitive energy range. It has a high spatial resolution (pixel size $\approx 2\ \mu$m), is sensitive to different energies (colour vision) and performs parallel processing and data reduction within the sensor (retina) [Lit97].

Hybrid pixel detectors are so far the closest imitation, although still barely comparable in performance. Each pixel can be sensitive to different energies and some parallel processing and data compression can be achieved on the read out chip. A high spatial resolution (pixel sizes < 0.1 mm) can be combined with a frame read out rate up to a couple of kHz (64 by 64 elements) and noise $< 100\ e^-$ r.m.s. [Medi2]. The separation of the read out chip and the sensor allows the freedom of choice of the detector material, while taking full advantage of the progress in silicon technology. It also allows the independent optimisation of the sensor and read out, providing a higher yield of the final system. Some disadvantages must nevertheless be taken into account, such as the high fabrication costs (state-of-the-art silicon technology for the read-out and detector plus additional costs of bump-bonding)

and the technical difficulties of producing large areas. (Read out ICs are typically limited to a size of $\approx$ 1-2 cm^2).
The main part of this work is concerned with hybrid semiconductor pixel detectors for X-ray detection. Accordingly the second chapter is devoted to the physics of X-ray interactions and semiconductors as far as is of interest for detectors. The five sections follow the generation of a signal in a semiconductor detector, starting from the interaction of the primary photon with the detector and the creation and distribution of created charge. Some common detector materials (Si, GaAs and CdZnTe) are introduced and some of their properties briefly discussed. The collection of this signal charge and the vital processes involved in this are discussed in the following section. A brief description of the electronics, which are commonly employed in processing the signal, is given before the final part introduces noise.
Two hybrid semiconductor pixel detectors are described and characterised in this work; one is designed for spectroscopic, the other for imaging applications. Both these systems are introduced in chapter 3.
The spectroscopic detector, the ERD1 (**E**nergy **R**esolving **D**etector), is characterised in chapter 4. It is intended for low noise, high rate spectroscopy at room temperature. Detectors with comparable energy resolution are often cooled (Ge or Li drifted Si detectors [Kno00]) which adds substantial complexity, size and cost to the system. Current room temperature spectroscopic detectors are commonly based on monolithic technologies (CCDs or drift detectors [Lec01]) and do not achieve the high rate due to slower read out.
The second pixel detector described here is the LAD1 (**L**arge **A**rea **D**etector), which is characterised in chapter 5. It is designed for X-ray imaging and is based on single photon counting. The detectors use a fan-out to reduce the dead space around the edge of the read out chips. It is the first of its kind designed to cover a large area (30 cm by 30 cm). It operates at room temperature, has a counting rate of up to several giga-counts per cm^2 and second and a potential frame rate of 2 kHz. Its advantages over existing large area X-ray imaging devices, such as amorphous silicon arrays [Sha01], are the substantially higher frame rate and the data analysis performed within each pixel ("smart pixels"). Other existing large area detectors use indirect conversion of the X-rays leading to loss of energy and spatial resolution.
Chapter 6 is split into two sections. The first discusses the difference in contrast between ideal single photon counting and charge integrating imaging systems. The second section is based on simulations and analytical calculations and discusses the small pixel effect and related phenomena.
The last part, chapter 7, is concerned with a graphite pixel detector, which is designed for real time ion beam profiling. This prototype detector is related to semiconductor imaging devices only through the read out electronics,

which is based on a charge integrating pixel ASIC. The advantages offered by such a detector are real time acquisition and true imaging of the beam profile. Current detectors are based on a single read out chain, such as a Faraday cup or wires and require the beam profile to be reconstructed from a scan.

Chapter 2

Semiconductor Detectors

This chapter is concerned with the physical processes which lead to the detection of particles. It is split into five sections, the first describes the interaction of photons and the trace they leave, by which they can be identified. The second section is devoted to semiconductor detectors and the collection of charge. In section three the generation of the signal is discussed. Section four introduces the electronics that are commonly used for reading out and amplifying the signals. The final section is concerned with the definitions and sources of noise.

2.1 Interaction of Photons and Electrons with Matter

The interactions for the particles of interest (X-rays and therefore electrons) will be introduced by focusing on the relevant aspects for semiconductor detectors.
The photo-electric effect dominates in the energy range of interest of up to about 100 keV. The Compton effect contributes significantly at the higher energies, while pair production lies well beyond the energies considered here and will not be discussed. As the absorption of photons leads to the emission of electrons, their interactions are included in this section.

2.1.1 Absorption of Photons

Photons undergo point interactions, therefore their absorption has an exponential dependence on the absorber thickness. The intensity I_0 of a beam of photons is reduced by a material of thickness x, density ρ and a material and energy dependent absorption coefficient α according to [Dys90]

$$I(x) = I_0 \, e^{-\alpha\rho x}. \tag{2.1}$$

The absorption coefficient is the sum of all possible contributions to the photon's interaction possibilities, i.e. $\alpha = \alpha_{\mathrm{Photo}} + \alpha_{\mathrm{Compton}} + \alpha_{\mathrm{Pair}}$.
For a compound material $X_x Y_y$ α is given by [Lau95]

$$\alpha(X_x Y_y) = \frac{\alpha(X)\, A_x + \alpha(Y)\, A_y}{x\, A_x + y\, A_y} \tag{2.2}$$

where A_x (A_y) is the molar mass of the element X (Y) and x (y) is its proportion in the compound material. Equation 2.2 can be extended to any number of elements.

2.1.2 Photo-Electric Effect

A photon interacting with an electron and transmitting all its energy E_γ vanishes. The electron can be ejected from the atom and is referred to as the photo-electron. If the binding energy of the electron is E_{b} the photo-electron will have the energy [Tai80]

$$E_{\mathrm{e}} = E_\gamma - E_{\mathrm{b}}. \tag{2.3}$$

To conserve momentum the atom from which the electron is emitted must recoil. This leads to a high probability of ejecting inner shell electrons which interact more strongly with the nucleus and can therefore more easily transfer momentum[1]. Most likely an electron will be emitted from a shell with energy levels closest to (but below) the photon energy.
The emission of an inner shell electron leads to a cascade of relaxation processes, the vacant state is filled by an electron from a higher level leaving its original state empty and so forth. The electrons moving into lower energy states can lose the excess energy by emitting characteristic photons (secondary photons).
From the detector point of view two things are of particular interest:

1. **Escape Peak:** A secondary photon depositing its energy outside the active area of interest is lost. Assuming the rest of the initial photon's energy is collected, the lost secondary photon gives rise to a lower peak in the energy spectrum which is referred to as "escape peak".

[1] The energy transfer can be neglected since the mass of the nucleus (or crystal lattice) is far greater than that of the electron.

2. **Photo-electron:** The photo-electron generates signal, therefore the distance it travels and the angle at which it is emitted influence the spatial distribution of the signal. This is of interest when considering effects like charge sharing.

The relative proportion of the escape peak depends mainly on the geometry and material of the detector; the position is entirely material dependent. The direction in which the photo-electron is emitted can be calculated using the Born approximation (i.e. the binding energy of the electron is assumed to be negligible). For the K shell which gives the greatest contribution (assuming the photon is sufficiently energetic), the differential cross section in dependence of the azimuthal angle Φ and the longitudinal angle Θ is given by [Spr50]

$$\frac{d\sigma(\Theta,\Phi)}{d\Omega} = r_0^2\,\frac{Z^5}{\alpha^4}\left(\frac{m_{\mathrm{e}}c^2}{E_\gamma}\right)^{7/2} 4\sqrt{2}\,\frac{\sin^2\Theta\,\cos^2\Phi}{\left(1-\cos\Theta\,\sqrt{1-(E_{\mathrm{e}}/m_{\mathrm{e}}c^2+1)^{-2}}\right)^4} \tag{2.4}$$

where

r_0	=	classical electron radius	=	$e^2/4\pi\epsilon_0\,mc^2$	=	$2.818\cdot 10^{-15}$ m
Z	=	atomic number of absorbing atom				
α	=	fine structure constant	=	$e^2/4\pi\epsilon_0\,\hbar c$	=	$1/137$
m_{e}	=	electron rest mass	=	511 keV/c^2	=	$9.110\cdot 10^{-31}$ kg
c	=	speed of light in vacuum			=	$2.998\cdot 10^8$m/s

For the applications of interest the photons are not polarised, hence the Φ dependence can be integrated out. The Θ dependence is plotted for energies of 10 keV and 100 keV in fig. 2.1.

From the detector point of view it is of interest, that the photo-electron has a large probability of being emitted sideways with respect to the direction of the photon. Therefore the charge-weighted mean position of the generated signal does not in general correspond to the point where the photon was absorbed. The error in the position is in the order of several μm (see section 2.1.4).

2.1.3 Compton Effect

The scattering of photons occurs most probably with loosely bound, outer shell electrons. This justifies the assumption that the interaction takes place with a free electron. Relativistic calculations using energy and momentum conservation describe the relation between the initial photon energy E_γ, the energy of the scattered photon E'_γ and the scattering angle Θ [Kra88].

$$E'_\gamma = \frac{E_\gamma}{1+(E_\gamma/m_{\mathrm{e}}\,c^2)\,(1-\cos\Theta)} \tag{2.5}$$

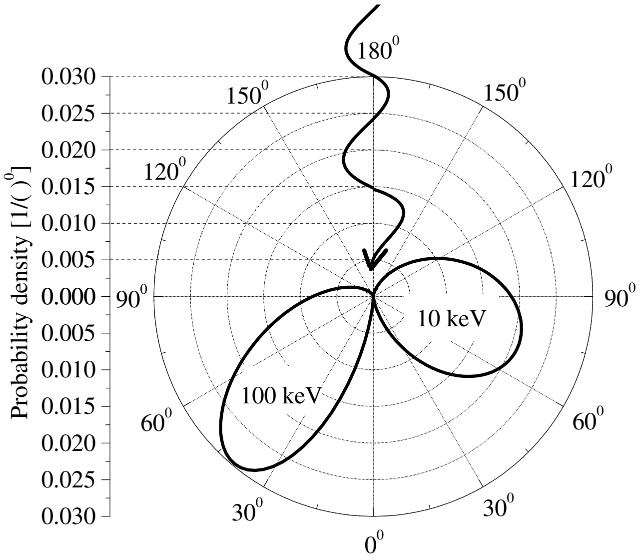

Figure 2.1: Polar plot of the probability of the direction in which the photo-electron is emitted. At low energy it is most likely to be released sideways, with increasing photon energy the likelihood of forward emission increases.

where m_e is the electron rest mass and c the speed of light.
Backscattered photons possess the minimum possible energy, i.e. $\Theta = \pi$ minimises equation 2.5 leading to

$$E'_{\gamma,\mathrm{min}} = \frac{E_\gamma}{1 + 2\,E_\gamma/m_\mathrm{e}\,c^2}. \tag{2.6}$$

The energy the electron acquires is $E_\mathrm{e} = E_\gamma - E'_\gamma$ and hence the maximum electron energy $E_\mathrm{e,max}$ is directly determined by equation 2.6. $E'_{\gamma,\mathrm{min}}$ and $E'_\mathrm{e,max}$ are plotted in fig. 2.2 for energies up to 100 keV. The shaded areas show the possible energies the scattered photon and emitted electron can acquire. The relation between the angle Θ at which the photon is deflected and the angle Φ at which the electron is emitted, is given by [Spr50]:

$$\tan\Phi = \frac{1}{1 + E_\gamma/mc^2}\tan\frac{\Theta}{2} \tag{2.7}$$

So the electron is always released with a forward component and can never have a velocity component opposite to the incoming photon's direction.
The differential cross section for Compton scattering can be calculated per electron [Kra88]. The result is the Klein-Nishina formula:

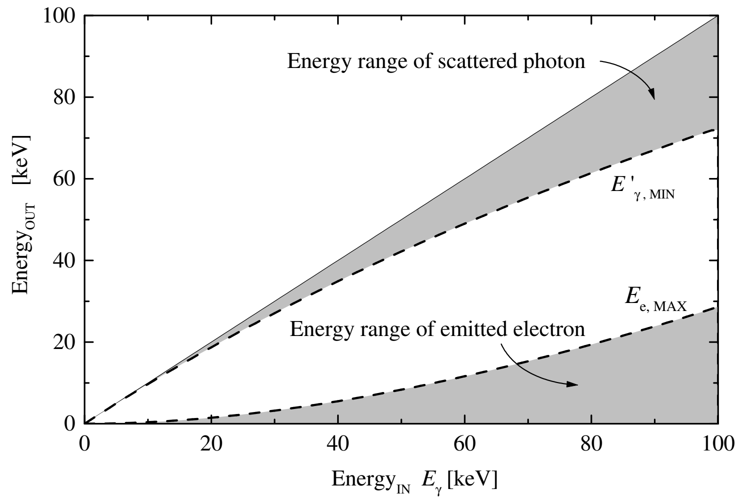

Figure 2.2: The plot shows the energy range the scattered photon and the emitted electron can acquire. The dashed lines show the minimum and maximum energy of the scattered photon and emitted electron respectively.

$$\frac{d\sigma(\Theta)}{d\Omega} = r_0^2 \left(\frac{1}{1 + E_\gamma / m_e c^2 \, (1 - \cos\Theta)} \right)^3 \cdot \left(\frac{1 + \cos^2\Theta}{2} \right) \cdot \left(1 + \frac{(E_\gamma / m_e c^2)^2 \, (1 - \cos\Theta)^2}{(1 + \cos^2\Theta) \left((1 + E_\gamma / m_e c^2) \, (1 - \cos\Theta) \right)} \right) \tag{2.8}$$

The angular dependence of the scattered photon is plotted for 1 and 100 keV in fig. 2.3.

At low energies the photon is scattered preferentially in the forward and backward directions, with increasing energy the forward direction prevails.
Depending on the detector application some consequences are:

1. **Energy resolving detectors:** For a given photon energy the Compton spectrum can be calculated from equations 2.5 and 2.8. An example for 100 keV photons is shown in fig. 2.4. The Compton edge reflects the maximum energy the electron can acquire, given by equation 2.6. For energy resolving detectors the Compton effect is not desirable. The energy of the initial photon is split between the electron and the scattered photon which may travel outside the area where the electron signal is generated. The energy information is likely to be lost and a Compton background is observed,

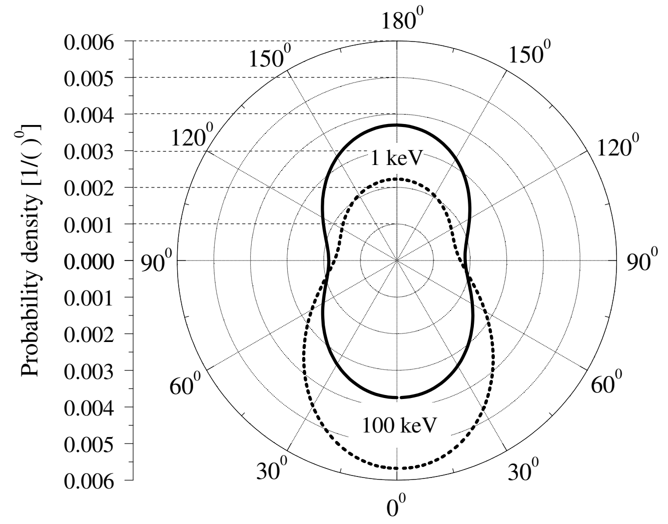

Figure 2.3: Polar plot of the probability of the direction in which the scattered photon is deflected. Forward and backward scattering are dominant and equally likely at low energies. The forward direction prevails for higher energies.

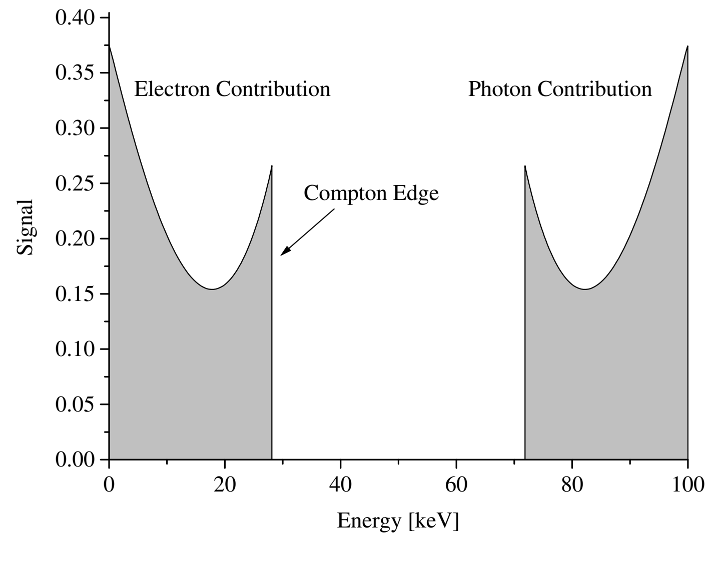

Figure 2.4: Theoretical Compton spectrum for 100 keV photons. The Compton edge is due to the high probability of a process with the maximum possible energy transfer.

as shown in fig. 2.4.

2. **Imaging detectors:** The interaction point is the information of interest. The scattered photon carries most of the energy (fig. 2.4) and may be lost or absorbed in another pixel. Therefore Compton scattering has undesirable effects in imaging systems.
   A beneficial point is that the scattered photon is preferentially deflected in the forward or backward direction, thus maintaining the position information.

Thomson Scattering

Thomson or Rayleigh scattering is a coherent process. The photon changes its direction without losing any energy. The cross-section for this process is significantly lower than for the dominant interaction (photo-effect at lower energies, Compton-effect at higher energies). The fraction of coherent scattered events, normalised to the total number of interactions is plotted in fig. 2.5. Of all interaction processes coherent scattering will contribute less than 14 % at maximum. All the data in

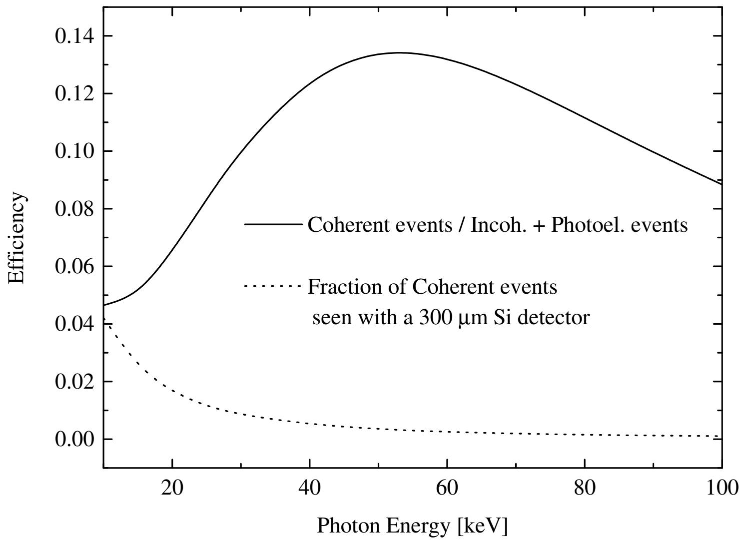

Figure 2.5: The solid line shows the coherent scattering fraction, which is always less than 14 % of all interactions. The dotted line is the fraction of coherent events that will be "seen" in a 300 μm thick Si detector, i.e. the coherent scattered photon must be absorbed in order to be of any significance.

fig. 2.5 are calculated for a 300 μm thick Si detector. The lower, dotted line shows the fraction of registered events which will have undergone a coherent scattering

process. For the calculation it was assumed, that the coherently scattered photon must be absorbed in 300 μm Si. This approximation is justified by the fact that forward and backward scattering are most likely.
Since the only relevant Thomson events are those for which the coherently scattered photon is absorbed, it is the lower, dotted line in fig. 2.5 that is relevant. Coherent scattering is negligible and will not be considered any further.

2.1.4 Electron Interactions

The specific energy loss of electrons (dE/dx) is described by the Bethe-Bloch formula [Fer86], the "dx" referring to the path length. The electron energies of interest are smaller than the photon energies considered and therefore less than 100 keV. At these energies the electrons follow erratic paths (multiple scattering), the Bragg distributions are folded along the electron's path and therefore the energy loss does not peak at a distance corresponding to the electron range from the emission point. Since the interest lies in the spatial distribution of the carriers, it is the range of the electrons that matters not their path length. The range is defined as the straight line distance between the electrons starting point and its final resting place.
The extrapolated range of electrons in Si, GaAs and CdTe is plotted in fig. 2.6. The material dependence is dominated by the different densities of the materials.

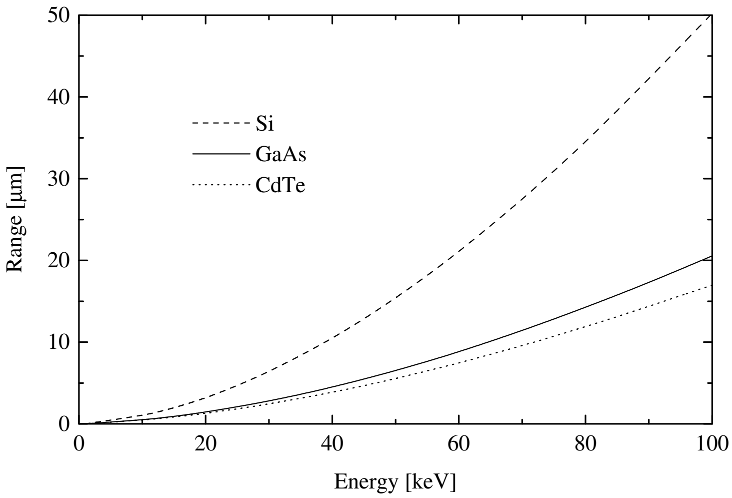

Figure 2.6: Range of electrons in Si, GaAs and CdTe for energies up to 100 keV.

For the electron energies of interest here the dependence on the Z/A ratio from

the Bethe-Bloch formula is significantly weaker. The data used for fig. 2.6 were extracted from ref. [NIST] and [Tab96].
At the electron energies of interest, the width of the volume in which the electron interacts is approximately 0.77 times the electron's range [Wit00].
Since the electron is generated by the interaction of a photon which is assumed to be non-polarised, the volume to be associated with one interaction is azimuthally symmetrical around the incident photon direction.
At the energies of interest the electron will lose virtually all its energy in collisions (at 100 keV radiative energy loss occurs at a level of 0.25 % [NIST]). Some of the collisions will ionise the material. For semiconductor detectors the average energy required to generate an electron hole pair is in the order of several eV (see table 2.1), so for the photon (and electron) energies of interest here up to around ten-thousand charge carriers are generated, typically, by a single photon.

2.2 Semiconductor Detectors

The aim of this section is to describes the physical processes that lead to an output signal in semiconductor detectors.

2.2.1 Reverse Biased and Photo-Conductivity Detectors

Whatever material is used, the signal generated by the particle to be detected is due to some distribution of electron hole pairs (e-h pairs). The number of e-h pairs is proportional to the energy of the incident particle. In order to retain this information it is beneficial[2] if all e-h pairs contribute fully to the output signal. The basic idea is to separate the carriers with an electric field before they recombine and drift them to either side of the detector, where the signal they generated can be amplified and further processed by read-out electronics. The challenge is to establish a suitable drift electric field inside the detector together with such conditions that the carriers do not get lost or are swamped by carriers from currents passing through the material.
Typical thicknesses of semiconductor detectors are several hundreds of μm for Si or GaAs and up to several mm for Cd(Zn)Te.[3]
The situation is the following:

[2]It is not necessary that all e-h pairs contribute fully to the signal in order to determine the correct energy. If a constant percentage of e-h pairs is always lost, then the calibration will change but no information is lost. However as noise is present in all systems, it is beneficial if no electrons or holes are lost.

[3]Since CdTe and CdZnTe are similar in several aspects, Cd(Zn)Te is used in contexts which are valid for both CdTe and CdZnTe.

Primary goal:

Collection of a maximum proportion of the generated charge in order to gain accurate information of the absorbed particle.
Reduction of undesirable effects of leakage currents and charge loss.

Challenges:

Reduction of leakage currents

To reduce currents the material must have as high a resistivity as possible. Two ways of achieving this are common: the material may naturally be highly resistive, thus an applied voltage will draw only a small current; or a reverse bias diode structure can be used.

Reduction of charge loss

Free carriers can be trapped or lost through recombination processes. Very high quality material is required to achieve a high collection efficiency. The distance the carriers travel (mean free drift length) is the vital parameter for the charge collection efficiency.

Leakage Currents

Some materials such as CdZnTe have naturally a high resistivity ($\approx 10^{10}$ Ωcm). By applying a voltage across such a material it acts as a resistor with the electric field constant over the whole detector. The current is given by Ohm's law. Detectors operating in such a way are referred to as photo-conductivity detectors[4]. Such a device is fully active since an electric field is present throughout the detector.
Reverse biased detectors make use of a diode structure, which can be a $p-n$ junction or a Schottky contact. The current-voltage ($I-V$) characteristics of these are given by[5] [Sze81]

$$I(V) = I_S\,(e^{qV/kT} - 1) \tag{2.9}$$

[4]This term originates from lower frequency light detectors. As the incoming light generates free carriers the resistivity is reduced. Measuring the resistivity (conductivity) of the detector relates to the amount of incoming light.

[5]The following assumptions are necessary in order to derive this equation:

1. The depletion zone is abrupt.
2. The Boltzmann approximation is valid (see [Sze81] chapter 1.4 and 2.4 for details.)
3. The injected minority carrier concentrations are small in comparison to the majority carrier concentrations.
4. No generation currents exist within the depleted region.

Parameter	Unit	Si	GaAs	CdZnTe
atomic number Z		14	31, 33	48, 30, 50
density ρ	g/cm^3	2.33	5.32	5.78
energy per e-h pair	eV	3.62	4.18	4.64
bandgap E_g	eV	1.12	1.42	1.57
electron lifetime τ_n	s	$> 10^{-3}$	10^{-8}	$3\,10^{-6}$
hole lifetime τ_p	s	$2 \cdot 10^{-3}$	10^{-7}	10^{-6}
permittivity ϵ		11.9	13.1	10.9
electron mobility μ_n	$cm^2/V\,s$	1400	8000	1000
hole mobility μ_p	$cm^2/V\,s$	480	400	100

Table 2.1: Semiconductor material parameters and values, according to references [Par00],[Sch95],[Sze81].

with

$$I_{S,p-n} = \frac{qD_p p_{no}}{L_p} + \frac{qD_n n_{po}}{L_n} \qquad \text{and} \tag{2.10}$$

$$I_{S,\mathrm{Schottky}} = A^{**}\, T^2\, e^{q\Phi_{\mathrm{B}}/kT} \tag{2.11}$$

for a $p-n$ junction and a Schottky contact respectively. A^{**} in equation 2.11 is the effective Richardson constant ([Sze81] page 254 - 262). The calculated value of A^{**} for electrons in GaAs and Si at 300 K are 4.4 $\mathrm{Acm^{-2}K^{-2}}$ and 96 $\mathrm{Acm^{-2}K^{-2}}$, respectively [Rho88].
In equations 2.10 and 2.11 q is the unit charge, p_{no} and n_{no} are the equilibrium minority carrier concentrations for the n and p regions, respectively. Φ_{B} is the Schottky barrier height, $D_{n(p)}$ is the diffusion constant and $L_{n(p)}$ is the diffusion length. For non-degenerate semiconductors (which is the case for detector material), the diffusion constant is given by equation 2.12. The diffusion length depends on the diffusion constant and lifetime τ of the carrier.

$$D_{n(p)} = \frac{kT}{q}\,\mu_{n(p)}, \qquad L_{n(p)} = \sqrt{D_{n(p)}\,\tau_{n(p)}} \tag{2.12}$$

kT is the product of the Boltzmann constant k and the temperature T; at room temperature the value is $kT = 0.0259$ eV.
Some material parameters, including those used in equations 2.9, 2.10 and 2.11 are given in table 2.1.

According to equation 2.9 the current under reverse bias condition ($V < 0$) will saturate ($I(V) = I_S$ for $V \to -\infty$). Real devices show an increase in current with increasing reverse bias. Effects leading to excess current are the field dependent barrier lowering in Schottky diodes (Schottky-effect), generation currents within the depleted region and carrier injection through the contacts.

Due to the build up of space charge the electric field drops linearly. The depletion width, i.e. the active width of the device, is given by [Sze81]

$$w = \sqrt{\frac{2\epsilon\epsilon_0}{q}\left(\frac{N_A + N_D}{N_A N_D}\right)(V_{\mathrm{bi}} - 2kT/q + V)} \approxeq \sqrt{\frac{2\epsilon\epsilon_0}{qN_B}V} \qquad (2.13)$$

where $N_B = N_D$ or N_A depending on whether $N_A \gg N_D$ or vice versa. The approximation in equation 2.13 is valid for detectors since they use one sided abrupt junctions and the bias voltage $V \gg V_{\mathrm{bi}} - 2kT/q$. ϵ and ϵ_0 are the permittivities of the semiconductor and the vacuum, respectively. In order to achieve a high quantum efficiency for low or moderate Z materials (Si, GaAs), it is necessary to have several hundreds of μm active depths (equation 2.1). According to equation 2.13 very lightly doped material (doping $< 10^{13}$ cm^{-3}) is required to allow such depletion at a reasonable voltage, (i.e. $\lesssim$ several 100 V). In fig. 2.7 the depletion widths for Si ($\simeq$ GaAs) at various doping densities is shown as a function of the reverse bias voltage.

The limit to the depletion depth is the breakdown of the diode due to impact ion-

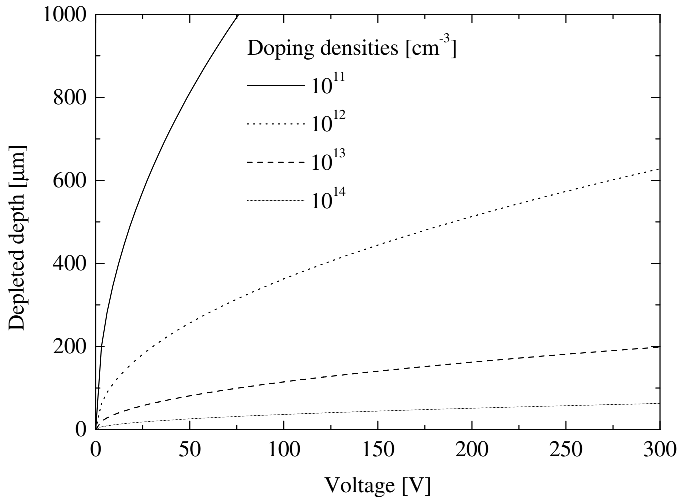

Figure 2.7: Depletion depth for various doping densities. This shows the need for low doping densities in order to achieve an active region of several hundreds of μm.

isation (avalanche breakdown) or carrier injection through a contact. Apart from these physical limits some applications may set limits to the maximum voltage.

Charge Loss

Carriers are considered lost if they recombine or are trapped for a time long

enough to prevent them from generating signal within the shaping time of the processing amplifier (see section 2.3).
The parameter that determines the charge collection efficiency (CCE) is the mean free drift length λ. It is *the* vital parameter of any detector material. If x is the distance from the generation point of N_0 carriers, then

$$N(x) = N_0\, e^{-x/\lambda} \tag{2.14}$$

is the number of carriers left at point x. The mean free drift length λ is the product of the drift velocity v_D and the lifetime τ of the carrier.

$$\lambda = v_D\, \tau = \mu\, E\, \tau \tag{2.15}$$

The drift velocity is electric field (E) dependent, $v_D = \mu\, E$ where μ is the mobility of the carrier. The proportionality of the drift velocity and the electric field is valid for field strengths up to about $2 \cdot 10^3$ V/cm, with saturation occurring at about $2 \cdot 10^4$ V/cm (for Si and GaAs). Since the electric field inside the active region may change significantly, the mean free drift length will vary accordingly. The lifetime τ is the time the average carrier spends in the conduction band[6].
The mean free drift lengths were calculated from mobility and lifetime values given in references [Sze81],[Rog97]. For GaAs λ is in the order of several mm at most, while in Si several m readily is achieved [Sch95]. Accordingly a good Si detector has 100 % CCE. In pure GaAs, where the lifetime is limited by radiative and Auger recombination, the carriers would have a mean free drift length of tens of cm (lifetimes $> 50\ \mu$s) [Sch95]. However trapping centres reduce the lifetime, and Shockley-Read-Hall (SRH) recombination and trapping dominate. The overall lifetime τ is given by

$$\tau = \left(\frac{1}{\tau_{\mathrm{rad}}} + \frac{1}{\tau_{\mathrm{Auger}}} + \frac{1}{\tau_{\mathrm{SRH}}} + \frac{1}{\tau_{\mathrm{trap}}}\right)^{-1} \tag{2.16}$$

where τ_{rad}, τ_{Auger}, τ_{SRH} and τ_{trap} are the radiative, Auger, Shockley-Read-Hall and trapping lifetimes respectively.
The trapping rate R_c is described by[7]

$$R_{c,n} = v_{th,n}\, \sigma_n\, n\, N_t \left(1 - \frac{1}{1 + \exp(\frac{E_t - E_F}{kT})}\right) \tag{2.17}$$

where v_{th} is the thermal velocity, σ is the capture cross-section, n is the carrier concentration, N_t is the trap concentration and the last expression is the fraction

[6] The lifetime τ in equation 2.15 is not well defined since a carrier may be trapped and released again. This may happen very fast (de-trapping time $\ll$ shaping time) or slowly (de-trapping time $\gg$ shaping time) with respect to the shaping time. Here the lifetime is understood as the length of time the carrier spends in the conduction band within the shaping time.

[7] The equation is given for electrons; for holes it is analogous.

of non-occupied traps determined by the Fermi-Dirac distribution. The emission rate R_ϵ is given by

$$R_{\epsilon,n} = \epsilon_n \, N_t \, \frac{1}{1 + \exp(\frac{E_t - E_F}{kT})} \tag{2.18}$$

where ϵ_n is the emission probability. If the emission time is longer than the collection time of the carriers, the capture rate will not equal the emission rate (the system is in a non-stationary, non-equilibrium state). For a stationary non-equilibrium condition the emission rate will be equal to the capture rate. The recombination rate U is then given by [Lut99]:

$$U = \frac{\sigma_n \, \sigma_p \, v_{th,n} \, v_{th,p} \, (pn - n_i^2) \, N_t}{\sigma_n \, v_{th,n} \left(n + n_i \, \exp(\frac{E_t - E_i}{kT}) \right) + \sigma_p \, v_{th,p} \left(p + n_i \, \exp(\frac{E_i - E_t}{kT}) \right)} \tag{2.19}$$

where E_t is the energy of the trap and E_i is the energy of the intrinsic Fermi level. This equation describes the four processes occurring in a single level recombination centre:

1. electron capture
2. electron emission
3. hole capture
4. hole emission

An electron capture followed by a hole capture results in the loss of the electron (recombination), since the electron initially in the conduction band ends up in the valence band. An electron capture followed by its emission is the process of trapping and de-trapping resulting in a time delay as mentioned before. A simple electron capture (trapping) not followed by another process (within the shaping time) results in a loss of the electron. The signal in the latter case is not the same as in the recombination process, because the trapped electron changes the electric flux in the detector and contributes due to a displacement of charge (see section 2.3).

According to equation 2.19 the most effective recombination centres are those with energy levels close to the intrinsic Fermi level E_i or mid band gap, i.e. for $E_t = E_i$ U approaches a maximum (e.g. Au in Si or the EL2 in GaAs).

The recombination rate is driven by the distance from the thermal equilibrium, i.e. $pn - n_i^2$. So for a reverse bias detector where $np \ll n_i^2$ (depleted) equation 2.19 simplifies to

$$U = -n_i \left[\frac{\sigma_n \, \sigma_p \, v_{th,n} \, v_{th,p} \, N_t}{\sigma_n \, v_{th,n} \, \exp(\frac{E_t - E_i}{kT}) + \sigma_p v_{th,p} \, \exp(\frac{E_i - E_t}{kT})} \right] \tag{2.20}$$

This determines the generation currents ($U < 0$) occurring in the depleted region. Traps have therefore two negative effects. They trap charge which leads to a lower charge collection efficiency and they generate leakage currents which increases the noise (see section 2.5). An illustration of generation and recombination (equations

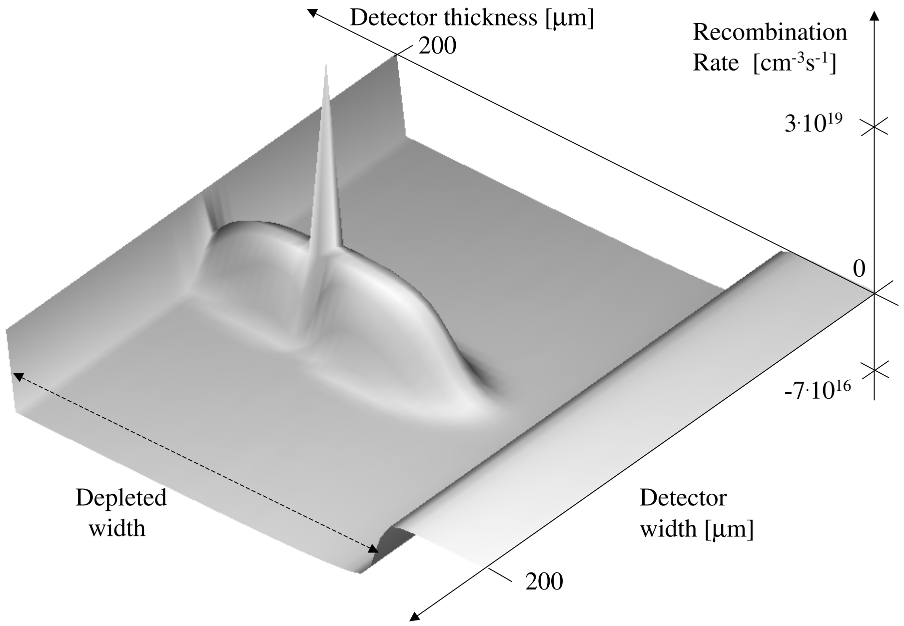

Figure 2.8: The picture shows the recombination rate over a partially depleted detector. Charge carriers were generated in the active region and have started to separate.

2.17 and 2.18) is given in fig. 2.8. The picture[8] shows a partly depleted detector. In the depleted area $np < n_i^2$ and generation dominates, the system is in a stationary non-equilibrium state. Where the detector is not depleted the semiconductor is in a stationary equilibrium, the generation rate is equal to the recombination rate, so no net recombination is observed.
Excess carriers were generated in the active region, as would be the case if an X-ray was absorbed. The e-h pairs have started to drift apart but still overlap slightly. Where they overlap the product $np > n_i^2$ and recombination is dominant, since both carriers types are present. In the regions where the carriers are fully separated, the excess carriers increase either n or p if they are electrons or holes respectively. This reduces the net generation, as seen in fig. 2.8. The region where excess charge carriers have been generated or have drifted to, is in a non-stationary non-equilibrium state.

2.2.2 Detector Materials

So far the importance of reducing leakage currents and charge loss have been discussed. If these were the only considerations then Si would be the best material by far. However the absorption efficiency is often a major issue, so higher Z materials are required. Additional reasons for choosing an other material than Si could be radiation damage or operation at extreme temperatures.
GaAs and Cd(Zn)Te are the next most common materials, but research is also carried out on diamond, TlBr, GaN, SiC and others. Ge has been used successfully for some time, however its low band gap (0.66 eV at 300 K) requires operation at low temperatures.
In the following only Si, GaAs and Cd(Zn)Te will be considered. Their absorption efficiencies for photons is plotted in fig. 2.9. For the comparison of different materials, typical thicknesses were used rather than comparing similar thicknesses. Since the absorption efficiency of Si is poor above about 20 keV, a scintillator is sometimes used to convert the X-rays into visible photons which are then absorbed in the Si. This increases the absorption efficiency but introduces various problems such as loss in spatial resolution and non-linearity.
In directly converting detectors, the gain in absorption efficiency by increasing the thickness depends on the energy. Fig. 2.10 shows how many times thicker a Si (GaAs) detector must be than GaAs (CdTe) in order to absorb the same amount of X-rays. The problems faced when operating an undamaged detector near room temperature are:

Si

None

GaAs

Bulk material: Purity is not sufficient. Due to the growth method arsenic antisites (EL2 defects) are present at a concentration of around 10^{16} cm^{-3}. These

[8] The data for the image were extracted from a simulation in MEDICI.

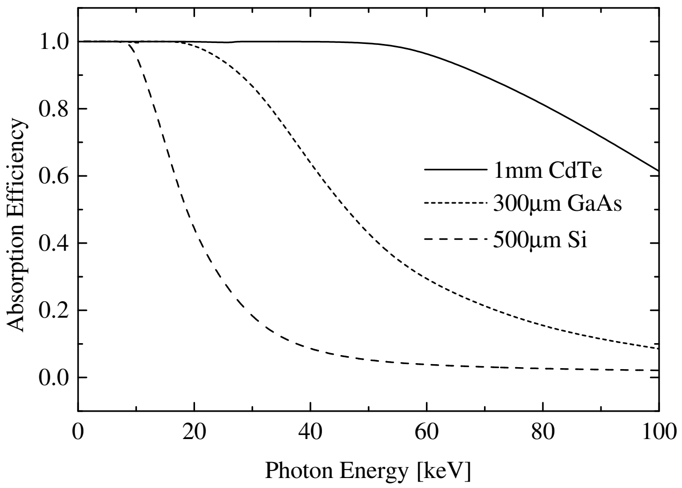

Figure 2.9: Energy dependent absorption efficiencies of Si, GaAs and CdTe for typical detector thicknesses.

compensate shallow acceptors (usually C), leading to semi-insulating properties. Such material can only be depleted because the occupancy of the EL2 increases at an electric field above about 1 V/μm [McG94]. Consequently trapping causes a major problem, nevertheless charge collection efficiencies close to 100 % have been achieved [Ber99].
Epitaxial material: Thick high quality material is not available. The carrier concentrations are still too high (about 10^{14} cm^{-3}) to allow the depletion of several hundreds of μm. Growth methods achieving the desired quality can so far not grow the desired thicknesses. Recent publications on high quality material show some encouraging results [Owe00].
Cd(Zn)Te
Polycrystalline structures, inhomogeneities and impurities cause major defects. In the case of CdZnTe Zn segregation is also a problem [Fie00]. The hole mobility is poor at about 50-100 cm^2/Vs, the electron mobility is about 1000 cm^2/Vs [Sch95]. Good detectors have been made on selected pieces. Due to the vast gain in absorption efficiency, Cd(Zn)Te detectors offer substantial benefits despite the problems to be overcome.

2.3 Generation of the Signal

The discussion so far has been concerned with the generation of the charge in the detection medium and the properties of the charge transport in the semiconductor.

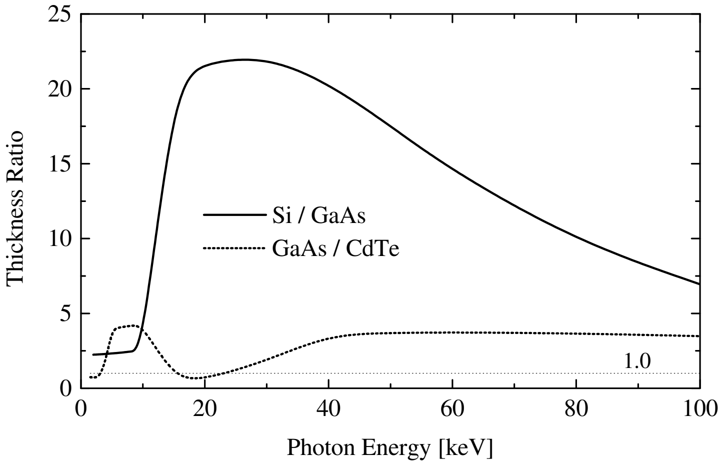

Figure 2.10: The graph shows how many times thicker a Si (GaAs) detector must be than a GaAs (CdTe), in order to achieve the same absorption efficiency.

It is however, the measured charge on a contact (integrated current), which is the subject of this section.

2.3.1 Ramo's Theorem

The current on the contact is equal to the rate of change of the charge on the contact. At a fixed bias voltage V, some charge Q will be present at the contact, this will be determined by the capacitance of the electrode. The stored energy of the capacitor $\mathcal{E}_{\mathrm{C}} = Q^2/2C$ is contained in the electric field $\vec{E}(\vec{x})$ inside the device. If charge carriers $q(\vec{x})$ in this field drift, the work it performs for a carrier movement $d\vec{x}$ is

$$\mathcal{E}_{\mathrm{F}} = q(\vec{x})\,\vec{E}(\vec{x}) \cdot d\vec{x} \tag{2.21}$$

Applying energy conservation, $\frac{d\mathcal{E}_{\mathrm{C}}}{dt} = \frac{d\mathcal{E}_{\mathrm{F}}}{dt}$, and taking the time derivative yields

$$q(\vec{x})\,\vec{E}(\vec{x}) \cdot \vec{v} = \frac{Q}{C}\,I_{\mathrm{C}} = V\,I_{\mathrm{C}} \tag{2.22}$$

where $\vec{v} = d\vec{x}/dt$ is the velocity of the carriers and $I_{\mathrm{C}} = dQ/dt$ is the induced current at the electrode. Re-arranging this equation gives

$$I_{\mathrm{C}} = q(\vec{x})\,\frac{\vec{E}(\vec{x})}{V} \cdot \vec{v} = q(\vec{x})\,\vec{E}_W \cdot \vec{v} \tag{2.23}$$

where $\vec{E}_W = \vec{E}(\vec{x})/V$ is the "weighting field" , which has the dimension of an inverse length.
Equation 2.23 was first put forward by S. Ramo in 1939 [Ram39] in the context of vacuum tubes and is known as Ramo's theorem.
Several papers have been published confirming this theorem ([Cav63], [Mar69], [Cav71], [Wil73], [Kim91]).

2.3.2 Components of the Current

Ramo's theorem has been shown to predict correctly the nature of current pulses in semiconductor detectors. It does not, however, give any information on the individual current components contributing to the overall signal.
The total current (I_{tot}) is the sum of three components, the electron (I_{e}), hole (I_{h}) and displacement (I_{d}) currents [MED99].

$$\begin{aligned} I_{\text{tot}} &= I_{\text{e}} + I_{\text{h}} + I_{\text{d}} \\ &= e\,\frac{\partial n_{\text{e}}}{\partial t} + (-e)\,\frac{\partial n_{\text{h}}}{\partial t} - \int_{\mathcal{A}} \frac{\partial D}{\partial t} d\mathcal{A} \end{aligned} \tag{2.24}$$

where n_{e} and n_{h} are the number of electrons and holes on the contact. D is the electric displacement and $\mathcal{A}$ is the area of the contact.
As charge is generated the displacement current will generate signal before any electrons or holes reach the contact. Once carriers reach the contact the displacement their presence caused is removed and the detector returns to its initial state. Fig. 2.11 shows the individual contributions for the contact collecting the holes (the signal on the anode looks similar). The data in fig. 2.11 are for a 200 μm thick Si detector with 1000 e-h pairs generated at the centre of the detector. The data were extracted from a simulation with MEDICI [Mat01]. The electron current contribution is zero since none of the generated electrons passes through the cathode. The displacement term returns to zero once all carriers have drifted out of the detector. The integration of the current components (charge) is shown in fig. 2.12. The charge increases constantly due to leakage current. The fast component of the charge pulse is due to the induced current, as seen from fig. 2.12.
The Si detector used as an example in fig. 2.11 and fig. 2.12 has 100 % CCE. For detectors where trapping occurs, the trapped charge changes the electric flux density, which is reflected by the induced charge contribution not returning to zero (within the time of interest). Any trapped charge that recombines allows the displacement to return to zero. Ramo's theorem, as given above assumes that any trapped charge causes a displacement and therefore does not include any recombination. Nevertheless it correctly predicts the charge pulse, because recombination can normally be neglected due to the very low free carrier concentrations in the depleted region of a detector.

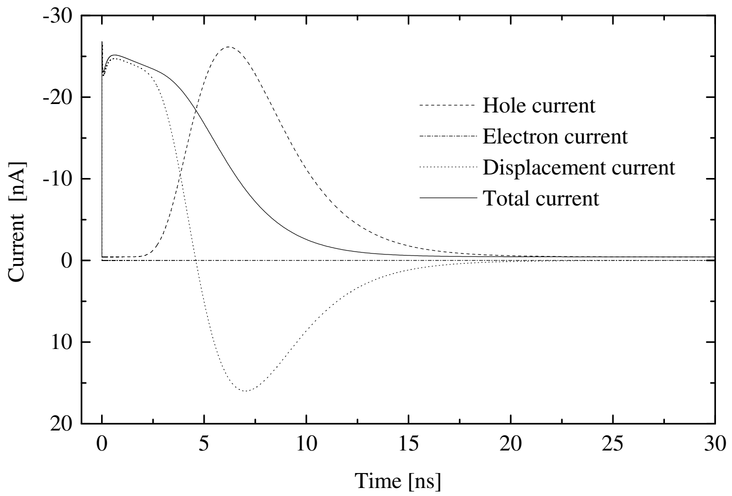

Figure 2.11: Current components of a signal in a Si detector. The device collects holes, so the electron current is zero, the displacement current returns to zero as the detector returns to its initial state.

2.3.3 Calculation of the CCE

The CCE can be calculated from equations 2.1, 2.14 and 2.23. The photons are assumed to impinge at $x = 0$ and to be absorbed at $x = x_g$ as shown in fig. 2.13. For a normalised amount of charge generated at $x = x_g$ the CCE is given by

$$\mathrm{CCE}_{x_g} = \int_{x_g}^{0} E_W(x)\, e^{-(x_g - x)/\lambda_1}\, dx + \int_{x_g}^{w} E_W(x)\, e^{-(x - x_g)/\lambda_2}\, dx \tag{2.25}$$

where λ_1 and λ_2 are the mean free drift lengths of the carriers moving to the contacts at $x = 0$ and $x = w$, respectively. Equation 2.25 is normalised so that for $\lambda_1 \to \infty$ and $\lambda_2 \to \infty$ the $\mathrm{CCE}_{x_g} \to 1$. In the case where E_W is constant (equal to $1/w$) for all x equation 2.25 is known as the Hecht theorem.

Taking the exponential absorption of the photons (equation 2.1) into account yields the average CCE for an infinite number of photons.

$$\mathrm{CCE} = \int_{0}^{w} \frac{\alpha\rho e^{-\alpha\rho x_g}}{1 - e^{-\alpha\rho w}} \Big(\int_{x_g}^{0} E_W(x) e^{-(x_g - x)/\lambda_1} dx + \int_{x_g}^{w} E_W(x) e^{-(x - x_g)/\lambda_2} dx \Big) dx_g \tag{2.26}$$

where $E_W(x)$ is the magnitude of the weighting field at point x.
Equations 2.25 and 2.26 are approximations, assuming that the electric field component normal to the x-direction is zero and the carriers only travel along the x-direction. A practical example is given in chapter 6 section 6.2.

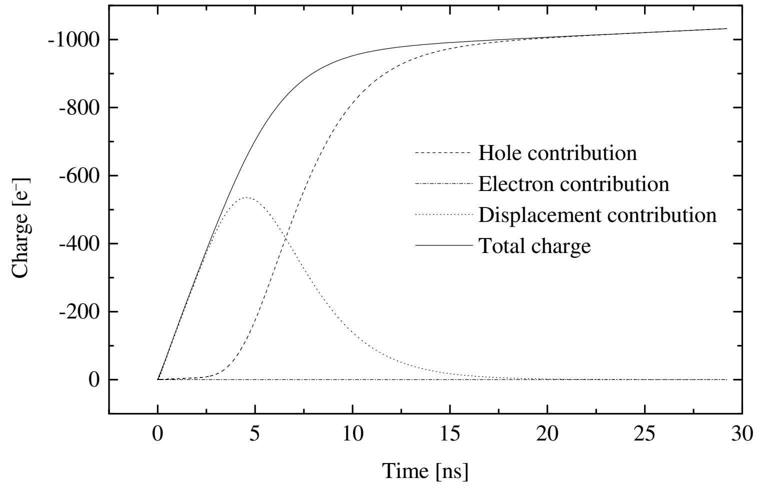

Figure 2.12: Charge pulse generation in a Si detector. The data are the integrated currents from fig. 2.11.

2.4 Read-Out Electronics

Three different modes of read-out are common, spectroscopic, charge integrating and photon counting. The integrating systems give information on the deposited energy while the photon counting register the number of photon absorption events. Spectroscopic devices and photon counting systems use similar front end electronics.

2.4.1 Integrating Systems

The simplest way to read out a detector is to attach a capacitance to one of its electrodes and integrate the signal current. After a certain exposure time the voltage on the capacitor is a measure of the energy deposited inside the detector. Such systems do not provide any information on individually absorbed photons, the leakage current of the detector is added to the signal and the dynamic range is limited by the capacitance. However since the required electronics are simple (a capacitance, a gate and address logic for the read out), a high spatial resolution can be achieved with pixellated devices having pixel sizes below 30 μm.
If Q_S is the charge output of the detector then the voltage measured V_{out} on the front-end input capacitance C_{in} is

$$V_{\mathrm{out}} = \frac{Q_S}{C_{\mathrm{det}} + C_{\mathrm{in}}} \tag{2.27}$$

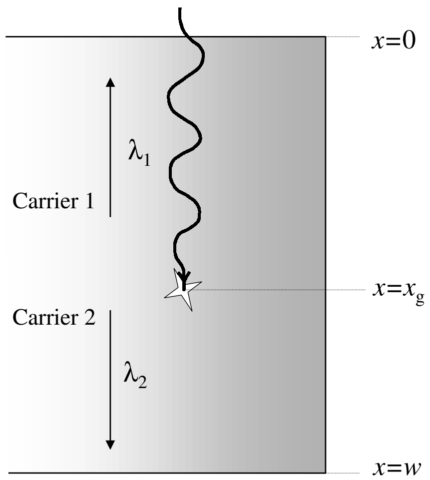

Figure 2.13
Geometry assumed for equations 2.25 and 2.26. The X-rays are assumed to come from the negative x-direction, impinging on the detector at $x = 0$.

where C_{det} is the capacitance of the output electrode of the detector.
In order to avoid any influence on the incoming signal due to the voltage on the input capacitance, the capacitor can be decoupled by using a current mirror. The signal of all the incoming charge is then seen on the input capacitor and the output voltage is directly proportional to incoming charge.

$$V_{\text{out}} \propto \frac{Q_S}{C_{\text{in}}} \tag{2.28}$$

2.4.2 Photon Counting and Spectroscopic Systems

Both photon counting and spectroscopic detectors evaluate events individually and commonly use the following front-end electronics.

Charge Sensitive Amplifiers

An evaluation of single events can be achieved by using an amplifier in the configuration shown in fig. 2.14. The system converts the input charge Q_{in} to an output voltage V_{out}, the conversion factor or A_Q is the charge gain of the amplifier.
If the voltage gain $dV_{\text{out}}/dV_{\text{in}} = -A$ and the input impedance of the amplifier Z_{in} is virtually ∞, the voltage difference V_f across the feedback capacitance C_f is

$$V_f = (A+1)\, V_{\text{in}}$$

All charge coming from the detector Q_{in} will be integrated onto C_f, so the charge on the feedback capacitor is

$$Q_f = C_f\, V_f = C_f\,(A+1)\, V_{\text{in}} = Q_{\text{in}}.$$

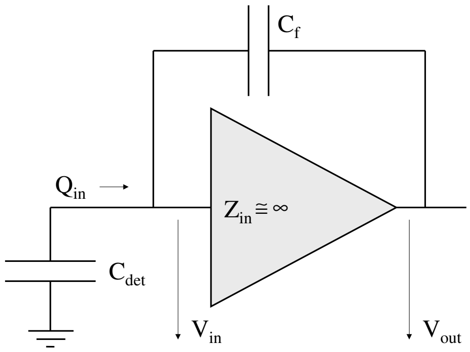

Figure 2.14
Charge sensitive amplifier configuration for reading out a detector. It allows the measurement of virtually all signal charge.

The effective input capacitance C_{in} is therefore

$$C_{\text{in}} = \frac{Q_{\text{in}}}{V_{\text{in}}} = C_f\,(A+1)$$

and for $A \gg 1$ it is proportional to the gain of the amplifier (hence the expression dynamic input capacitance).
Finally the gain A_Q is given by

$$A_Q = \frac{dV_{\text{out}}}{dQ_{\text{in}}} = \frac{A\,V_{\text{in}}}{C_{\text{in}}\,V_{\text{in}}} = \frac{A}{A+1} \cdot \frac{1}{C_f} \approx \frac{1}{C_f} \qquad (A \gg 1) \tag{2.29}$$

and therefore only depends on the feedback capacitor C_f (if $A \gg 1$).
So far, a charge Q_{in} coming from the detector has been considered but its relation to the signal charge Q_S is still to be determined. The charge remaining on the detector capacitance C_{det} is $Q_{\text{det}} = Q_S - Q_{\text{in}}$. The fraction of the signal charge measured is then

$$\frac{Q_{\text{in}}}{Q_S} = \frac{C_{\text{in}}\,V_{\text{in}}}{Q_{\text{det}} + Q_{\text{in}}} = \frac{C_{\text{in}}}{Q_S} \cdot \frac{Q_S}{C_{\text{in}} + C_{\text{det}}} = \frac{1}{1 + C_{\text{det}}/C_{\text{in}}} \approx 1 \qquad (\text{if } C_{\text{in}} \gg C_{\text{det}}) \tag{2.30}$$

The feedback capacitance C_f and the voltage gain A are therefore the two parameters determining the performance of a charge sensitive amplifier. The charge gain A_Q can be selected by choosing the value of the feedback capacitor, the voltage gain A then determines the fraction of the signal charge that contributes to the measured output. Typical values for C_f and C_{det} are in the range of several pF, the gain is A usually $> 10^3$, so more than 99.9 % of the signal charge is measured. The circuit in fig. 2.14 stores the charge on the feedback capacitor for a (theoretically) infinitely long time. In order to cope with any sequence of charge pulses the amplifier must be reset. This is achieved by either draining the charge through a resistor in parallel with the feedback capacitor or by resetting it with a transistor. Since photons are processed individually, they can be counted and/or their energy measured.

2.4.3 Pulse Shaping

The output of the amplifier V_{out} is a step function. For further processing it is useful to shape this constant output into a pulse. This is achieved with an RC or constant current shaper. The output voltage is

$$V_{\mathrm{out,RC}}(t) = \frac{Q_{\mathrm{in}}(t)}{C_f}\, e^{-t/RC} \tag{2.31}$$

$$V_{\mathrm{out,I}}(t) = \frac{1}{C_f}\Big(Q_{\mathrm{in}}(t) - I_c\, t\, \Theta(Q_{\mathrm{in}})\Big) \tag{2.32}$$

for an RC and a constant current shaper, respectively. RC is a time constant and I_c is a constant current. The Θ function[9] assures that the output does not go negative.

The shaped signal is shown for various shaping times and constant currents in fig. 2.15. The data plotted in fig. 2.15 are the simulated pulses discussed previously in fig. 2.12, section 2.3, evaluated according to equations 2.31 and 2.32. Since the peaking time of the amplifier has been neglected, the rise times are given by the collection time of the carriers. This collection time is strongly dependent on the detector material and on contact geometry, and the optimum shaping time varies accordingly.

The amplitude of the output pulse contains the information on the detected photon energy. This signal can be further processed or sampled with an ADC (giving a pulse height spectrum).

Shorter shaping times allow a higher rate and suppress the leakage current contribution but affect the signal amplitude. The reverse holds for longer shaping times.

2.5 Noise

The term “noise” may have a different meaning depending on the context. In the following, the definition of noise in energy resolving detectors is discussed first, followed by a part which is concerned with the noise in imaging systems.

2.5.1 Noise in Energy Resolving Systems

Typical measures of the energy resolution are the FWHM (**F**ull **W**idth at **H**alf **M**aximum height) of a peak due to photons of a given energy in the pulse height distribution or in the case of a Gaussian peak shape, the standard deviation σ (FWHM $\simeq 2.35\sigma$).

The FWHM value is often quoted since this can be measured from any peak shape, e.g. asymmetric distributions such as Landau peaks.

[9] The Θ function is the integral of the Dirac delta function and is zero or one if its argument is negative or positive, respectively.

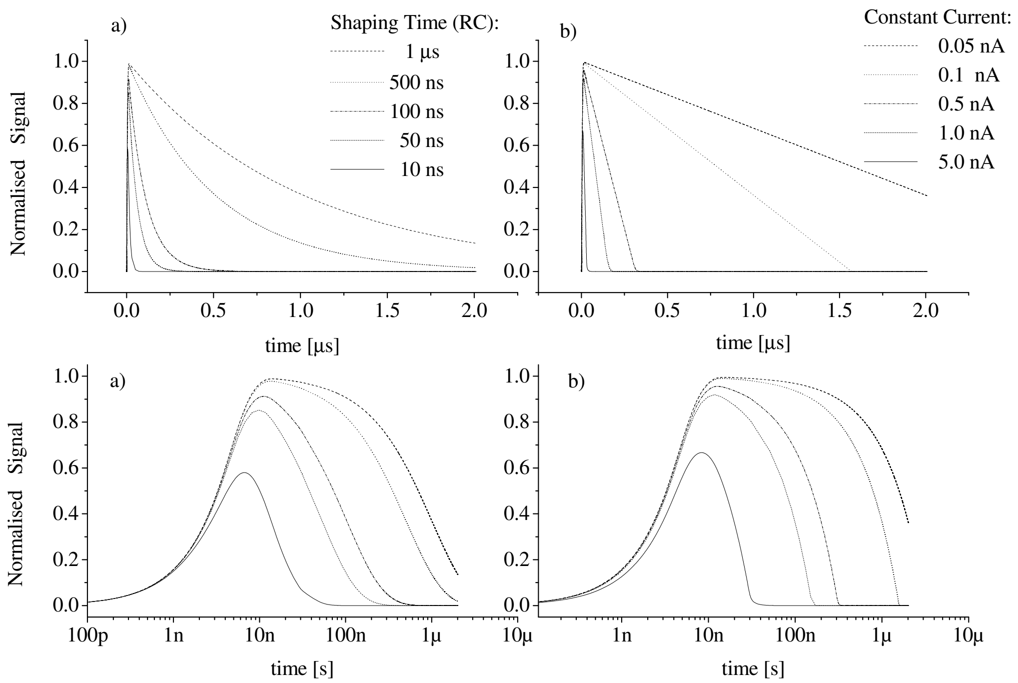

Figure 2.15: The left hand side (a) shows the output from a RC shaper, the right (b) from a constant current shaper. The lower, logarithmic plots illustrate the loss in signal amplitude depending on the shaping parameter.

Fano Noise

The photo- or Compton-electron generating the signal charge does this with some statistical variation in the number of created e-h pairs, for a given photon (or electron) energy.
The resulting variance in the number $N_{\mathrm{e-h}}$ of generated e-h pairs is [Ali80]

$$\mathrm{Var}(N_{\mathrm{e-h}}) = F\, N_{\mathrm{e-h}} \tag{2.33}$$

where F is the material dependent "Fano factor", which has a value of ≈ 0.1 for Si, GaAs and CdTe [Kno00], [Lut99]. The Fano factor $F < 1$ because the various energy loss processes are not statistically independent.
The Fano noise determines the minimum energy resolution possibly achievable, it is the intrinsic resolution of any detector.

Thermal, Flicker and Shot Noise

Noise added to the signal from the read-out is referred to as electronic noise. It is commonly measured as an equivalent noise charge (ENC) [Rad88]. The ENC is defined as the amount of input charge that gives a signal-to-noise ratio of one.

Shot noise
The leakage current $I_{\rm det}$ from the detector is due to the emission of quantised charge carriers (electrons or holes). Since this independent process is random it follows Poisson statistics, which should lead to a noise contribution proportional to $\sqrt{I_{\rm det}}$.
Lower noise values have been observed [Luk00] and are assumed to be due to trapping processes. If emitted carriers are trapped the measured current $I_{\rm det}$ must be due to more carriers than in the non-trapping case. This leads to a smaller relative variation of the current and hence a lower noise.

Thermal noise
The noise in a resistor arises from the thermal motion of charge carriers. When the resistor is in thermal equilibrium with its surroundings, the mean value of potential difference between the ends of the resistor is zero. However, Brownian motion of the charge carriers results in a fluctuating potential difference across the resistor.
Thermal noise in a resistor R at temperature T contributes $\sqrt{4kT/R}$ to the electronic noise [Rad88], where k is Boltzmann's constant.

Flicker noise
Flicker noise or $1/f$ noise is still not fully understood. It is assumed that it originates from generation and recombination processes involving surface states and therefore depends on the contact technology and surface preparation.
It has approximately a $1/f$ dependence on the frequency and is independent of the amplifier shaping time [Rad88].

Shot and thermal noise are "white" noise sources, i.e. they show no frequency dependence. Due to their random nature their contributions increase with the square root of the shaper peaking time $\tau_{\rm S}$.
The input transistor of an amplifier is affected by thermal and shot noise. This leads to an additional noise contribution which depends on the transistor parameters. Adding up all the noise sources gives an overall ENC of

$$\mathrm{ENC} = \sqrt{S_1 \frac{1}{\tau_{\rm S}} \frac{2}{3} C_{\rm in}^2 \frac{4kT}{g_m} + S_2\, \tau_{\rm S} \left(2eI_{\rm det} + \frac{4kT}{R}\right) + S_3 \frac{1}{f}} \tag{2.34}$$

where S_1, S_2 and S_3 are constants depending on the shaping network, g_m is the transconductance of the input transistor (which is assumed to be a FET $\rightarrow$ factor of 2/3 [Rad88]) and $C_{\rm in}$ is the input capacitance.

2.5.2 Noise in Imaging Detectors

If an image is taken several times under identical conditions the results will show some variation. Additionally some “fixed pattern” may be observed. These two effects are referred to as image noise.
Fixed pattern noise can easily be subtracted from the image. Ultimately Poisson statistics limit the image noise, however other noise sources may be dominant. For integrating systems the leakage current noise contribution is proportional to $\sqrt{t}$, where t is the exposure time. This limits the exposure time of integrating systems. Photon counting systems eliminate this effect of leakage current, and such devices should show Poisson image noise even at low exposures.
The image noise in photon counting detectors is discussed in more detail in chapter 5, section 5.3.

Chapter 3

The Investigated Devices

The characterised systems were developed under the IMPACT (**I**nnovative **M**icro-electronic **P**ixellated **A**nd **C**CD **T**echnology) project. IMPACT was funded through the Department of Trade and Industry Foresight initiative and was administered by PPARC. The detectors and read out electronics were designed at the Rutherford Appleton Laboratory[1].
This chapter describes two semiconductor hybrid pixel detectors which are characterised in chapter 4 and 5.

3.1 The ERD1

The **E**nergy **R**esolving **D**etector (ERD1) is designed for material inspection equipment using X-ray fluorescence spectroscopy. An image of the device is shown in fig. 3.1.
A description of the ERD1 system is given in references [Sel98] and [Sel99].

3.1.1 The Electronics

The detector is bump-bonded to a **P**ixel **A**rray **C**hip (PAC5). The PAC5 is an array of 16 by 16 pre-amplifiers with a pixel pitch of 300 μm by 300 μm. The segmentation gives reduced noise and a higher count rate. Each pixel contains a charge sensitive pre-amplifier and a line driver, as shown in fig. 3.2.

The pre-amplifier has a folded cascode stage with a 200 μm : 1.2 μm optimised input FET taking 100 μA and has a feedback capacitance of 100 fF. The values are chosen to give adequate gain while maintaining reasonable gain uniformity between pixels. A simple transistor circuit, with a 1 MΩ stabilising resistor, is used to reset

[1] The systems were designed by Paul Seller.
Rutherford Appleton Laboratory, Chilton, OXON., OX110QX, UK.
seller@rl.ac.uk

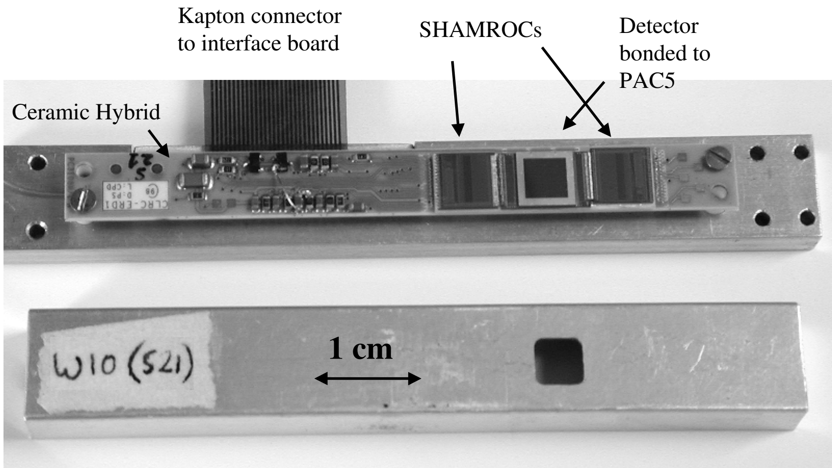

Figure 3.1: Photograph of the ERD1 showing the hybrid, read-out ICs and detector.

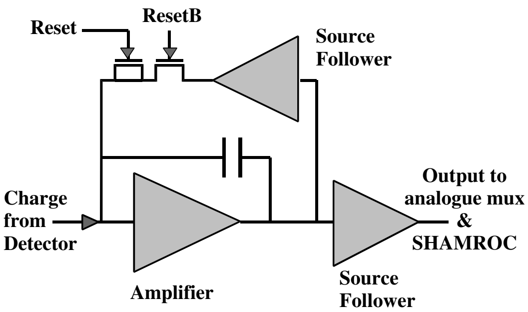

Figure 3.2 Schematic diagram of the electronics contained in each pixel of the PAC5.

the amplifier. At 1 pA leakage current a reset must be applied every 100 ms. The noise performance of the pre-amplifier is designed to give 20 electrons r.m.s. with a 250 fF detector capacitance, 250 fF pad capacitance and 10 pA leakage current when shaped by the 2 μs shaper.
All pixels are routed from the PAC5 and aluminium wire bonded to two **S**haper **A**nd **M**ultiplexer **R**ead **O**ut **C**hip (SHAMROC) integrated circuits. Both the PAC5 and SHAMROC are built on the Mietec 0.7 μm CMOS process. The SHAMROC contains 128 *CR-RC* shaper, peak-hold and comparator circuits, shown in fig. 3.3. A signal above threshold in any channel flags read-out electronics which fires the comparator which in turn sets a read-out flag in the chip. The output multiplexer identifies this flag and sends the analogue value and address of the channel hit to off-chip electronics. This action resets this shaper channel only. The output rate is limited by the clock speed of 1 MHz, however each pixel has a maximum rate of 40 kHz limited by the reset time of the channel.

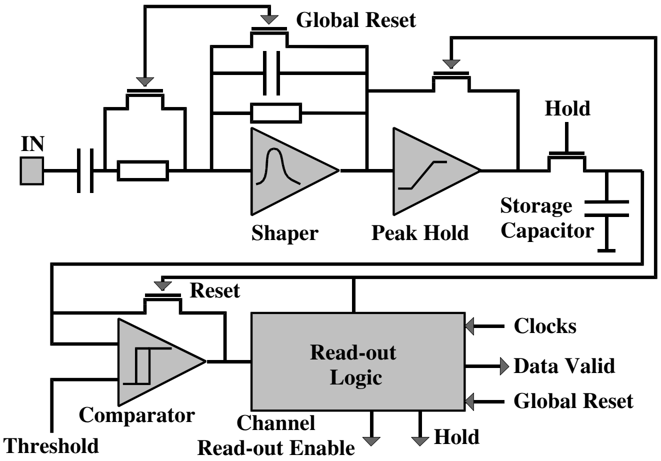

Figure 3.3 Schematic diagram of the electronics for each input of the SHAMROC.

A step voltage signal from a PAC5 amplifier is shaped by a 2 μs $CR-RC$ amplifier with a voltage gain of about 40. The shaped output drives a peak-hold circuit which holds the peak of the shaped signal. If this is above threshold it fires a comparator which provides a hit signal to the read-out logic. The minimum comparator input voltage which causes the comparator to change is 5 mV. When a comparator fires, it sets a flag in the read-out logic and enables a counter , which counts to 3 clock cycles before applying a hold signal, enabling the rest of the system to continue to acquire data. This hold signal also raises a flag which will trap a read-out pointer when it reaches the channel. When the pointer is trapped the analogue multiplexer is enabled and routes the stored value from the channel to the analogue output. The channel address and a data valid signal are also output to indicate that the data on the output is valid.
The read-out pointer passes through the logic for the 128 channels until it emerges at the PtroutB if standing alone. The pointer logic is designed to allow the pointer to skip channels with no data. A single channel read-out cycle takes 1 μs and the read-out logic then applies a reset to the peak-hold and comparator circuits of the channels and resets itself. The logic must wait for 20 μs following the departure of the pointer, before releasing the rest to the peak-hold and comparator circuits, to allow time for the tail of shaped analogue signal to return to zero. As the data is only available at the output while the pointer is present at the channel, the data acquisition system must sample the data in one clock cycle. A true and inverse clock are provided for the SHAMROC to help reduce their noise contribution, which is important as they are running at all time.
For testing purposes the SHAMROC has the ability to inject signals to the inputs of any individual channels. A common calibrate input is used to apply input signals and a “masking” register selects which channels are active. The functional block diagram of the whole system is shown in fig. 3.4. The pointers move between the SHAMROCs collecting the flags.

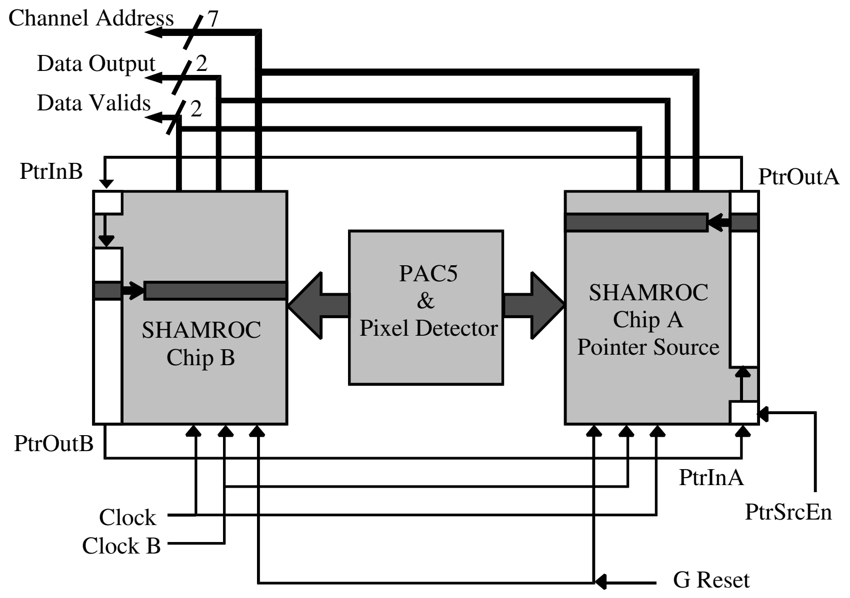

Figure 3.4: Block diagram of the ERD1 system.

3.1.2 The Detectors

The ERD1 is equipped with 300 μm or 500 μm thick Si detectors, fabricated on four inch wafers using double-sided processing at SINTEF[2]. The material is <100> n-type Si with resistivities between 3 and 10 kΩ cm. The pixellated side has p implants with 1.5 μm Al metallisation. The bump-bond pads have an additional layer of 5 μm thick Zn plated with 50 nm Au. A polyamide passivation is used as an insulating underfill. The ohmic back contact is an n implant through a 200 nm thick oxide. A 0.5 μm thick Al metallisation frame allows contacting the back using wire bonding and avoids a parasitic absorbing metal layer on top of the active region. The detector is bump-bonded to the PAC5 using Au studs and conductive glue, the process was done at Hycomp[3].
A photograph of part of the pixellated side of a detector is shown in fig. 3.5. The pixels have 280 μm sensitive width plus a 20 μm gap. The guard-ring is 140 μm wide and is surrounded by four floating guard-rings, as shown in fig. 3.5. Not all detectors use this design but it allows a higher over-depletion for faster carrier collection in order to reduce charge sharing due to diffusion. The electric field in the detector was simulated[4] with MEDICI and is plotted in fig. 3.6. The corresponding potential is shown in fig. 3.7 for an applied bias of 50 V.

[2]SINTEF, P.O. Box 124, Blindern, 0314 Oslo, Norway.
[3]Hycomp Inc., 165 Cedar Hill St., Malborough, MA01752, USA.
[4]The simulation of floating guard-rings was carried out together with K. Mathieson. K.Mathieson@physics.gla.ac.uk, G12 8QQ, University of Glasgow.

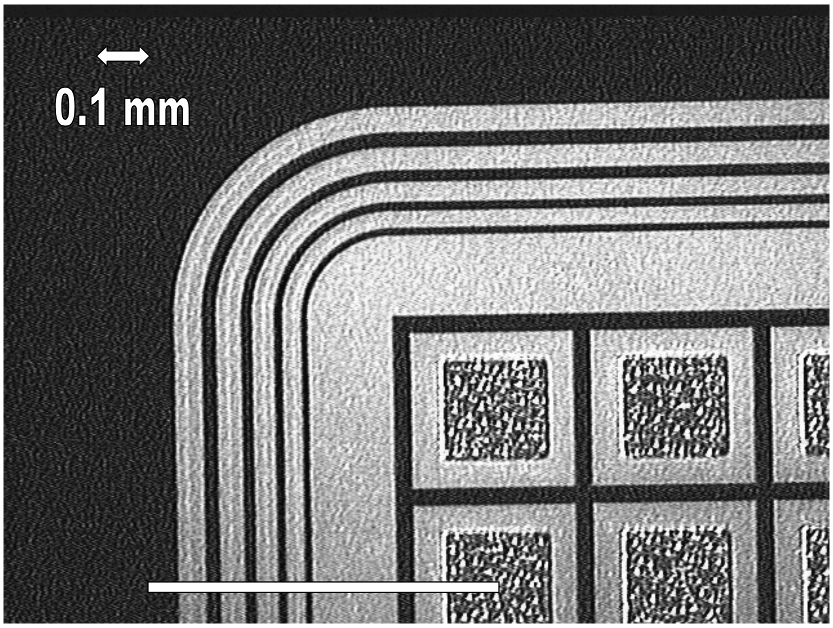

Figure 3.5: Photograph of an ERD1 Si detector. This detector has four floating guard-rings in order to allow higher over-depletion. The Au bond-pads are centred on each pixel, their surface is rough to improve the contact to the bump-bond. The white line at the lower part of image shows the simulated section shown in fig. 3.6 and 3.7.

3.1.3 Experimental Setup

The schematics of the ERD1 setup are shown in fig. 3.8. The detector module is connected to an interface board which supplies the power and is linked to a PC equipped with National Instruments DAQ cards (PCI-6110E and DIO-6533 [32HS]). LabView software is used to control the cards and handle the data acquisition. The ERD1 draws about 50 mA at 5.5 V, the detector bias is supplied separately using a battery source adjustable between 0 and 400 V.

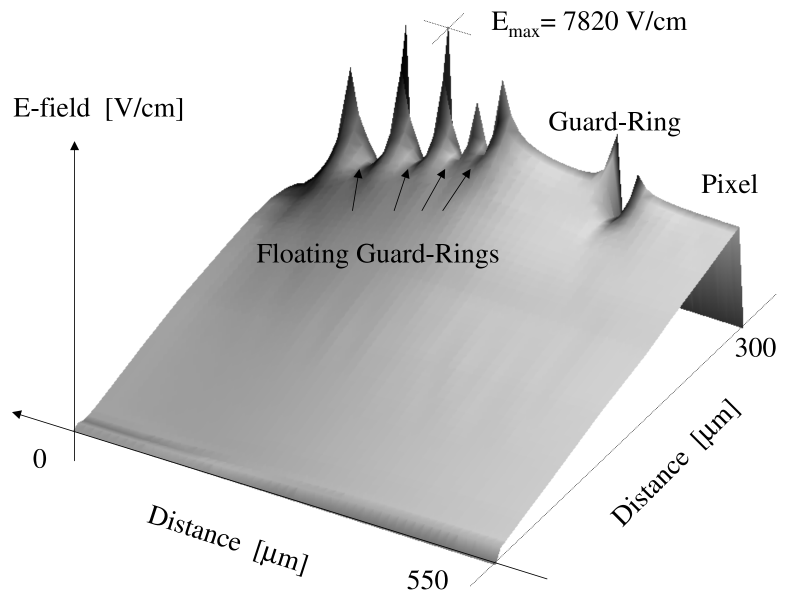

Figure 3.6: Simulated electric field in a ERD1 Si detector. It is biased at 50 V, the simulated section is from the edge of the detector to the centre of the first pixel, as shown in fig. 3.5.

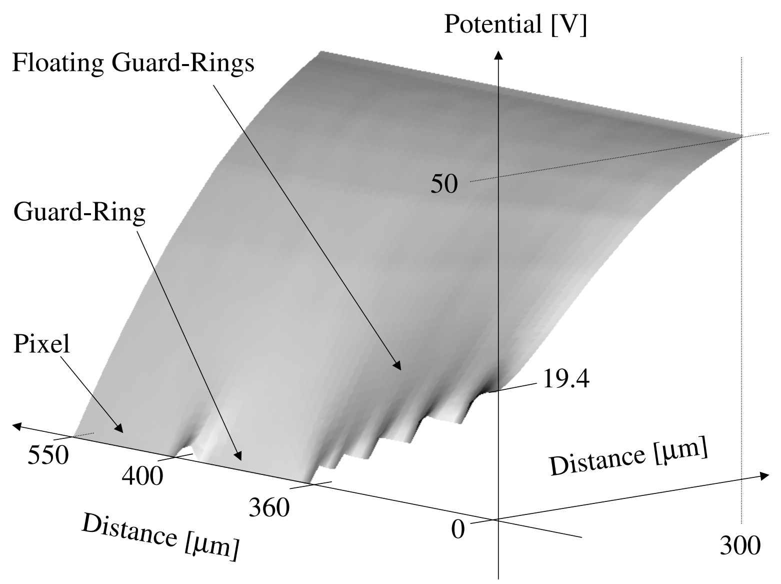

Figure 3.7: Potential across an ERD1 detector. The floating guard-rings step down the bias voltage in a controlled manner, reducing the maximum electric field. For better illustration this image is rotated by 180^0 around the z-axis with respect to fig. 3.6.

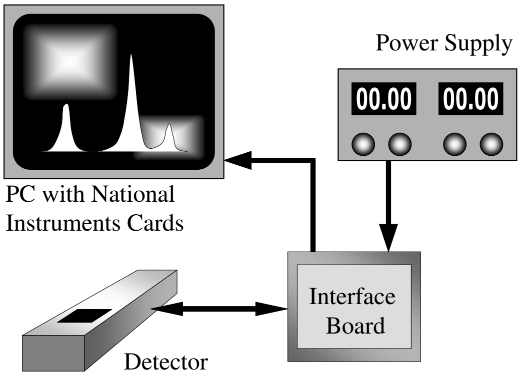

Figure 3.8
Experimental setup of the ERD1 system. The detector is connected to an interface board which supplies the power and is linked to a PC equipped with National Instruments DAQ cards.

3.2 The LAD1

The **L**arge **A**rea **D**etector (LAD1) is an imaging detector developed for time resolved X-ray diffraction studies. It is modular and capable of being tiled to cover an area of 30 cm by 30 cm with 4 million pixels. The pixel is 150 μm square, the dead area is approximately 7 %. Each module holds seven read-out chips and one detector. The dead space is given by the edge of the detector and a fan-out on the detector eliminates the dead area between adjacent read-out chips. The modules have a Mo substrate providing good thermal conductivity and a reasonably similar thermal expansion coefficient.
Single chip detectors were fabricated for testing purposes. An image of a module with a single chip is shown in fig. 3.9. The active region of a single chip detector

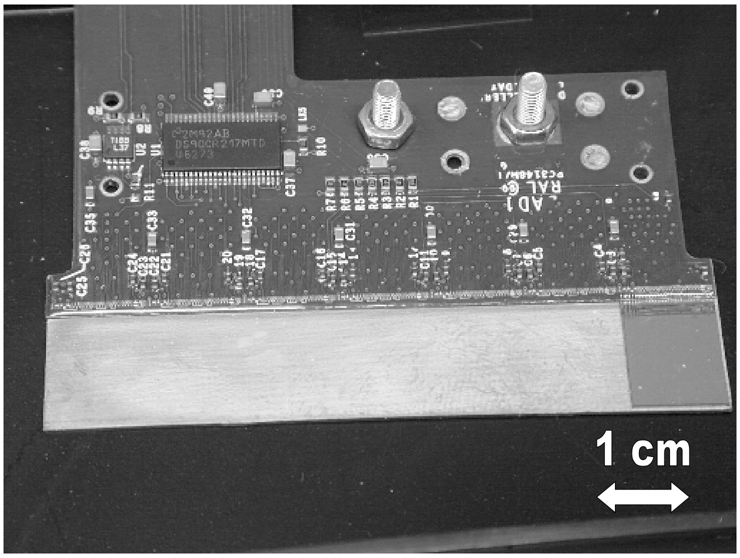

Figure 3.9: Photograph of a single chip LAD1 module. The ICs are mounted on a Mo plate, which can hold seven read-out chips.

is 9.6 mm squared, given by the 64 by 64 array of 150 μm square pixels.
A description of the LAD1 system is given in references [Sel99] and [Sel00].

3.2.1 The Electronics

In the Aladin (**A** **L**arge **A**rea **D**etector with **IN**crementors) read-out chips each pixel contains a bond pad, pre-amplifier, shaper, comparator and 15 bit counter, as shown in fig. 3.10. The pre-amplifier integrates the charge from the 150 fF pixel capacitance onto a 10 fF feedback capacitor with an estimated 300 e^- r.m.s. ENC including the shaper. The pre-amplifier feedback and shaper fall-time are

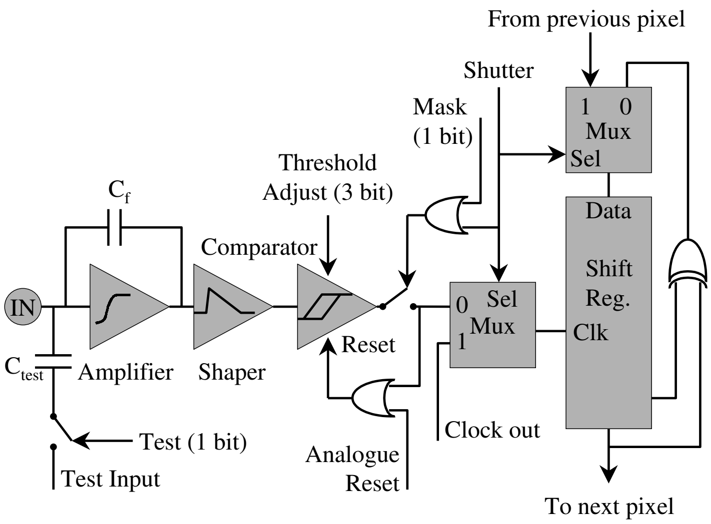

Figure 3.10: Diagram of the electronics contained in each pixel cell of the Aladin chip. Each pixel has a test input, a 3 bit threshold adjust and a masking bit which can be addressed individually. For read out the counter is used as a shift register.

both constant current driven, giving a linear falling ramp. Both are programmable via I2C (Inter-IC) driven DACs on the chip. The comparator has a 3 bit global threshold offset adjustment for each pixel. The 15 bit pseudo-random dynamic counter is adapted for simple serial read-out. The I2C also programs the individual calibration and mask bits for each pixel.

Four columns are read out in series at 10 MHz, giving an acquisition time per image of 4 x 64 x 15 x 0.1 μs = 384 μs. Each chip dissipates approximately 750 mW at 3.3 V. Data are transferred from the Aladin via a high-speed serial link (National-Semi-Conductors-Channel-Link). The read-out is controlled by the Count Enable signal that is applied to the chip. Count Enable going high enables the Aladin comparators and counters for as long as required. Count Enable going low disables the Aladin comparators and counters and also turns the Aladin counters into shift-registers. The data are then shifted out at 10 MHz per chip. Seven chips can be multiplexed onto one (16 data bit) bus at 70 MHz. The 70 MHz clock is divided down in the Aladins to control the read-out rate, using two registers that are programmed over the I2C interface. The Master asserts a bit on an extra 17$^{\text{th}}$ line to help synchronise the data at the receiving end. The Channel Link chip collects the 16 bit words from the 7 Aladins at 70 MHz and serialises them. The inverse conversion is performed at the PC end of the link. A schematic of the LAD1 module is shown in fig. 3.11.

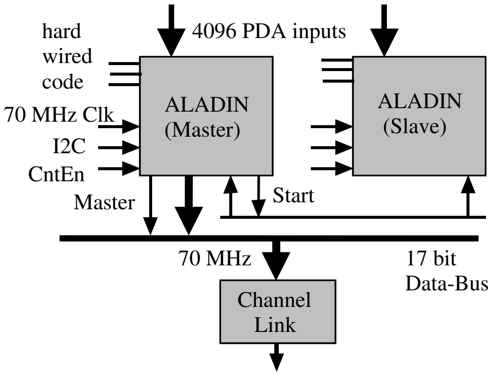

Figure 3.11: Schematic of the LAD1 module.

3.2.2 The Detectors

The detectors were fabricated on four inch Si wafers using double sided processing at SINTEF. Both 300 μm and 500 μm thick detectors were made on 3-10 kΩcm, <100> n-type material.

The pitch on the Aladin cells and bond pads is 150 μm by 144 μm while the detector pixel pitch is 150 μm square. The bond pads on the detector are tracked to the pixels, allowing the Aladin read-out chips to be butted together with no dead regions on the detectors. The fan-in of the bond-pads on the detector is shown in fig. 3.12.

The outer part of the detector, including the guard-rings and bias contact, is shown in fig. 3.13. Floating guard-rings and a guard band surround the pixels, similar to the designs of the ERD1 (section 3.1.2). The detector bias is applied through a front side bump-bonded n^+ contact, so no wire bond to the window side of the detector is required. Fig. 3.14 shows the results of simulation of the potential distribution of a Si LAD1. The corresponding electric field is shown in fig. 3.15. The bias voltage is 40 V applied to the front side n^+ implant. The floating back contact acquires virtually the same potential which depletes the detector in the usual manner. This biasing technique inevitably creates a low field region under the n^+ bias contact. The extent of this inactive region depends on the size and position of the bias contact and is slightly reduced by over depleting.

3.2.3 Experimental Setup

The setup for single chip modules comprises of the detector, an interface board and a PC equipped with an National-Instruments (DIO-6533 [32 HS]) and an I2C card. A schematic of the setup is shown in fig. 3.16.

The power supply delivers 3.3 V to the detector module via the interface board. The detector bias is supplied separately using a battery source.

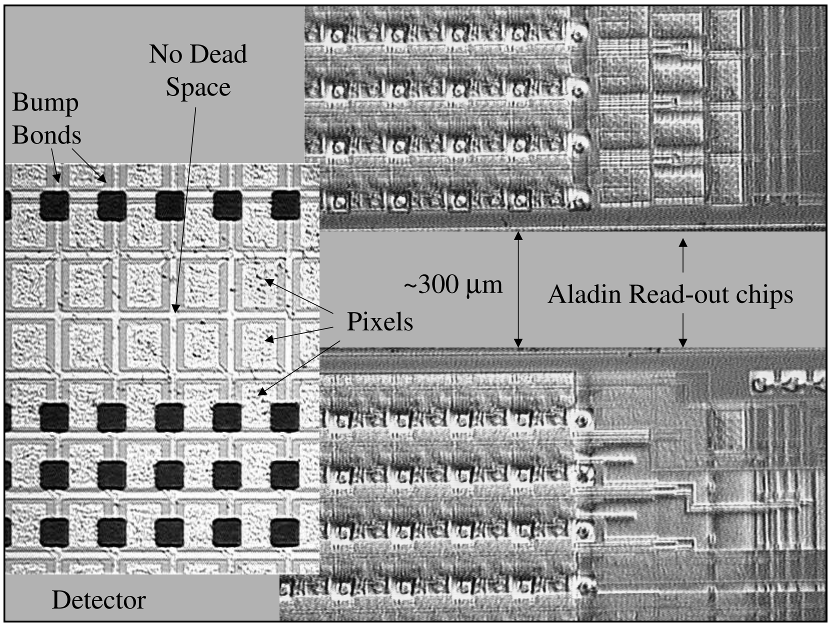

Figure 3.12: Illustration of the fan-out of the pixel pitch. Sections of two neighbouring Aladin chips are shown with a detector. The separation of the Aladins does not lead to any dead space due to the fan-out on the detector.

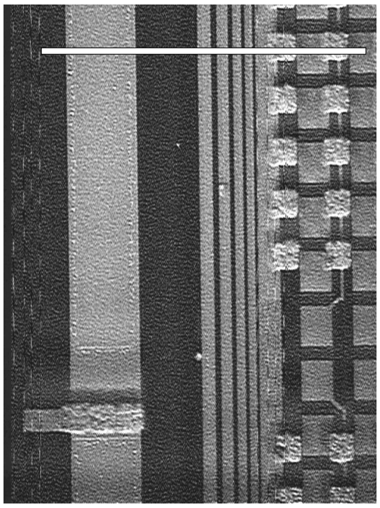

Figure 3.13
Photograph of part of a Si LAD1 detector. The pixels and guard-ring are surrounded by four floating guard-rings. The contact for the bias (metallisation visible at the left hand side) is only present on one side of the detector. The simulated cross-section is indicated by the white line in the upper part of the image.

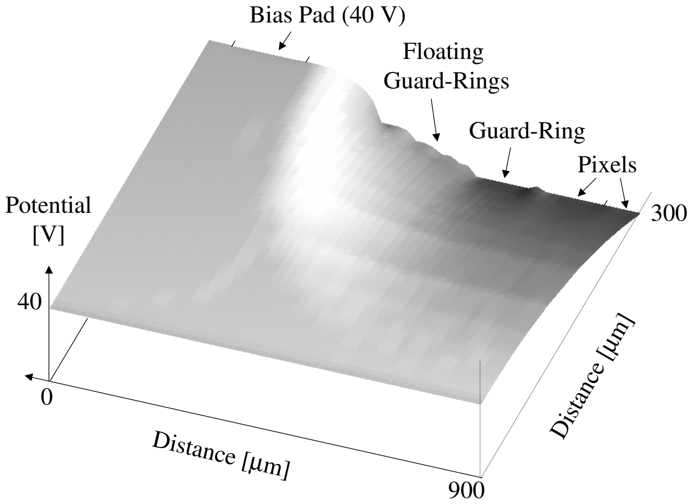

Figure 3.14: Simulated potential in a LAD1 Si detector. The n^+ bias pad is on the same side as the pixels, the ohmic back contact floats up to virtually the same potential, depleting the detector in the usual manner. The bias voltage is 40 V which fully depletes the detector.

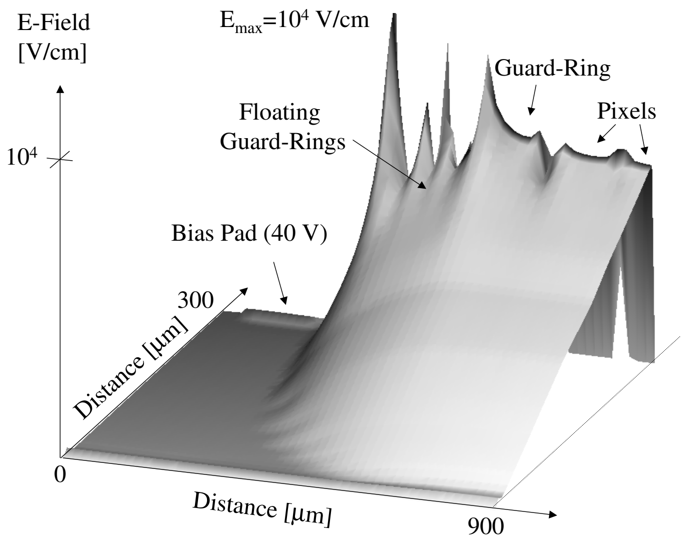

Figure 3.15: Electric field distribution in a LAD1 Si detector. For higher bias voltages the low electric field region (inactive area) is reduced. It is limited by the size and position of the front side n^+ implant.

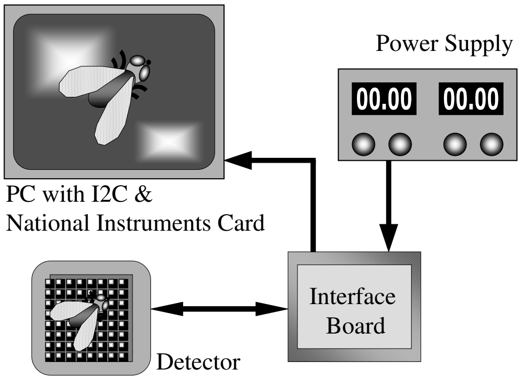

Figure 3.16
Experimental setup of the LAD1 system. The detector is connected to an interface board which supplies the power and is linked to a PC equipped with a National Instruments DAQ and an I2C card.

C^{++} and IDL software [IDL] is used to control the DAQ and I2C cards. The data are saved as 16 bit integers in binary format.

Chapter 4

Characterisation of the ERD1

Two different generations of modules are discussed in this chapter. The first is used to characterise general aspects such as the linearity, the adjustment among pixels and the performance in a synchrotron radiation source (SRS). Due to a significant improvement in the energy resolution of the new generation, the spectral performance and charge sharing is investigated with this very recent detector.

4.1 X-ray Sources used for the Characterisation of the ERD1

Some measurements were performed at the Daresbury SRS, the energy of the beam was varied and is given in the relevant section (4.2.3).
The following X-ray sources were used:

1) ^{241}Am X-ray source. The α-particles were shielded off, the X-rays of interest are listed in table 4.1.

Energy [keV]	13.93	17.61	21.00	26.35	59.54
Yield [%]	17.7	24.2	6.5	3.3	47.2

Table 4.1: Energies and yields of the relevant X-rays from an ^{241}Am source.

2) Variable X-ray source. The primary source is ^{241}Am which excites a target which then emits characteristic X-rays. The targets, energies and photon yields are given in table 4.2.

3) ^{55}Fe decaying to excited Mn emitting X-rays with energies given in table 4.3.

Target	Energy [keV]				Yield [γ's/s sr]
	$K_{\alpha 1}$	$K_{\alpha 2}$	$K_{\beta 1}$	$K_{\beta 2}$	
Cu	8.047	8.027	8.904	8.976	800
Rb	13.394	13.335	14.960	15.184	3000
Mo	17.478	17.373	19.607	19.964	7500
Ag	22.162	21.988	24.942	25.454	12000
Ba	32.191	31.815	36.376	37.255	12500
Tb	44.470	43.737	50.391	51.737	17500

Table 4.2: Target material, photon energy and yield of the variable X-ray source [Fir96].

Energy [keV]		
$K_{\alpha 1}$	$K_{\alpha 2}$	$K_{\beta 1}$
5.898	5.887	6.490

Table 4.3: X-ray energies emitted from an ^{55}Fe isotope, corresponding to the Mn K series.

4.2 The First Generation ERD1

4.2.1 Pulse Height Spectra and Linearity

The pulse height spectra of five targets from the variable X-ray source are shown in fig. 4.1. All spectra are normalised to their K_α photo peak. The lower amplitude peaks at the lower energy side of the K_α peaks are presumably due to the clock injection and are clock frequency and bias dependent. This assumption is not further investigated since this behaviour is cured in the second generation modules[1].
The linearity of the ERD1 was investigated using the peaks shown in fig. 4.1 and the ^{241}Am X-ray pulse height spectra. A plot of the ADC output voltage as a function of the input energy is shown in fig. 4.2. The data were obtained by fitting Gaussian functions to the photo peaks in the pulse height spectrum, using a least squares method. The deviation from the line fit is shown in fig. 4.3. The convex shape of the deviation may be due to non-linearity of the amplifier. This systematic error shows up in the reduced χ^2_{red} of the line fit, which is $\chi^2/\mathrm{dof} = 107$. Additional systematic error may arise from the assumed symmetrical (Gaussian) shape of the peaks of the pulse height spectrum. The larger error bars correlate with lower statistics. The maximum deviation from linearity is 0.5 keV (at 26.35 keV) or less than 2 %.
The energy resolution of the photo peaks from fig. 4.1 is plotted in fig. 4.4.

[1] They are not the Si escape peaks, since the energy difference from the main K_α peak varies and does not correspond to the Si K-X-ray (1.8 keV)

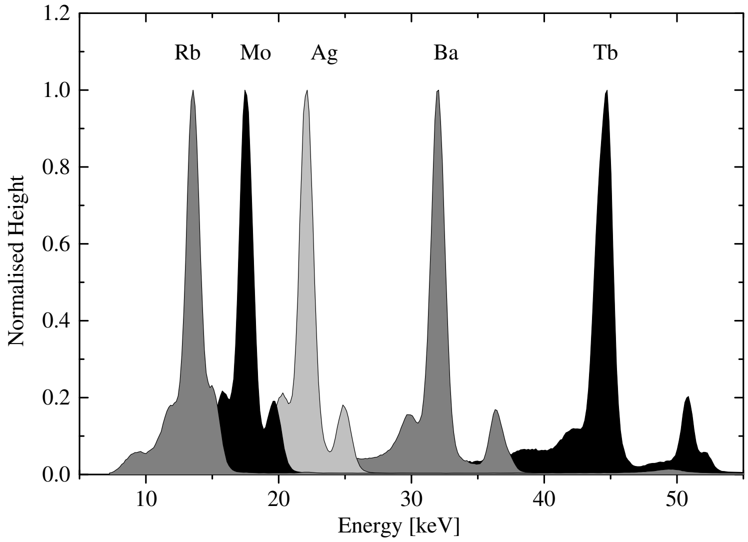

Figure 4.1: Normalised pulse height spectra of five targets from the variable X-ray source. The lower amplitude peaks at the lower energy side of the K_α photo peaks are presumably due to clock injection.

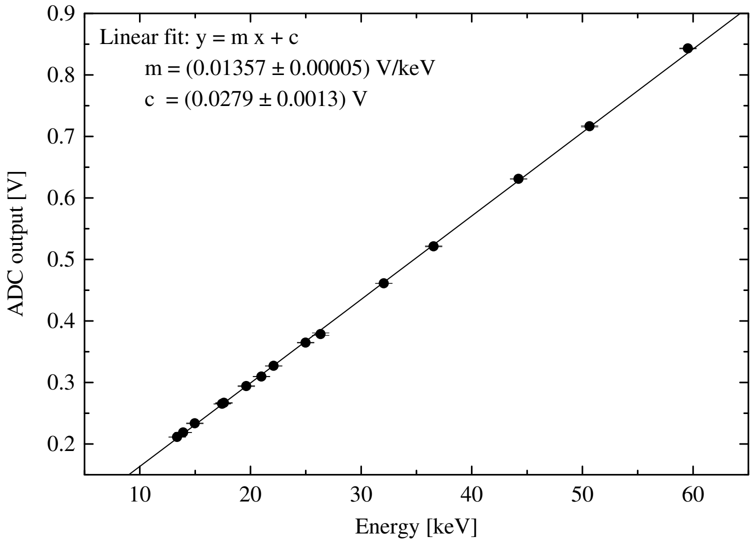

Figure 4.2: ADC output voltage plotted as a function of the X-ray energy. The line fit and extracted parameters are included in the graph.

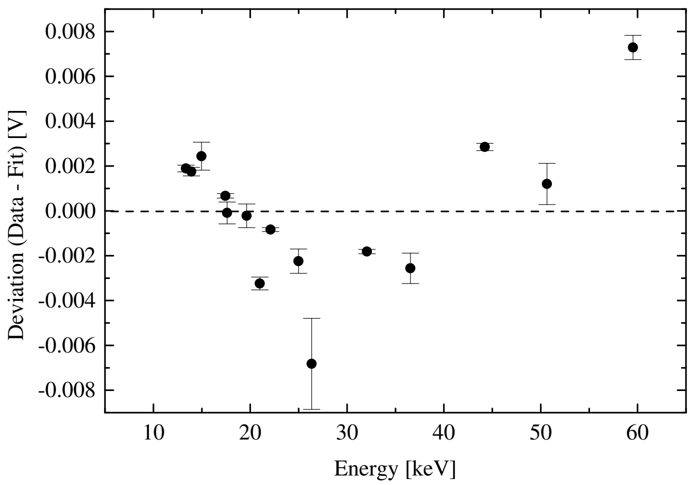

Figure 4.3: Plot of the deviation of the data from the fitted line. The convex shape may be due to non-linearity of the amplifier.

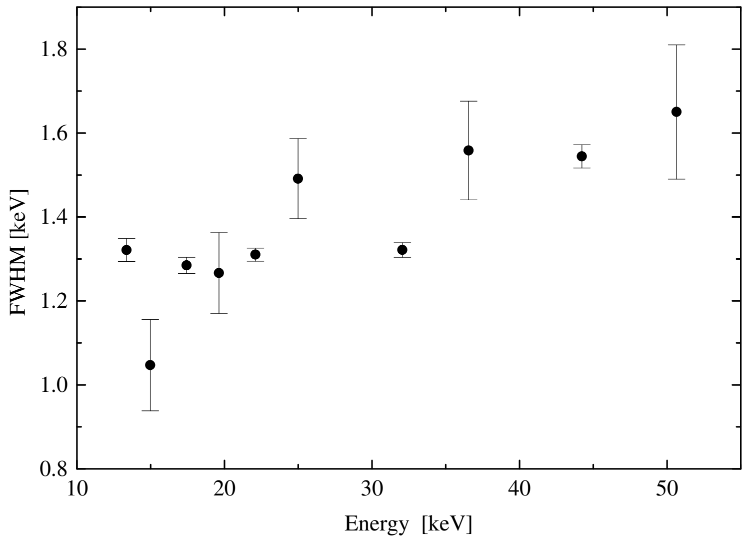

Figure 4.4: Energy resolution of the photo peaks from fig. 4.1.

4.2.2 Adjustment of the Pixel Variations

The ERD1 was designed for spectroscopic applications. Pixellating such a device brings the benefit of covering a larger area without increasing the detector capacitance, i.e. the noise. The drawback lies in the variation in response among pixels. Although identical in design, the differences between pixels, including the read-out (variation in the pixel capacitance, inhomogeneities in the detector and different gains or offsets of the pre-amplifiers), are significant and need to be taken into account. For a given photon energy the response of each pixel (output in volts) will differ, as shown in fig. 4.5, therefore the association of the output voltage to the photon energy (calibration) must be made separately for each of the 256 pixels. This then allows the calculation of the photon energy from the specific calibration of the pixel which was hit.

The separate calibration of each pixel is discussed in the following, including the investigation of the noise variation. Finally a spectrum of ^{241}Am γ's is shown after adjustment using the complete calibration data. The calibration used the K_α

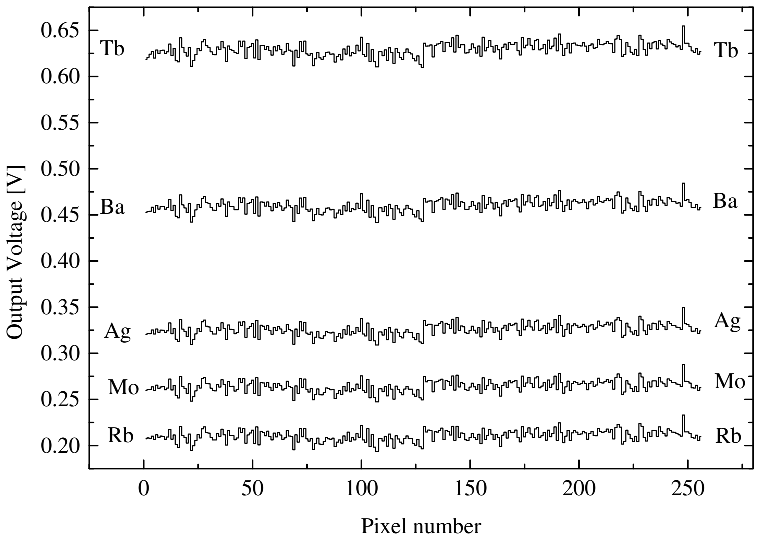

Figure 4.5: The peak position is plotted for the 256 pixels of the ERD1. The data show the variation among the pixels.

peaks of spectra discussed above. The variation in the peak position for the 256 pixels of the ERD1 is shown in fig. 4.5. In order to allow an adjustment the data sets must be highly correlated. That this is the case can be seen in fig. 4.5 and is confirmed by the correlation coefficients given in table 4.4. Apart from a variation in the peak position, pixels may also have different noise performances. This could result in a few pixels with particularly large noise dominating the overall energy

Correlated Data Sets	Correlation between Peaks	Correlation between Sigma
Tb-Ba	1.00	0.22
Tb-Ag	0.99	0.11
Tb-Mo	0.99	0.18
Tb-Rb	0.99	0.15
Ba-Ag	0.99	0.11
Ba-Mo	1.00	0.17
Ba-Rb	1.00	0.25
Ag-Mo	0.98	0.17
Ag-Rb	0.98	0.12
Mo-Rb	1.00	0.07

Table 4.4: Correlation coefficients for the various combinations of the calibration data.

resolution. Such pixels should be 'masked off'. Histogramming the standard deviation of the calibration peaks of each pixel allows the calculation of the spread and helps to identify noisy pixels. Such a histogram is shown in fig. 4.6 for the Mo data. The standard deviation in noise is 5 %. The maximum deviation in the data set corresponds to 3.6 σ or 18 %. The 5 % includes the variation expected from statistical and fitting errors. These contribute at the level of 2.4 %, leaving 4.4 % due to true pixel variation. All pixels were used, none was taken as being too noisy.

The correlation between the noise (sigmas) of the calibration peaks is given in table 4.4. In all cases these are positive, indicating that the performance of individual pixels vary, though not significantly since the correlation coefficients are small. The final adjustment was performed on an independent data set which was not used for the calibration. This was done by taking an ^{241}Am spectrum, which is shown in fig. 4.7. In the top part of the figure the unadjusted spectrum, obtained by simply adding the spectra of each pixel, shows a FWHM of 2.68$\pm$0.12 keV for the 13.93 keV peak. The more relevant comparison is between the adjusted spectrum (middle of fig. 4.7) and the performance of a single pixel (bottom of fig. 4.7). The FWHM achieved for the 13.93 keV peak is 1.658$\pm$0.079 keV and 1.613$\pm$0.010 keV for the adjusted and average single pixel respectively. The error for the adjusted spectrum was derived from the least-squares fit. For the average single pixel the variation in sigma over the 256 pixels was used to give an error. Not taking the errors into account would give a 2.8 % increase due to adjustment inaccuracies. However the values agree well within the errors.
The parameters of the calibration (line fit) of each pixel are histogrammed and shown with Gaussian fits in fig. 4.8. For both the offset and gain the variation

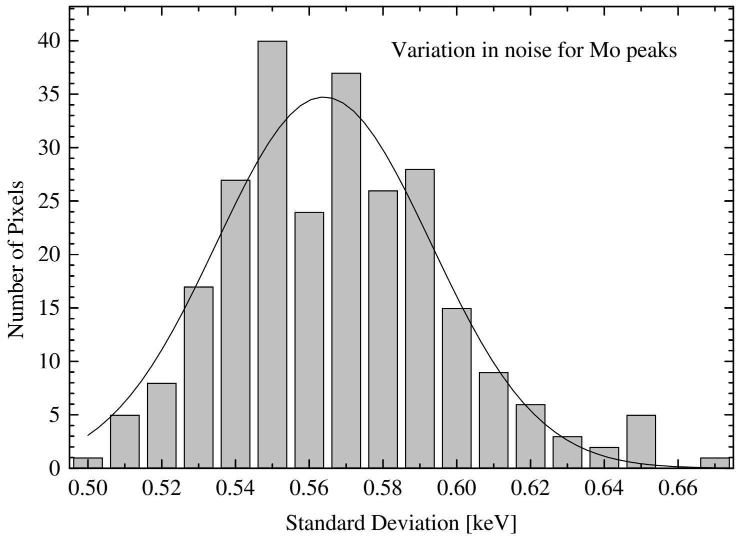

Figure 4.6: The spread in noise for the Mo data is plotted as a histogram, showing no particularly noisy pixels.

seem to be Gaussian. The offset is dominant which is also seen from the data shown in fig. 4.5.

4.2.3 Measurements at the Daresbury SRS

Tests with the ERD1 in a realistic operational environment were performed at the synchrotron radiation source (SRS) at Daresbury. Although not designed for the high fluxes of the SRS, the ERD1 was used as a detector for X-ray diffraction patterns while simultaneously acquiring the energy spectrum. The beam was focussed on a rotating $KNbO_3$ crystal powder behind which the ERD1 was mounted at a distance of about 40 cm. A lever arm allowed a rotation of the ERD1 with respect to the $KNbO_3$ crystal, in order to scan for diffraction maxima. Neither a vacuum nor any form of collimation was used. The 16 x 16 pixel matrix of the ERD1 gives a 2-dimensional image while taking the energy spectrum. Fig. 4.9 shows such an image of two diffraction lines. At the upper edge of the image it can be seen that the detector was shielded by the Al casing in which the hybrid is mounted. A plot of the same data is shown in fig. 4.10, in which the y-axis (mean intensity) was calculated by averaging the counts of the columns of pixels in fig. 4.9. The pixel size of 300 μm gives a peak separation of about 2 mm.

For these measurements the beam energy was set to 12 keV. Displaying the energy spectrum of the above data shows the peak at 12 keV, as plotted in the top

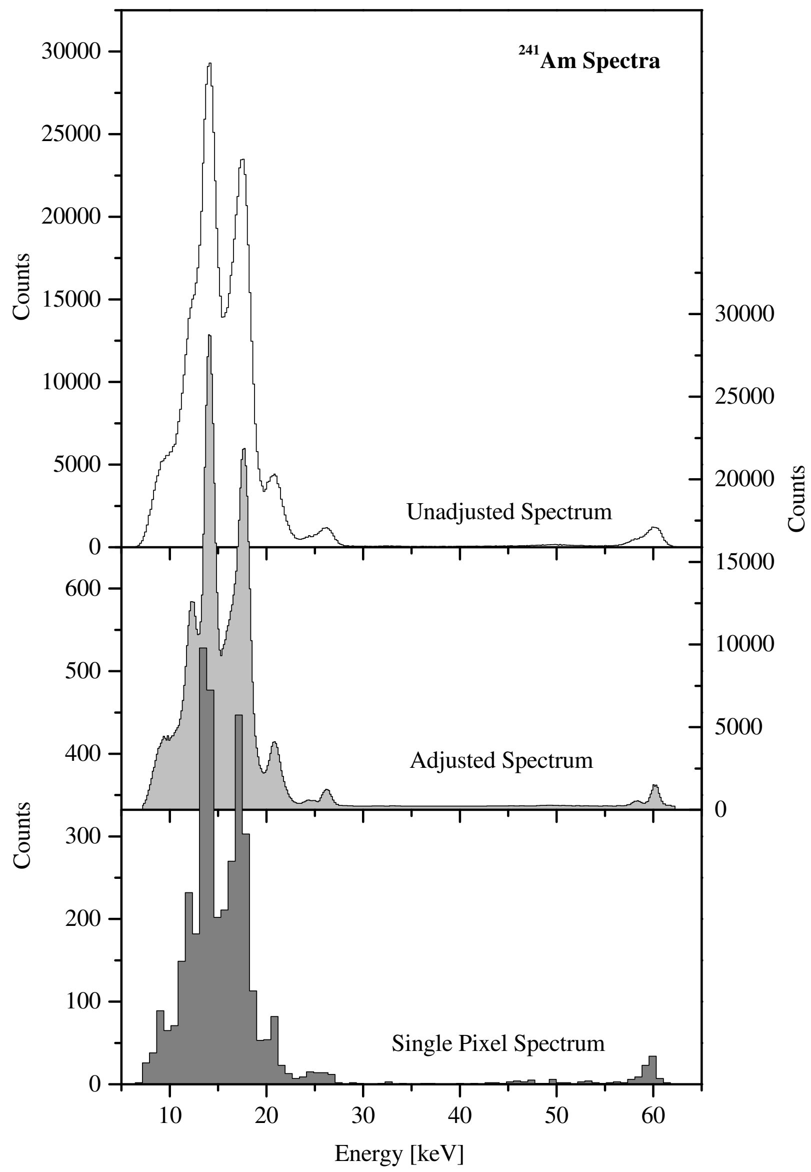

Figure 4.7: The graph shows the unadjusted ^{241}Am spectrum in the top layer, the adjusted spectrum in the middle and a single pixel spectrum in the bottom layer. The resolution of the adjusted spectrum is comparable to that of a single pixel.

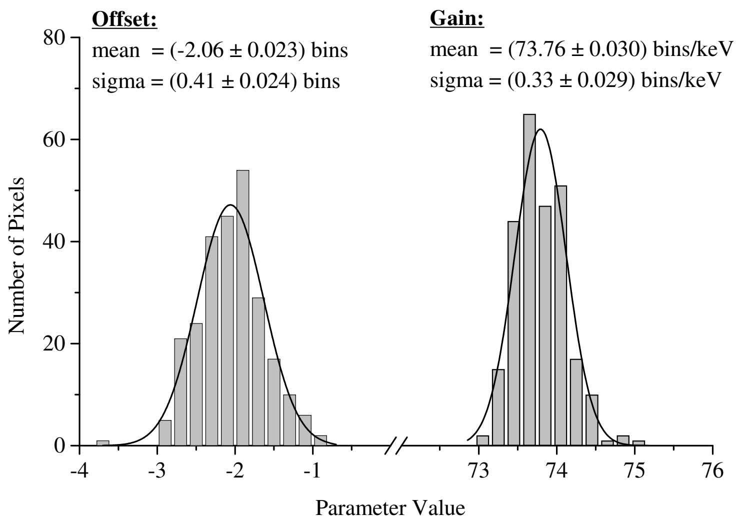

Figure 4.8: Histograms of the fit parameters. The variation in the offset is dominant.

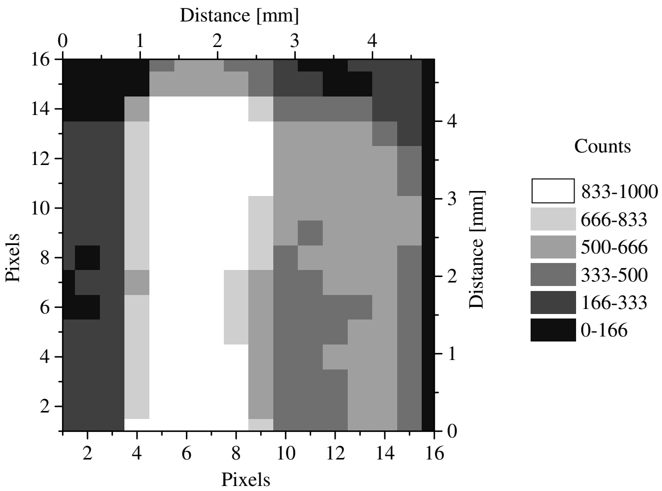

Figure 4.9: Image of two X-ray diffraction lines of a $KNbO_3$ crystal.

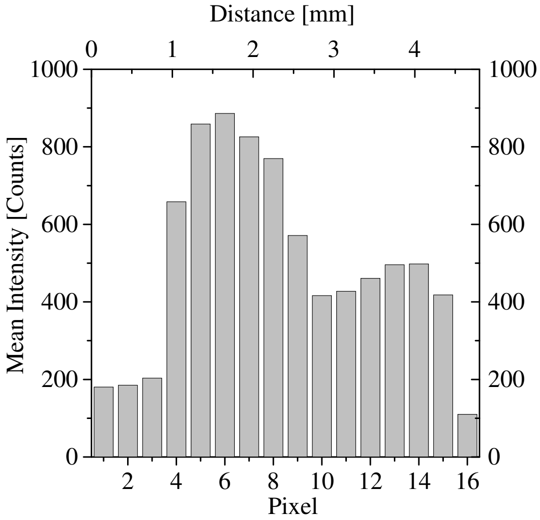

Figure 4.10
The graph shows a plot of the mean intensity vs. distance measured with the ERD1. The data are the same as used for the image shown in fig. 4.9.

spectrum in fig. 4.11. The spectra acquired at beam energies of 20 keV and 25 keV are shown in the middle and lower parts of fig. 4.11, respectively. The peak at 12 keV is clearly wider than those at 20 and 25 keV. This peak is extracted from the same data as the intensity lines. The X-ray flux for these lines is so high that pile-up occurs, so that the charge from more than one photon is integrated within the shaping time, occasionally, resulting in a tail at higher energies and a broadening of the peak. The energy spectra at 20 and 25 keV were taken outside the high intensity lines and therefore do not show any pile-up. For energies above 19 keV the fluorescence of the Nb can be seen at 16.6 keV, which corresponds to its K_α line.

4.2.4 Imaging Properties

The 256 pixels are insufficient to allow useful imaging of structured objects. The detector was mounted on an x-y stage to scan an image of a ball point pen, shown in fig. 4.12. A standard dental X-ray tube was used at 60 kVp anode voltage, giving a bremsstrahlung spectrum peaking at around 30 keV. The lower energy part of the spectrum is cut off by an absorber, so the lowest energy X-rays are around 10 keV. The spectrum of the tube is obtained by using the absorption efficiency of the detector to de-convolute the measured spectrum. Both are shown in fig. 4.13.

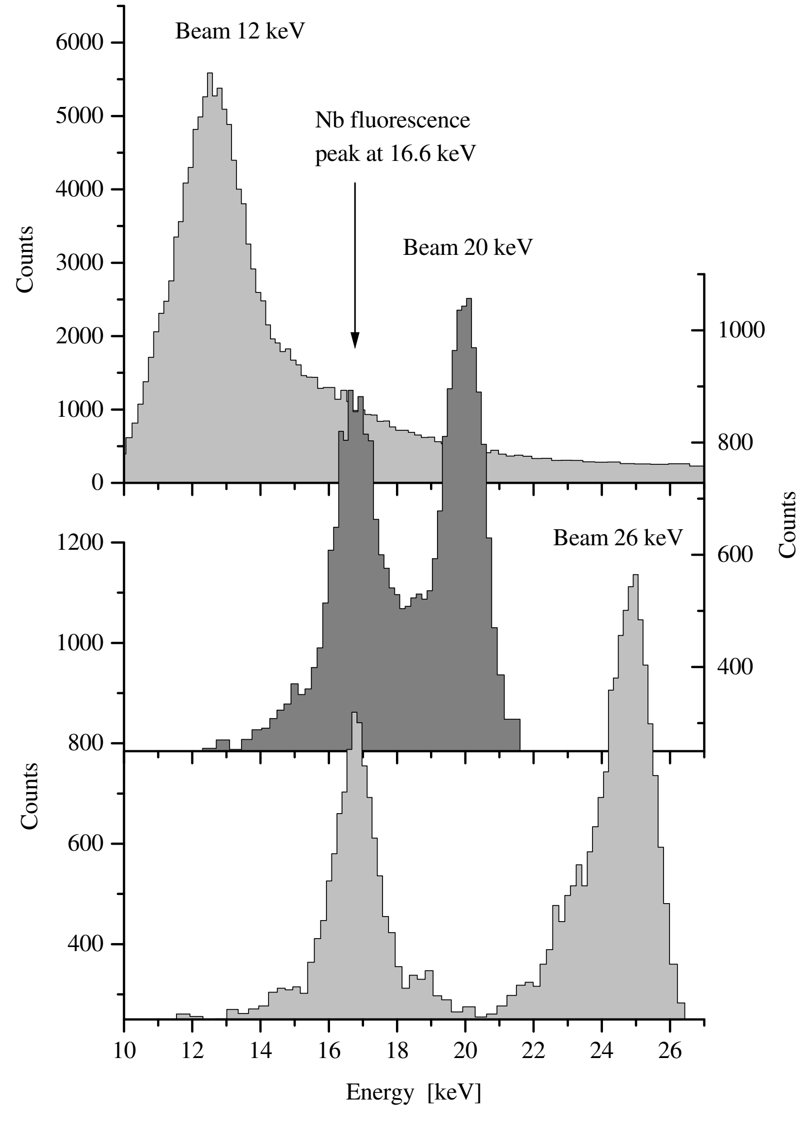

Figure 4.11: Energy spectra plotted for various beam energies. The peak at 16.6 keV is the fluorescence peak of Nb. The top spectrum is the energy spectrum of the diffraction maxima in fig. 4.9.

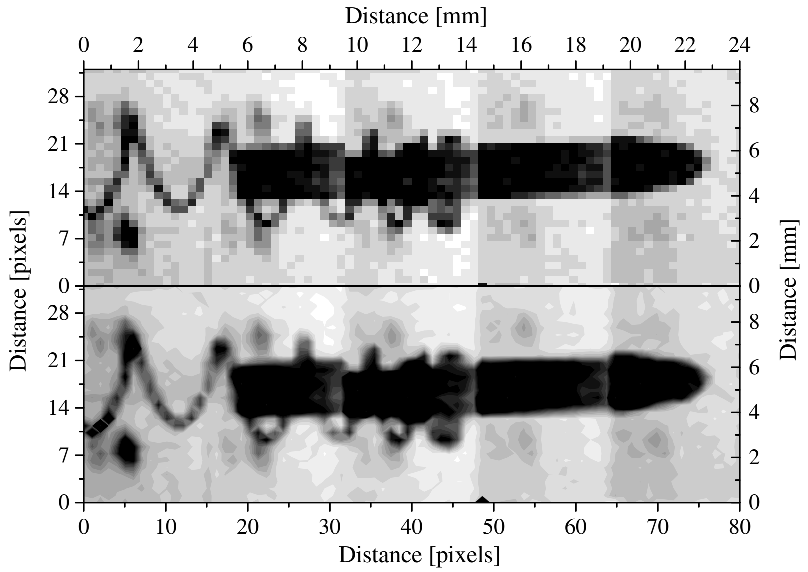

Figure 4.12: Scanned image of a bull point pen. The upper image is the direct data, the lower image is a contour plot. The image is tiled from 5 x 2 acquisitions.

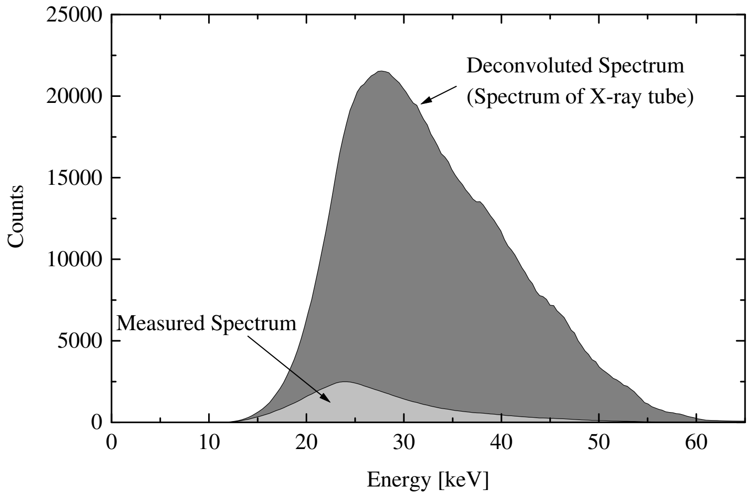

Figure 4.13: Pulse height spectrum of the X-ray tube and the measured spectrum. The absorption efficiency of the detector was used to deconvolute the measured spectrum to give the spectrum of the X-ray tube.

4.3 Dash-E

4.3.1 Description of the System

The ERD1 system as described above has several weaknesses:

1. The minimum threshold is limited by clock injection to a level around 10 keV.

2. The noise is increased by the injection.

3. Only the pixel hit is read out and no information on any other channels is available.

4. The electronics is uni-polar and requires hole collection.

A new version of the chip has therefore been fabricated, improving the noise performance and reducing the injection to about 4 keV. This new system is called[2] Dash-E, the following features have been changed or added:

1. The shaping time is increased to 4 μs.

2. The SHAMROC can be switched to read signals of either polarity (software controlled).

3. Optionally all channels on a SHAMROC can be read out if one pixel has been hit (software controlled).

4. The feedback capacitance is reduced to 25 fF and can be increased to 250 fF by adding a capacitor (software controlled).

All the problems apparent in the ERD1 have been cured.

4.3.2 Energy Resolution

The pulse height spectra of various X-ray sources are shown in fig. 4.14. The roughness of the background reflects the statistics of each spectrum. The cut-off at the lower energy end is determined by the threshold used for the data acquisition.
Two peaks are observed in the background of the Ba spectrum. The higher corresponds to the Ag energies and is assumed to be due to known contamination of the variable X-ray source. The origin of the lower peak is unknown.
The FWHM for each energy are plotted in fig. 4.15. The data for this plot were obtained by fitting multiple Gaussian functions to the photo peaks. The two K_α lines are taken into account by imposing appropriate constraints for the fit. The

[2]ERD2 is a different development within the IMPACT project and can therefore not be used. Dash-E is derived from 'ERD1.

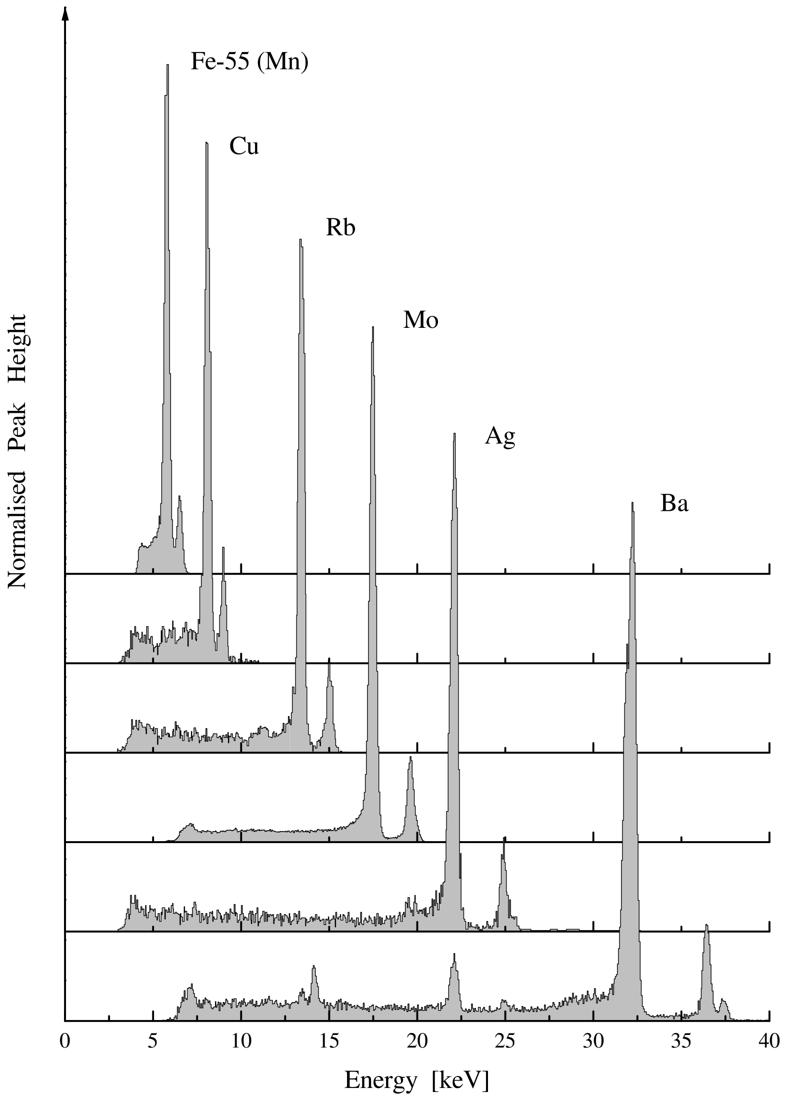

Figure 4.14: Pulse height spectra for various X-ray sources. The peak heights are normalised, the background roughness depends on the statistics.

standard deviation is forced to be equal, the difference in the peak positions is imposed and the areas are constrained to the known values [Dys90] with a tolerance of about 2 %. The fit to the sum of two Gaussian functions, due to these constraints, requires only three free parameters to be fitted and no additional degrees of freedom are added[3]. The square of the FWHM has a linear dependence on the

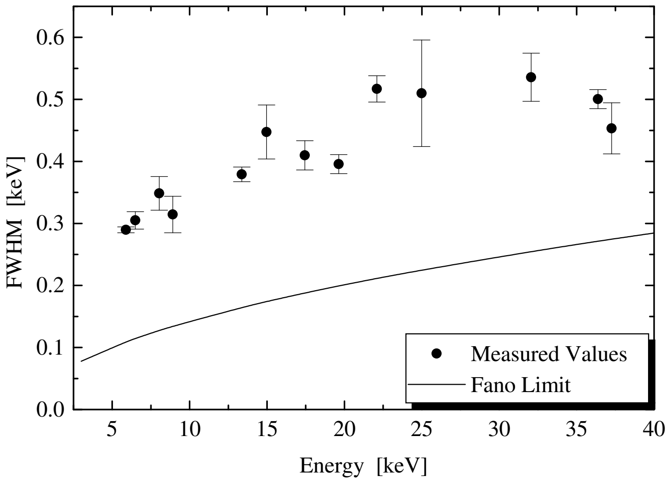

Figure 4.15: FWHM of the photo peaks shown in fig. 4.14. The Fano noise limit is plotted as a line.

photon energy and can be represented as the sum of in a constant (square of electronic noise) and a linear contribution [Kno00], as shown in fig. 4.16 with a line fit. The electronic noise extracted from the fit is (224 ± 64) eV. The gradient of the linear fit $(0.00608 \pm 0.00064$ keV) can not be explained by a Fano factor of 0.125 as given in ref. [Lec96]. Since the Si detector is expected to have 100 % CCE, charge loss is not expected to contribute. However a low energy tail is present, suggesting some charge loss. The high background increases with decreasing depletion width and might have significant contributions from the processing electronics.
Both these effects are not yet explained satisfactorily.
The peak-to-background ratio is plotted in fig. 4.17. The data of the two lowest X-ray sources (Cu and ^{55}Fe) are not included because the background is cut off by the threshold set for the data acquisition. The background increases with increasing photon energy. This does not, however, allow to conclude that there is necessarily an energy dependence of the background. The effect may be due to

[3]Taking the two K_α peaks into account improves the resolution by about 10 % in average.

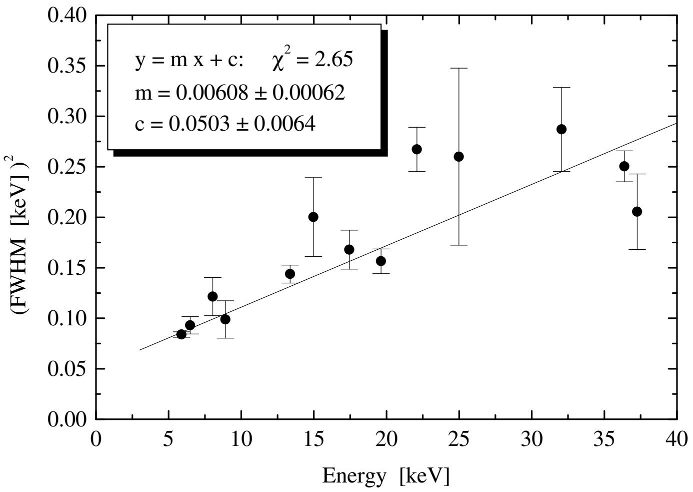

Figure 4.16: Plot of the FWHM squared with a line fit. The electronic noise contribution extracted from the fit is (224 ± 64) eV.

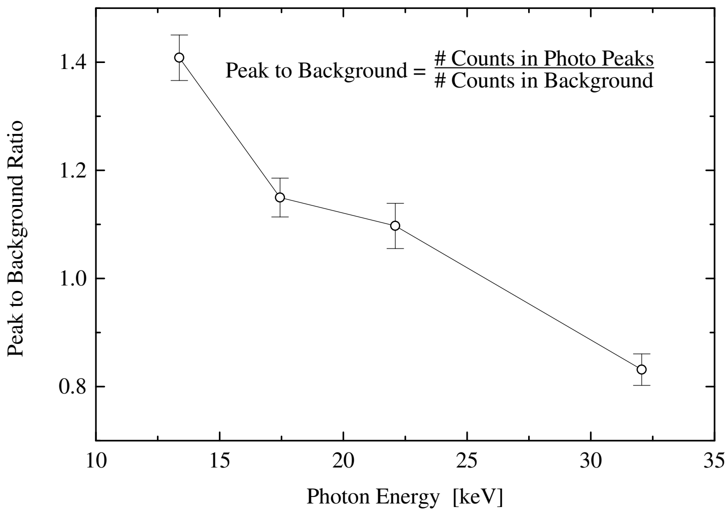

Figure 4.17: Peak-to-background ratio. The background increases with increasing photon energy.

the different rates of the absorbed X-rays.
The data were acquired by fitting Gaussian functions to the K_α and K_β peaks which gives the area of the photo peaks. For the evaluation of the background, a line was fitted to the data below the K_α peak. The background area was then calculated by integrating the fitted line from zero to the K_α peak energy. This eliminates the influence of the threshold which cuts the background at different levels.

4.3.3 Variation among Pixels

The pedestals are calculated from the same data files as are used for the investigation of charge sharing, described in the following section. Several hundred values with no signal charge are averaged to acquire the offset value for each pixel (A cut on the signal height defines pixels with signal and those without.). The pedestals are plotted with the standard deviation in fig. 4.18. These values are reproducible

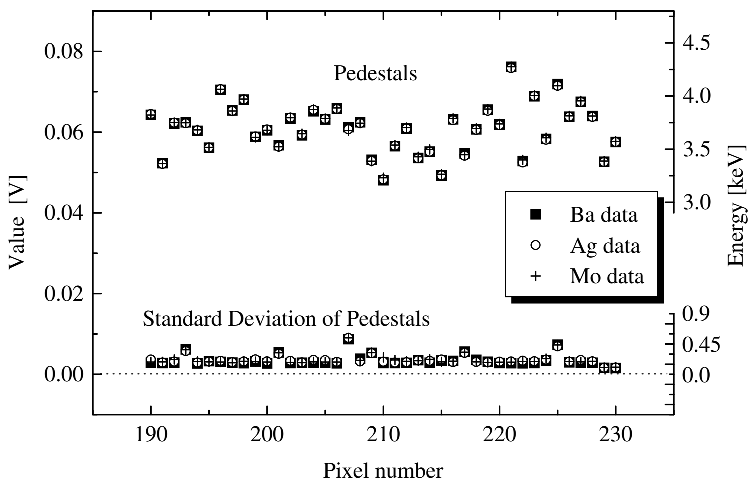

Figure 4.18: Pedestal values plotted with their standard deviation. The values are reproducible from different sets of data.

and the variation of the pedestal values for different data files is 5.4 ± 2.6 eV, which is negligible.
The distribution of the pedestal values is not Gaussian, as illustrated by the two examples shown in fig. 4.19. Extracting the electronic noise by fitting a Gaussian to the lower peak in the noise distribution, gives (228 ± 29) eV FWHM electronic noise, which is consistent with the result gained from the pulse height spectra.

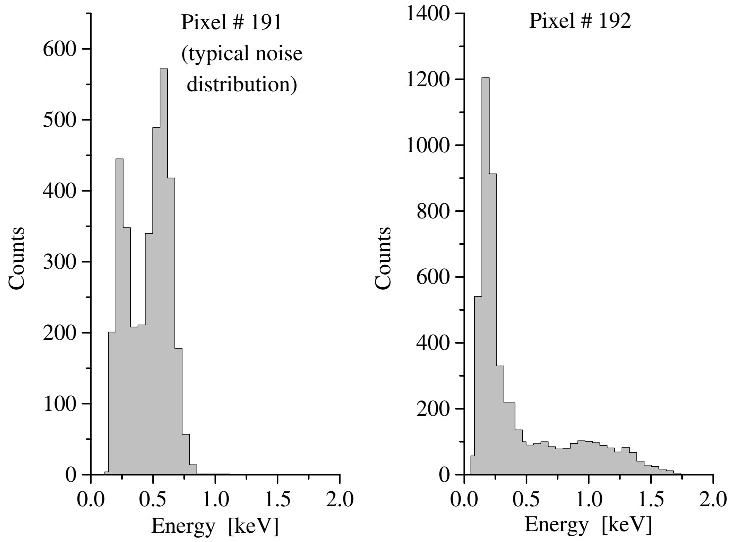

Figure 4.19: Distributions of pedestal values, which are not Gaussian. The example on the left is representative for most pixels.

Common mode noise is sampled with a separate channel and subtracted. Any remaining common mode noise results in an increased correlation between a set of data where all channels have been read out. From several thousand correlation coefficients calculated from the Mo, Ag and Ba data, the mean correlation is 0.0232 ± 0.0022. Common mode noise does not significantly contribute to the observed energy resolution.

When evaluating any data the pedestal values are subtracted and therefore all pixels are expected to have the same calibration. For all of this analysis it is assumed that the variations in the pixel performance are due to different offset and that all pixels have the same gain, which is justified by the results of the previous section.

4.3.4 Charge Sharing

Charge sharing can be investigated by reading out all pixels for each event. In order to validate the results it must be assumed that the illumination over any two pixels does not change significantly. The variable X-ray source is collimated to a circular spot size of about 4 mm diameter, over which the illumination is homogeneous [Pas98]. The area used for the investigation of charge sharing is a section of 2.4 by 1.5 mm^2 which is significantly smaller than the beam size.

The analysis includes single, double and treble clusters. For each event the pixel with the maximum signal is defined as the pixel hit. The eight surrounding neigh-

bours are selected and if one or two values exceed a set threshold a double or treble event is registered, respectively. Edge pixels are discarded since charge sharing may occur with the guard ring which would falsify the results. A minimum signal height is required in order to trigger an event so that noise counts are rejected.
The fractions of single, double and treble events are plotted for the six considered energies in fig. 4.20. Due to the large pixel size the single clusters dominate. At low threshold the noise contributes significantly to double and treble clusters. Clustering due to the noise is shown in fig. 4.21. The data were taken from the Ba measurement by selecting a pixel which did not contribute to the signal. At a threshold of 2 keV random multi-clustering (≥ 2 clusters) occurs at a level of (2.7 ± 0.3) %. This threshold was used to plot the pulse height spectra of single, double and treble clusters, which are shown in fig. 4.22-4.27 for the various X-ray sources.

For all sources the treble cluster spectra have such low statistics that no peaks are clearly visible. Treble clustering is negligible, which is also seen from fig. 4.20 and will not be discussed any further. The Ba, Ag, Mo and Rb sources show clear characteristic pulse height spectra for the double clusters. However Cu and ^{55}Fe (Mn) do not show a double cluster spectrum resembling their emission lines. The dominant cause is the level of the threshold applied for the data acquisition. As seen from the single pixel spectra (fig. 4.26 and fig. 4.27) the lowest amplitude events are close to the photo peaks, which leaves only a small range of charge shared events to be acquired. The double cluster for Cu and ^{55}Fe (Mn) are due to random, coincidental double hits and can not be used for further analysis. In order to acquire successfully all occurring double clusters it is necessary that the threshold is below 50 % of the photo peak energy. This is the case for the Rb, Mo, Ag and Ba data. The single and double cluster fractions for these four sources are plotted as a function of the threshold for charge sharing in fig. 4.28 and fig. 4.29, respectively.

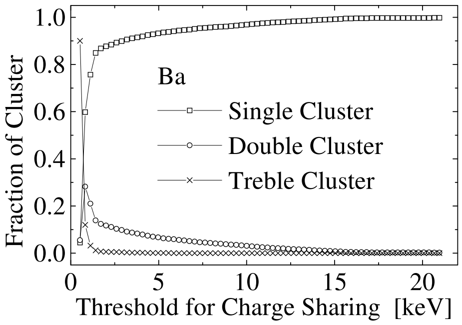

(a) Ba data

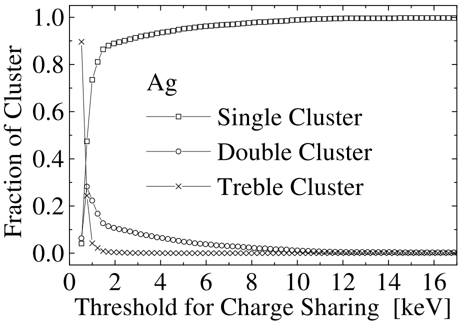

(b) Ag data

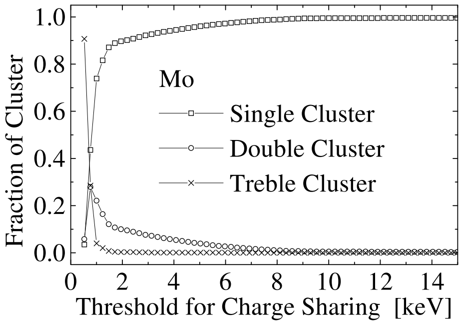

(c) Mo data

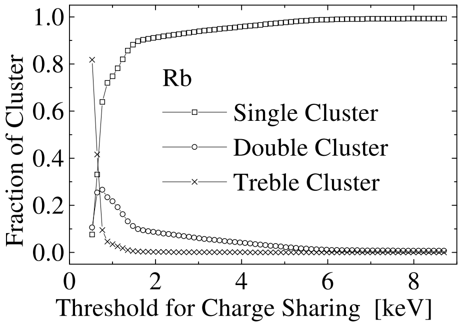

(d) Rb data

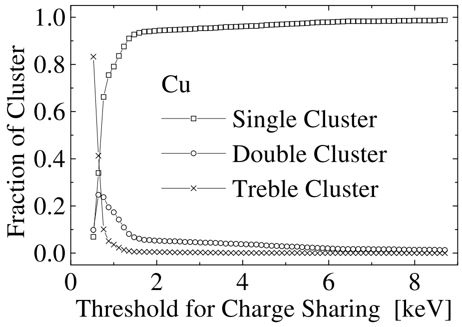

(e) Cu data

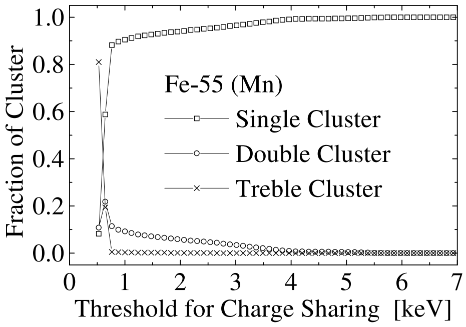

(f) ^{55}Fe (Mn) data

Figure 4.20: Fraction of single, double and treble clusters for different energy X-rays. The lowest data point in each spectrum is equal to the pedestal value and is largely dominated by noise. Single clusters are dominant due to the large pixel size of 300 μm.

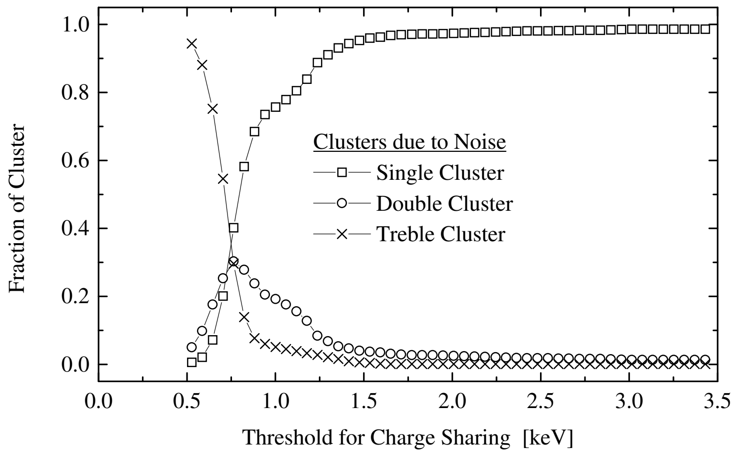

Figure 4.21: Clusters due to noise. The pedestal values are around 0.5 keV. Random multi-clusters occur at a level of (2.7 ± 0.3) % at a threshold value of 2 keV.

The data are the same as used for fig. 4.20 but now plotted to illustrate the energy dependence of charge sharing. For a threshold of 2 keV the energy dependence of charge sharing is shown in fig. 4.30. The likelihood of a photon depositing a certain energy in a neighbouring pixel increases with increasing photon energy.

The above charge sharing uses the absolute value of shared energy (charge), which leads to the increase in charge sharing for higher photon energies. Fig. 4.31 shows the probability of sharing a certain fraction of charge (20 % of the K_α peak value) as a function of the photon energy.

The fraction of charge shared decreases with increasing photon energy. This implies that diffusion is the dominant effect. Diffusion influences the width of the charge cloud approximately in proportion to the distance the charge carriers travel inside the detector. Because the detector is illuminated from the back the lower energy X-rays generate charge further away from the pixellated contact, on average. The charge generated by a lower energy X-ray has therefore, on average, more time to diffuse and is more likely to be shared.
The width of the charge cloud is also influenced by the range of the photo electron. This effect contributes to an increase in charge sharing with increasing photon energy and is apparently less significant.

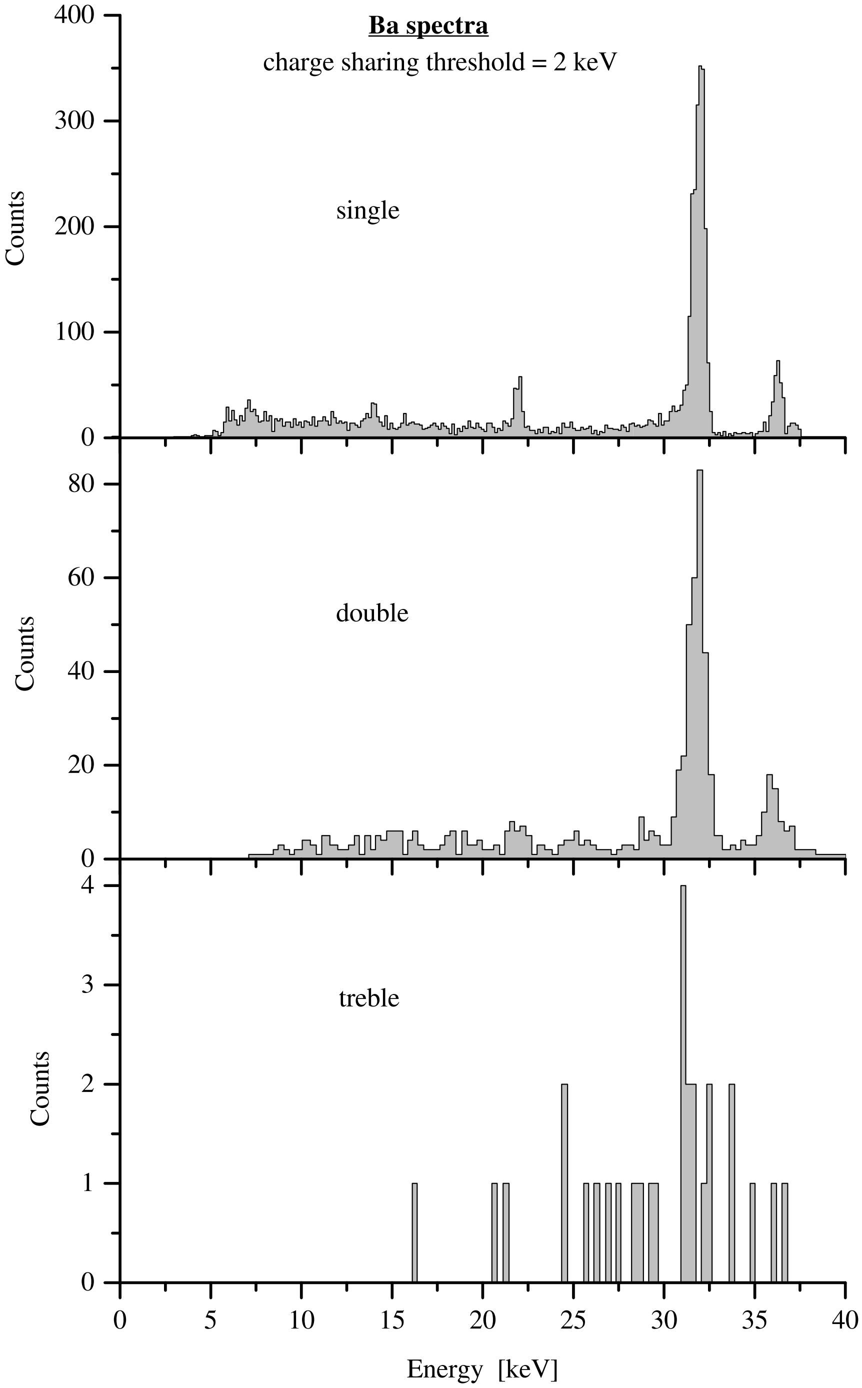

Figure 4.22: Single, double and treble cluster spectra of Ba for a threshold value for charge sharing of 2 keV.

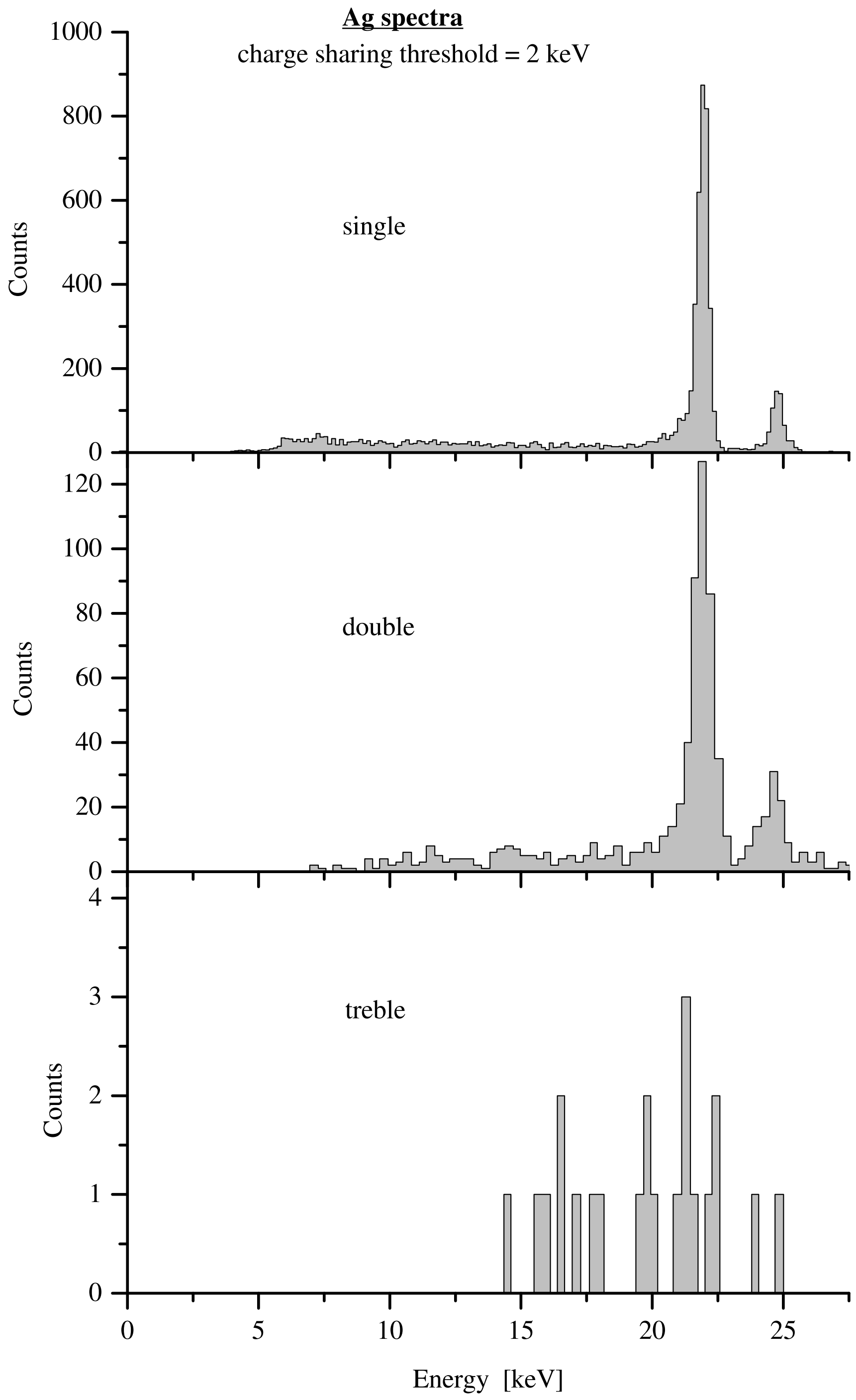

Figure 4.23: Single, double and treble cluster spectra of Ag for a threshold value for charge sharing of 2 keV.

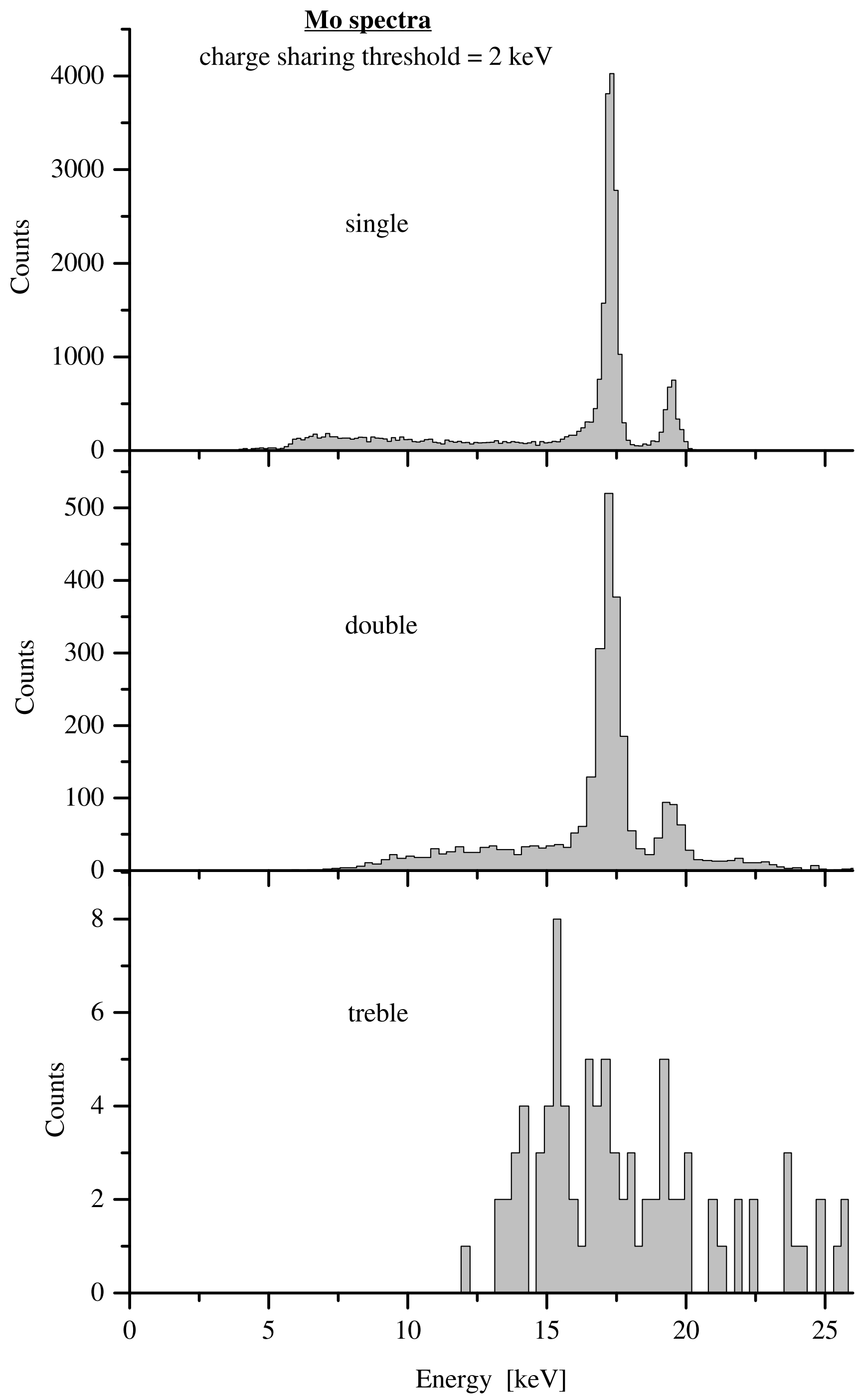

Figure 4.24: Single, double and treble cluster spectra of Mo for a threshold value for charge sharing of 2 keV.

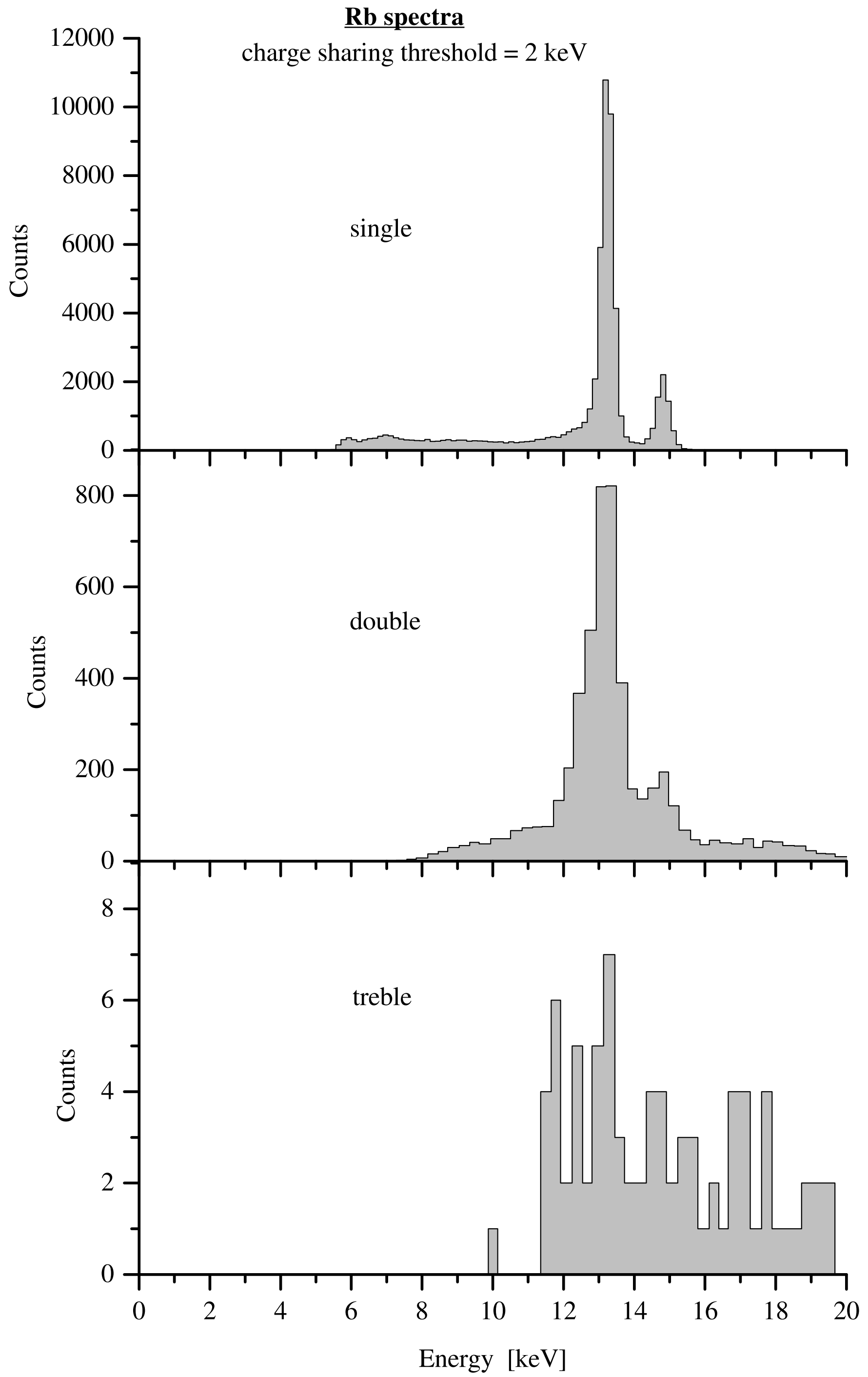

Figure 4.25: Single, double and treble cluster spectra of Rb for a threshold value for charge sharing of 2 keV.

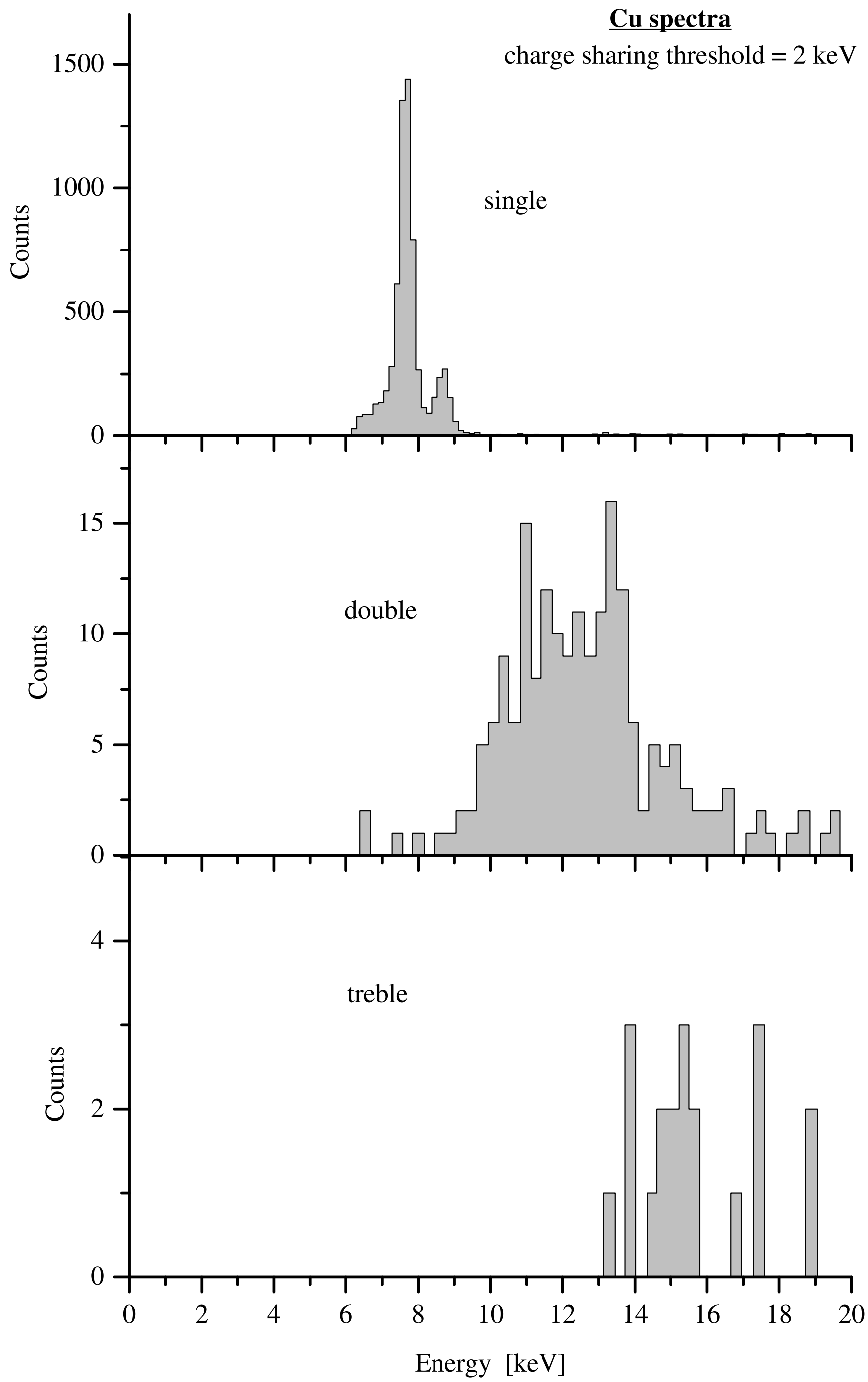

Figure 4.26: Single, double and treble cluster spectra of Cu for a threshold value for charge sharing of 2 keV.

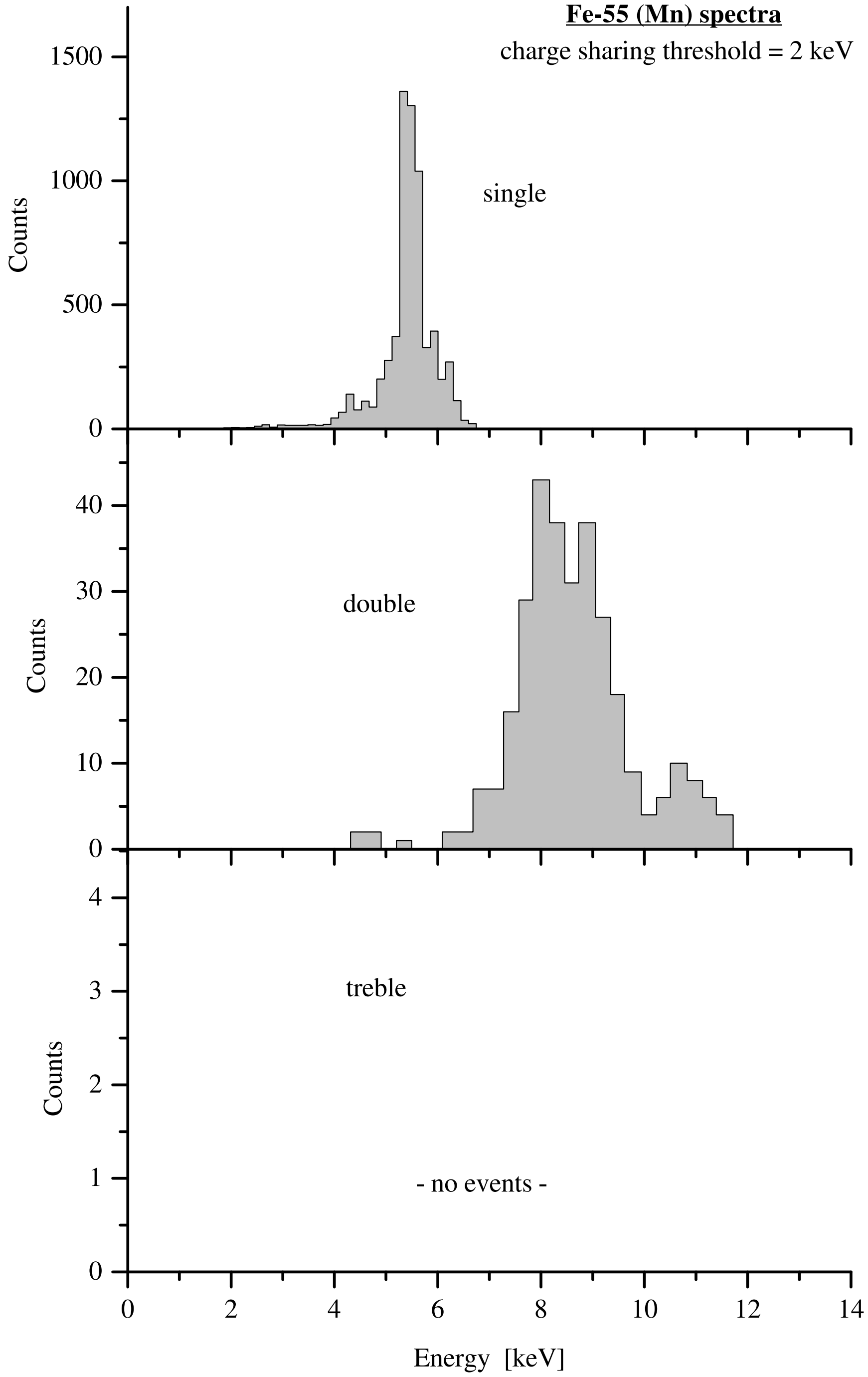

Figure 4.27: Single, double and treble cluster spectra of ^{55}Fe (Mn) for a threshold value for charge sharing of 2 keV.

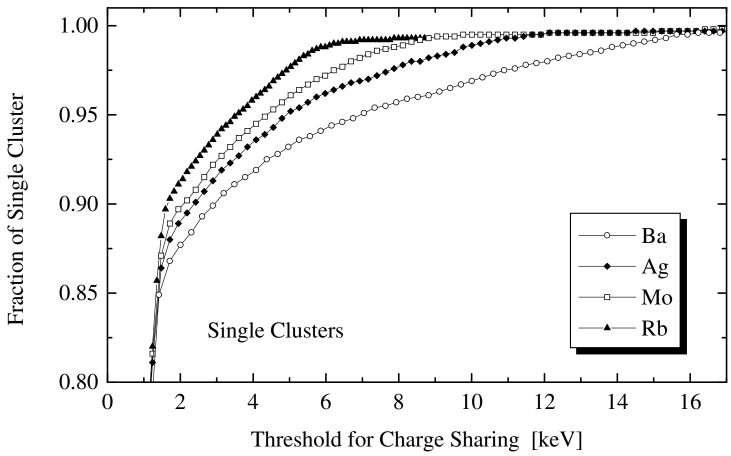

Figure 4.28: Threshold dependence of the single clusters for the Ba, Ag, Mo and Rb data.

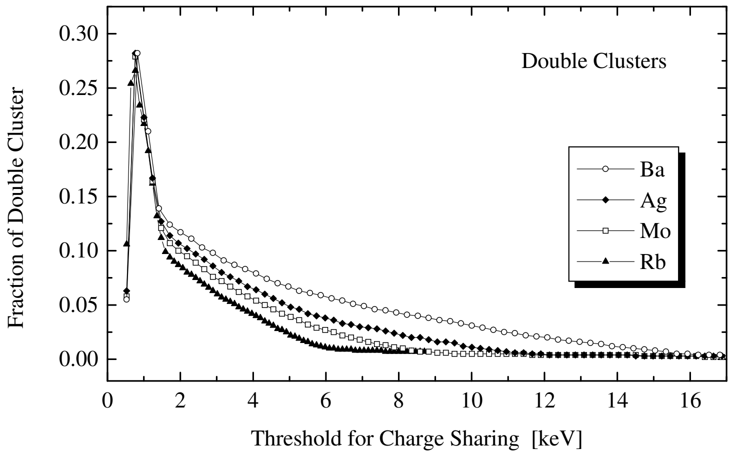

Figure 4.29: Threshold dependence of the double clusters for the Ba, Ag, Mo and Rb data.

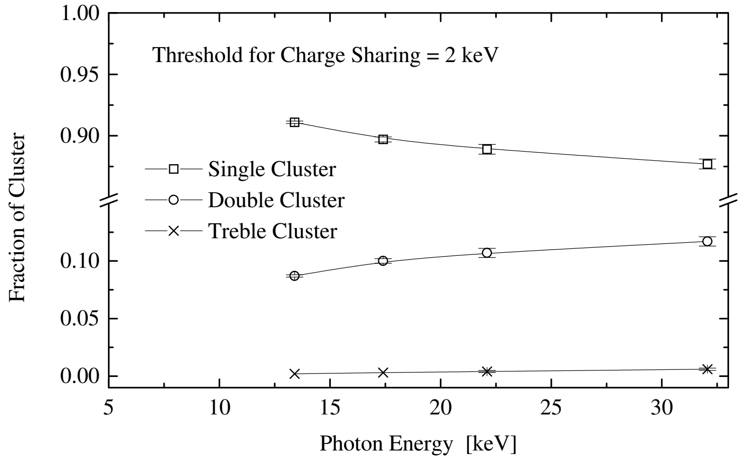

Figure 4.30: Energy dependence of charge sharing defined as the amount of energy shared. The increased multi clustering with higher energies is due to the higher energy of the primary photo-electron.

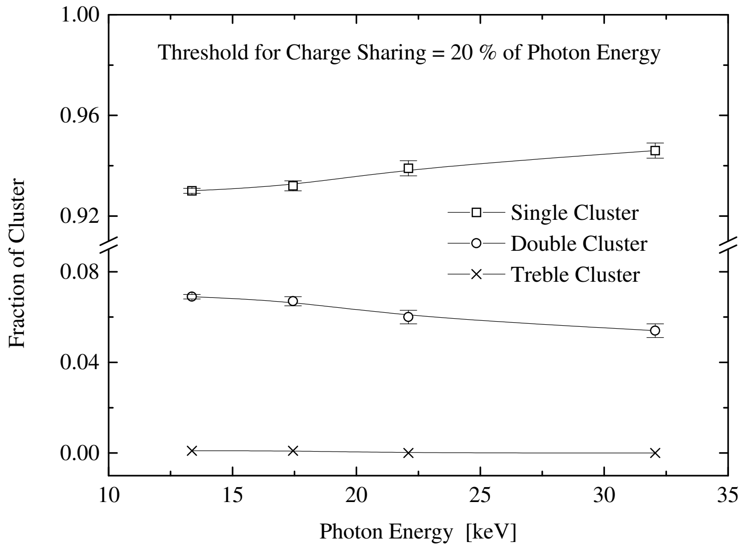

Figure 4.31: Energy dependence of charge sharing defined as the fraction of energy shared. The decrease in charge sharing with higher photon energy implies that diffusion is the dominant effect.

4.3.5 Extraction of the Charge Distribution

Relation between the Experimental Data and the Charge Distribution

All the above results are specific to the detector system. Of general interest are the distributions of the charge clouds. These are not directly available but can be extracted from the data.
The data containing the relevant information are those plotted in fig. 4.29. These data give the probability of sharing a certain energy or more. An illustration of the relation of these data to the average charge cloud density $f''(x, y)$ is given in fig. 4.32 which shows a possible distribution of the signal from a homogeneously illuminated pixel, given by the integration of $f''(x, y)$ over the pixel area. Neglecting

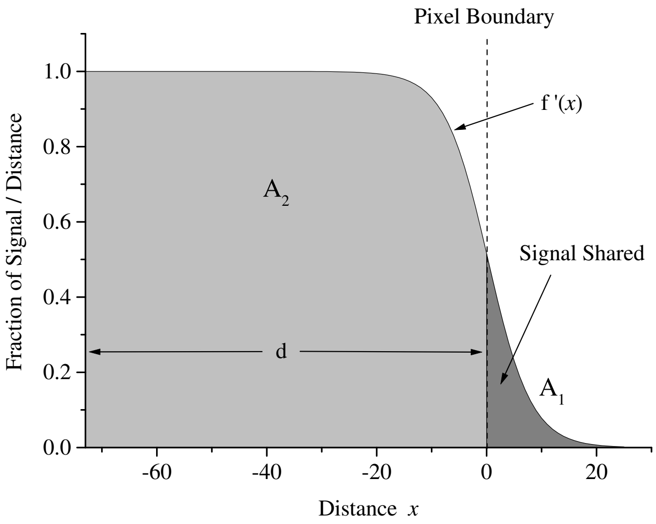

Figure 4.32: Distribution of the signal across a homogeneously illuminated pixel.

corner effects reduces the problem to one dimension ($f''(x, y) \rightarrow f''(x)$). Accordingly fig. 4.32 in effect shows a perpendicular cut through a pixel, with

$$f'(x) = \int_x^\infty f''(x')\, dx' \tag{4.1}$$

representing the signal distribution. If A_1 and A_2 are the amounts of signal shared and seen on the pixel, respectively, then the fraction of charge sharing is $f = A_1/(A_1 + A_2)$, which is what is acquired experimentally.

$$f(x) = \int_x^\infty f'(x')\, dx' \tag{4.2}$$

where $f(x)$ corresponds[4] to the data plotted in fig. 4.29. So the shape of the signal distribution $f''(x)$ is the second derivative of the experimental $f(x)$.
The experimental data give the fraction of charge sharing but do not contain any distance information. This is gained by multiplying the experimentally acquired fraction for charge sharing f by the overall signal known from the pixel dimensions. For the normalised signal in fig. 4.32 the total area is $A_1 + A_2 = d$, where d is the region of a pixel associated with the edge. For the 1-dimensional case of fig. 4.32, a cut through the pixel would show charge sharing on either side of the pixel boundary. Each boundary would be associated with half the pixel width, which in the case of the ERD1 is $d = 300/2$ μm=150 μm. Since the pixels are actually 2-dimensional charge sharing occurs at all four sides of the pixel, thus neglecting the corners, $d = 300/4\,\mu\text{m} = 75\,\mu\text{m}$.

Theoretical Model of the Charge Distribution

In principle the charge distribution $f''(x)$ can be extracted by taking the second derivative of the experimental data. However the variations in the data make a direct differentiation inaccurate. Therefore a simple model is used to fit the data, which allows the fitted function to be differentiated.
Consider the following model of the signal distribution from the photon interaction: Photo electrons which are emitted from the same point in the same direction are assumed to have a constant probability of depositing their energy within any distance x. This leads to an exponential attenuation of the deposited energy as a function of the distance x from the emission point,

$$f''(x) \propto e^{-\frac{x}{r_0}}, \tag{4.3}$$

where r_0 has the meaning of the range of the photo-electron. Since the absorbed photons are assumed to be unpolarised this distribution is azimuthally symmetrical. Approximating the angular distribution of the photo-electrons with equal probability for all angles[5] leads to a spherical symmetry which introduces a factor of $1/r_0^2$ in the signal density distribution. So for a normalised signal

$$f''(x) = \frac{1}{r_0^2} e^{-\frac{x}{r_0}}. \tag{4.4}$$

Including the photon energy E_γ with the knowledge that the maximum signal shared is $E_\gamma/2$ gives the final result:

$$f''(x) = \frac{E_\gamma}{2r_0^2} e^{\frac{-x}{r_0}} \tag{4.5}$$

[4] $f(x)$ is the inverse function of the data plotted in fig. 4.29, so the x and y-axis must be exchanged.

[5] This is a rough approximation, the photo electron is most likely to be emitted sideways and will never be emitted in the forward or backward direction, as shown in fig. 2.1.

In order to keep the model simple, diffusion is assumed to increase the parameter r_0. So no additional parameters are introduced, simply the interpretation of r_0 changes.
The function fitted to the data shown in fig. 4.29 is therefore

$$f^{-1}(y) = r_0\, ln(\frac{E_\gamma}{2}) - r_0\, ln(y). \tag{4.6}$$

Experimental Results

The fits of the function $f^{-1}(y)$ to the data are shown in fig. 4.33.

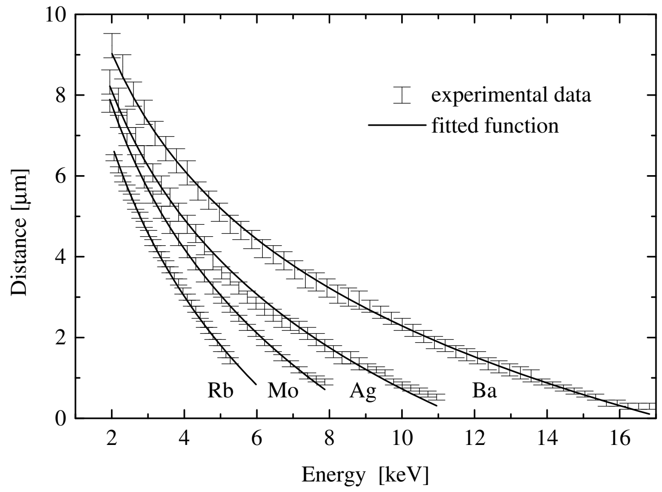

Figure 4.33: Plot of the experimental data with the fitted theoretical functions.

The fitted functions are considered to be an adequate representation of the experimental data. These were cut at 2 keV at the low energy end to reduce errors arising from noise and at about 0.5 of the photon energy. At these values multi clusters should not occur, however some double clusters are still observed due to random multiple hits within one acquisition. By cutting the data at 0.5 of the photon energy these errors are reduced.
The parameters obtained from the fit are E_γ and r_0. E_γ should correspond to the photon energy, r_0 is an effective range, and can not be compared directly to theoretical values, but is expected to be of the same order of magnitude as the range of the photo-electron. Both E_γ and r_0 are plotted in fig. 4.34 with the published values [Fir96], [Tab96].

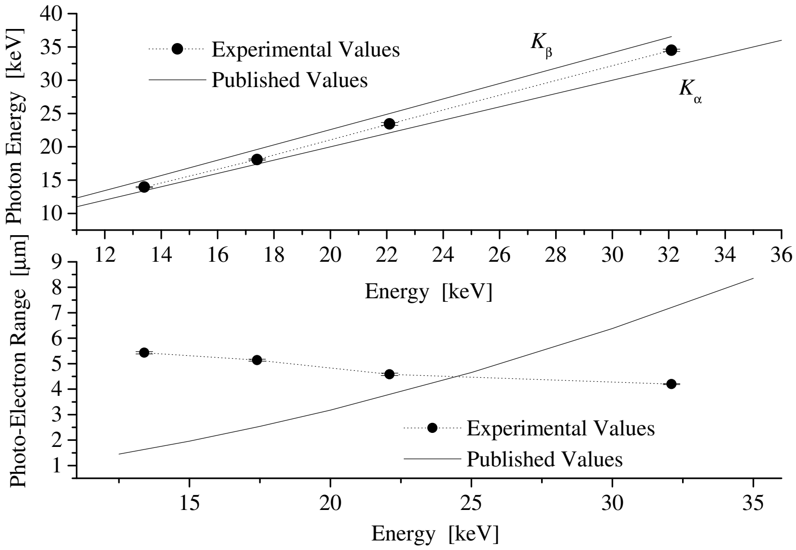

Figure 4.34: Plot of the parameters from the fitted functions. The photon energies are consistently too large (4-7 %). The values for r_0 are in the order of the published electron ranges.

Further conclusions are not drawn since the model is very simplistic and diffusion is the dominant effect. The values for the photon energy E_γ are consistently too high, (4 - 7 % higher than the K_α energies).
These values are used to plot the distributions of the charge clouds $f''(x)$, which are shown in fig. 4.35. The distributions are normalised to the photon energy, so at any point the higher energy sources have larger values although the relative widths are increased for the lower energy X-rays.

Comments
In principle the only requirement for the fitted function is to accurately represent the experimental data. However since these are terminated, the fitted function is used to extrapolate to energies of '0' and '$E_\gamma/2$'. The accuracy of the extrapolation to $E_\gamma/2$ is directly given by the photon energies extracted from the model. But no charge sharing (extrapolation to '0') is never reached in the model due to the exponential function, which depends an the parameter r_0. The energy deposition from the photo-electrons might be more realistically modelled by terminating the exponential at some point, however fluorescence has been neglected. This is because the fluorescence yield for the Si K-shell is only about 5 % [Fir96] and does not contribute significantly. It will however contribute to the long range, low

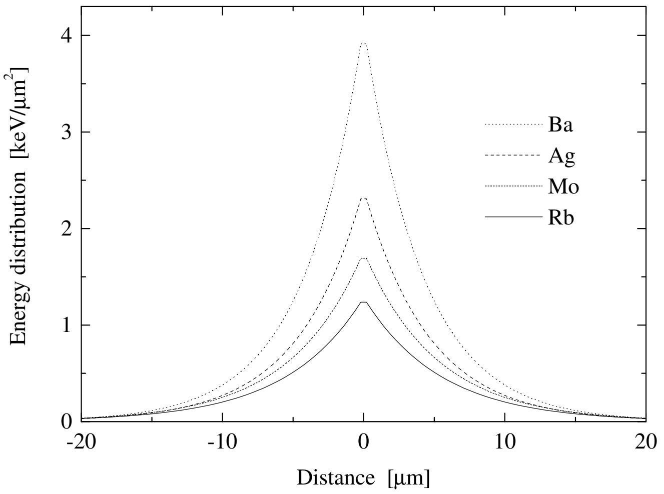

Figure 4.35: Signal distribution obtained from the fitted parameter values of E_γ and r_0.

energy charge sharing at some level and is known to have an exponential attenuation, however with an equivalent range of 14 μm [NIST].
Another source of errors for the given charge cloud density might arise from the differentiation. Although the fitted function may seem accurate, minor deviation can be significantly increased in the second derivative. By reducing the number of data points and therefore gaining larger differences in their values allows to differentiate the data directly. The model can then be fitted to the first derivative $f'(x)$. The results prove to be similar as far as the photon energies are concerned, the ranges are slightly smaller ($\approx 1\,\mu$m smaller).

Chapter 5

Characterisation of the LAD1

The aim of this chapter is to describe the investigation of the most important properties of the LAD1 system. This detector is designed for imaging applications, for which the spatial resolution, noise performance and rate capability are considered to be the most important aspects. The first section gives a brief description of the data acquisition. In the second part the line spread function and modulation transfer function are used to determine the spatial resolution. Section three describes the image noise in photon counting systems and discusses experimental results. The last section is concerned with the rate capability of the LAD1. All data discussed in this chapter were acquired with a single chip module and a 300 μm thick Si detector.

5.1 Data Acquisition

All data discussed in this chapter were taken at the Daresbury SRS [SRS]. An X-ray beam was reflected off a silicon crystal, giving a monochromatic beam with an energy of 19.5 keV. The detector was placed about two meters from the silicon crystal. Focusing in the horizontal was possible by bending the crystal. An image of the focussed beam is shown in fig. 5.1. The acquisition time was 20 ms and the maximum signal around 2700 counts.

The read out mode can be chosen to acquire 100 images under identical conditions but with a successively increased threshold. An example of such a threshold scan and its derivative are plotted in fig. 5.2. The derivative (correctly the negative derivative) is the energy spectrum. At a threshold value of around 20 the comparator threshold moves into the noise, leading to a massive increase in the number of registered counts. The read out uses a Schmitt-trigger, which leads to zero counts at low threshold due to continuous pile-up.

Imaging was possible by scanning the detector through the beam. The image of an IC-chip of about 5 mm length, placed in front of the detector, is shown in fig. 5.3.

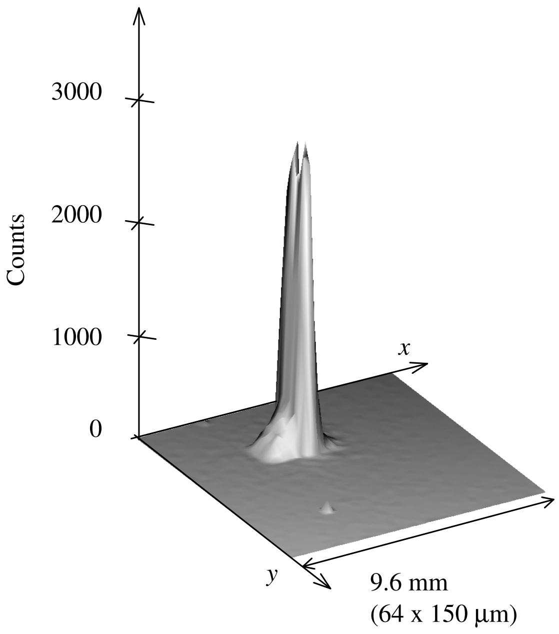

Figure 5.1
Image of a focussed beam taken at the Daresbury SRS in a 19.5 keV X-ray beam. A noisy pixel can be seen in the front part of the picture. The beam was focussed along the x-axis which leads to the tapered profile.

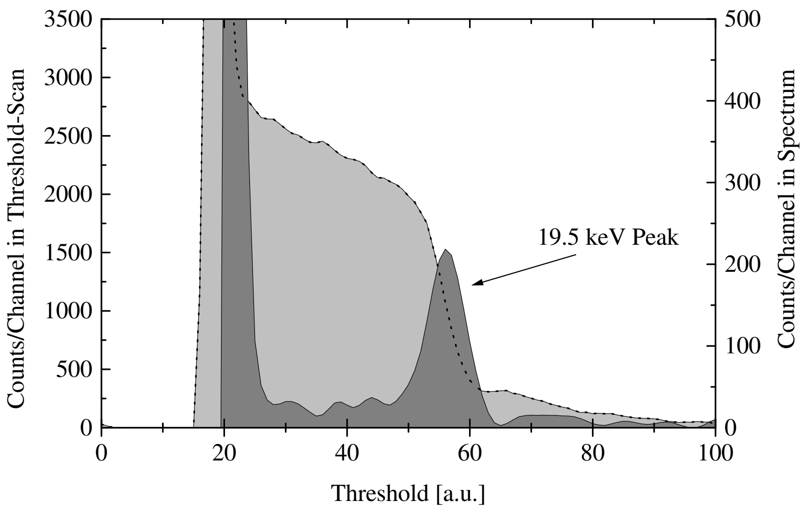

Figure 5.2: Example of a threshold scan plotted with its derivative, which is the energy spectrum. At a value of around 20 the threshold moves into the noise. The Schmitt trigger does not fire for low thresholds due to continuous pile-up. The high rate of the SRS leads to pile-up events of higher energy, seen above the 19.5 keV peak.

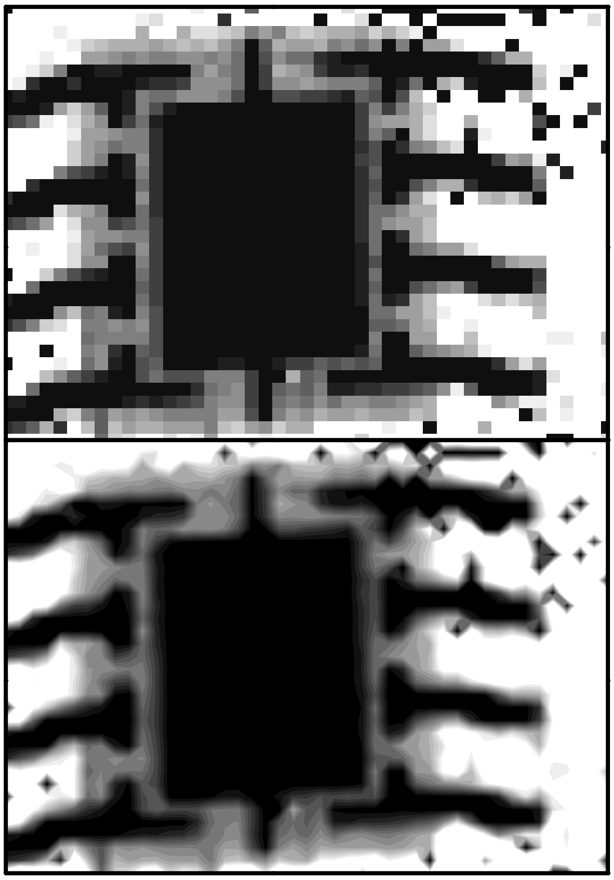

Figure 5.3
Image of an IC-chip taken by scanning the detector and object through the beam. The image covers an area of 45 by 34 pixels; the upper shows the grainy pixel structure, the lower is a contour plot which interpolates between pixels.

5.2 The Spatial Resolution

In this section the **L**ine **S**pread **F**unction (LSF) and **M**odular **T**ransfer **F**unction (MTF) will be introduced as a method to determine the spatial resolution of an imaging system.
Some theoretical background is considered in order to apply the MTF specifically to pixel detectors. Theoretical derivations of the LSF and MTF are made and compared to the experimental results.

5.2.1 Definition of the MTF

The MTF is a common tool to evaluate the spatial resolution of a radiographic imaging device [IC86]. To enable a comparison of different devices a standard way

of measuring the spatial resolution is necessary. The MTF is such a method. Equivalent to imaging objects is the response to exposure to varying intensities, and the latter is what is used for the MTF. By definition (for the MTF) the intensity per unit length varies sinusoidally with distance. So the perfect image would be a strip pattern with dark and light lines, the transition corresponding to a sine wave. One period of such a pattern is referred to as a line pair (lp). So the unit for the spatial resolution (spatial frequency) is lp/mm: the more lp/mm resolved, the better the spatial resolution of the device.
Ideally the response of the system would be equal to the input (sine wave), however as deteriorating effects are present in all systems, blurring will occur. For increasing spatial frequencies the response will become less distinct, the line pairs fade and the response converges to the average intensity, as illustrated in fig. 5.4.

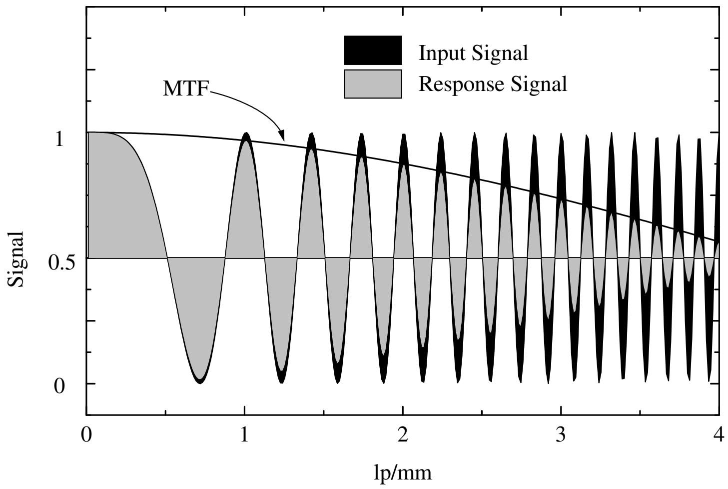

Figure 5.4: The plot shows the input spatial frequency and the corresponding response. The MTF is defined as the relative response (response/input).

The area under the response signal is equal to that of the input signal, which is physically reasonable as the input signal is merely distributed but not lost. The MTF is defined as the proportion of the response signal to the input signal ($\frac{\text{response signal}}{\text{input signal}}$). In fig. 5.4 the input signal is normalised, so the MTF has values between 1 and 0.5. To give the MTF the meaning of how well a spatial frequency is resolved it is commonly normalised to have values between 0 and 1.
Some practical problems may be faced when trying to measure a MTF in the way described above. Although it may be possible to get a sine wave intensity with different spatial frequency for visible light and longer wavelengths it is impossible

for X-rays, which are of interest for the systems discussed here.
For such systems it is convenient to calculate the MTF from the LSF.

5.2.2 Calculation of the MTF from the LSF

The mathematical reason for the deteriorating effects is that the intensity at a point x_0 is distributed around x_0. In the above discussion (fig. 5.4) it was assumed that this distribution is symmetric, hence the symmetry of the sine waves was conserved. This assumption is true for the X-ray detectors considered.
There can be various physical reasons for the distribution of the signal. In most state-of-the-art pixellated detectors the pixel size is certainly the dominant factor[1]. Any X-ray absorbed at a point on the detector will give a signal with a distribution of at least the size of the pixel it hit. Additionally, charge sharing contributes to the spreading of the signal. So instead of the ideal delta distribution, real systems respond with some distribution of finite width. The illustration of the effect this has on the input signal is shown in fig. 5.5. If all signal received at a point were

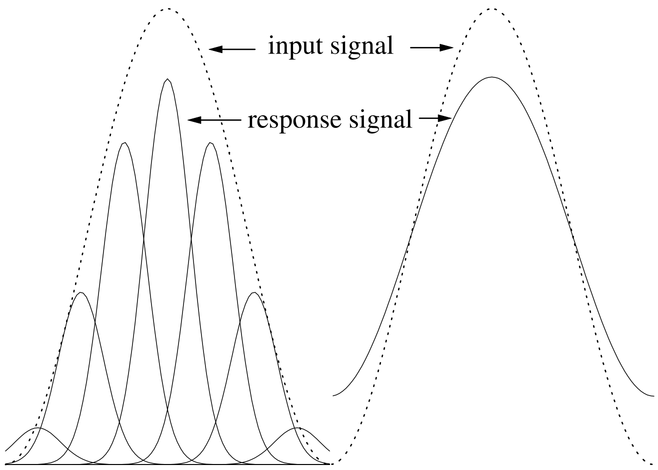

Figure 5.5: The dotted line corresponds to the sine wave input signal. On the left hand side the response at some points is shown for a real system, at each point a distribution is convoluted with the input signal. The result is the response signal shown on the right.

seen at that point (δ response) the input signal would be returned perfectly. As

[1] An infinitely narrow X-ray beam will generate a signal across an area of several microns diameter [Mat01]. The pixel size of existing integrating detectors still exceeds these dimensions significantly ($\sim$25μm).

in fig. 5.5 the response has a finite width the considered point will have less signal as part is lost to the surroundings.
The area under the δ distribution and the distribution of the real system are the same (normalised to 1). The expression of this in mathematical terms is the following:
For any spatial frequency z the delta distribution returns the input signal unchanged. In the case of a sine input with spatial frequency z, the input function is $sin(2\pi xz)$, where x is the spatial distance. So at any point x_0 the response $r_\delta(x_0, z)$ is

$$r_\delta(x_0, z) = \int \delta(x_0 - x) sin(2\pi xz) dx = sin(2\pi x_0 z) \tag{5.1}$$

The right hand side is simply the input signal at x_0.
For the real system the delta function is replaced with the response distribution $f(x)$. However the point x_0 has contributions not only from $f(x_0)sin(2\pi x_0 z)$ but also from $f(2x_0 - x)sin(2\pi xz)$, this is simply taking the spread of the input signal into account as shown in fig. 5.6. The equation giving the response of the real

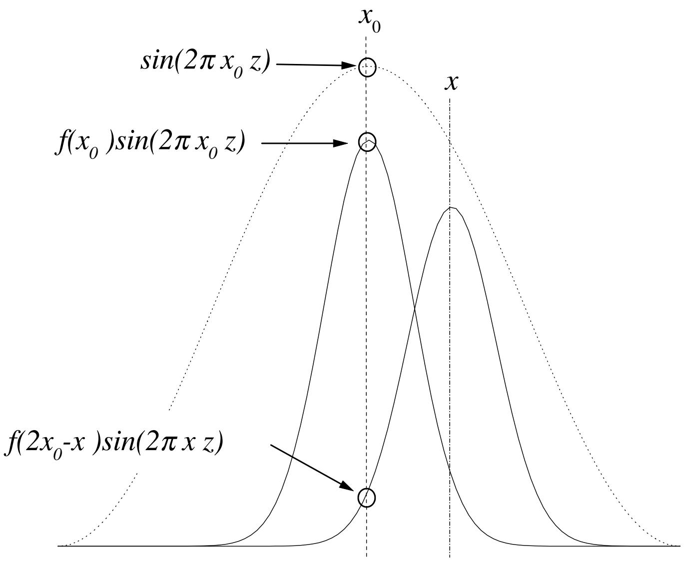

Figure 5.6: Illustration of the contributions to the signal at a point x_0 in a real system.

system is therefore

$$r_f(x_0, z) = \int f(2x_0 - x) sin(2\pi xz) dx \tag{5.2}$$

The MTF can be extracted at any point of the period (since it is defined as the fraction of response signal to the input signal), choosing the maximum at each spatial frequency retains the normalisation. In the above discussion it was assumed, that $f(x)$ has its maximum at the same point as the input function. To simplify matters it is reasonable to assume that $\max[f(x)]=f(0)$, the point where the X-rays hit the detector is then $x = 0$ and $f(x) = f(-x)$. However if the input is a sine wave its maximum would be at $x = 0.5$, so either a phase shift must be introduced, or the cosine used instead. This simplifies the calculation of the response signal, which can now be written as

$$r_f(z) = \int f(x)cos(2\pi xz)dx \tag{5.3}$$

This is the response at $x = 0$, dividing this by the input signal will give the MTF dependence on the spatial frequency z. As $cos(0) = 1$ the above equation is equal to the MTF and assuming that $\int f(x)dx = 1$, the MTF will be normalised.
To acquire the MTF of a system it is sufficient to know the response to an infinitely narrow input, which is $f(x)$. The MTF can then be calculated for any spatial frequency z according to the formula:

$$\mathrm{MTF}(z) = \int f(x)cos(2\pi xz)dx \tag{5.4}$$

This is however simply the Fourier transform of $f(x)$ in spatial frequency. The important symmetry, $f(x) = f(-x)$, reduces the Fourier transform to the cosine transform [Bro79].
So far the problem of measuring the MTF has reduced to acquiring the distribution $f(x)$. This can be achieved by taking an image of a narrow slit, narrow in this case meaning several times smaller than the pixel size in order to get a good approximation to an infinitely narrow slit. Cutting the image of the slit perpendicular to the slit will give the distribution $f(x)$, which is referred to as the line spread function (LSF).
A consequence of the equivalence between the MTF and the Fourier transform of the LSF is that this allows two ways of obtaining the MTF.

1. Measurement of the LSF.

2a. Calculation of the MTF according to[2]:

$$\mathrm{MTF}(z) = \int \mathrm{LSF}(x)cos(2\pi xz)dx$$

2b. Fitting of a function to the LSF data which gives an accurate description of the LSF and Fourier transforming the fitted function in spatial frequency.

Depending on the LSF data one or other of the methods might be preferable.

[2]A direct Fourier transform assumes a period of 2π which in this case is not appropriate. Therefore a factor of 2π must be introduced in the argument of the trigonometric functions.

5.2.3 Error Considerations for the MTF

The errors in the MTF depend on the accuracy of the LSF data. Considering the first method of calculating the MTF directly from the LSF data, the following errors should be taken into account:

1. The measured LSF will be evaluated as having a certain width, which excludes the tails of the LSF beyond a certain level - the LSF is truncated. Therefore part of the area under the LSF is not taken into account and the error in the MTF is proportional to the excluded area fraction [Doi72]. This is referred to as the "truncation error". It can be controlled by extending the LSF width until the effect can be neglected.

2. The sampling distance step of the LSF is finite, this leads to what is referred to as the "aliasing error" [IC86]. Theoretical and experimental studies indicate that the sampling distance step should be less than about 0.25 of the half width at half maximum of the LSF, if errors in the computed MTFs are to be less than 0.005 [IC86].

In principle both of these errors can be controlled by choosing the right experimental setup. In the case of the aliasing error it might be necessary to scan the line across the imaging device.
Both these errors are eliminated when fitting a function to the LSF and Fourier transforming that function. The quality of the MTF then depends only on how well the fitted function represents the LSF. The choice of function does not have to be justified by any theoretical expectation of what the LSF should look like, the only important point is that the measured LSF should be as closely as possible represented by the fit.

5.2.4 Calculation of the Theoretical MTF

For non circular pixels the LSF will depend on the angle at which the slit is placed across the detector. The x-axis of the LSF is given by the distance to the centre of the pixel. The amplitude or y-axis is proportional to the length of the slit within the pixel boundary. For square pixels this is shown in fig. 5.7. Before looking at different pixel sizes, the influence of the angle at which the slit is placed across the detector will be discussed. The theoretical LSFs and MTFs of a pixel detector with 150 μm square pixels are shown for different alignments of the slit in fig. 5.8 and fig. 5.9. Taking the row number as x-axis and the column number as y-axis, the orientation of the slit is given by $y = mx + d$, where m is the slope of the slit, d the offset in pixels and $0 \leq m \leq 1$ will take all possible orientations into account, due to the symmetry of the detector. The calculated LSFs for some values of m are shown in fig. 5.8. Due to the symmetry of the LSF it is sufficient to consider the positive part only. Accordingly only the positive halves of the LSFs are shown in fig. 5.8. The corresponding MTFs, shown in fig. 5.9, were calculated according

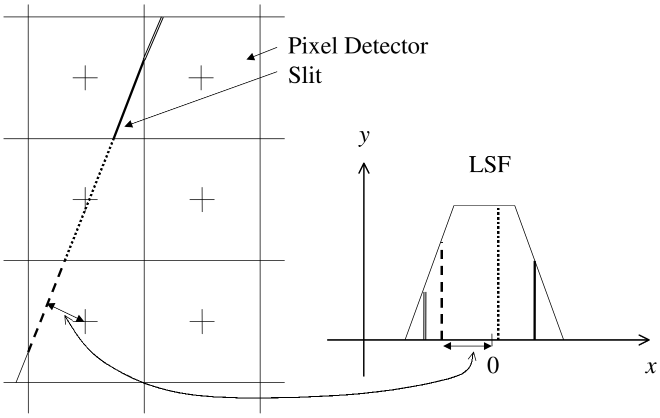

Figure 5.7: The figure shows the method used for calculating the LSF in the case of square pixels.

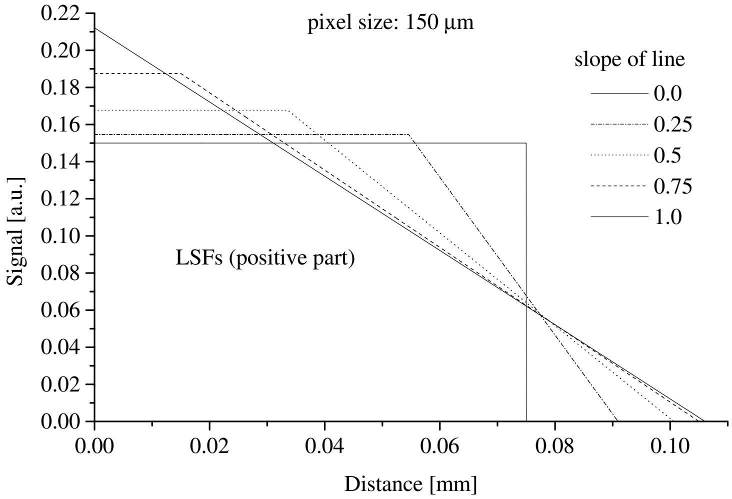

Figure 5.8: Theoretically calculated LSFs for different orientations of the slit.

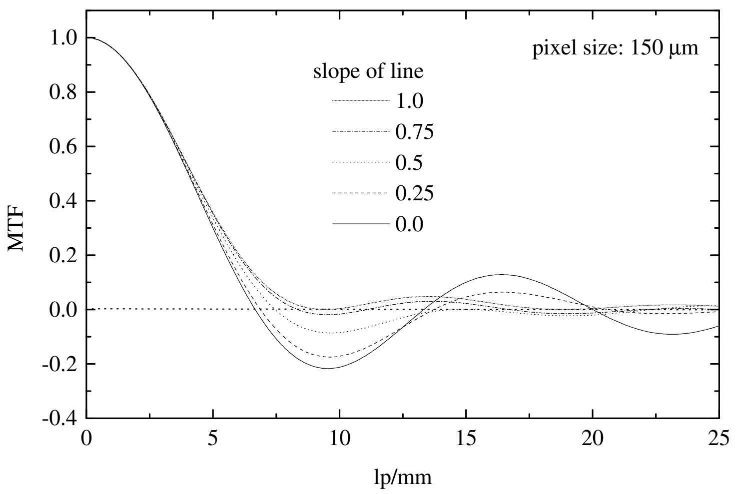

Figure 5.9: Corresponding MTFs to the LSFs shown above.

to the formula:

$$\mathrm{MTF}(z) = \int_0^{\infty} \mathrm{LSF}(x) cos(2\pi xz) dx \tag{5.5}$$

where z is the spatial frequency in lp/mm. A value of '0' in the MTF corresponds to the average intensity, values between '0' and '-1' correspond to intensities between the mean and zero and are physically reasonable.

The oscillations seen in fig. 5.9 are due to the LSF extending into the next period of the cosine (neighbouring line pair), which gives rise to interference patterns with the actual signal in that line pair. So the oscillations are caused by integrating over more than one line pair (one period in the cosine) and can be eliminated by simply reducing the integral boundary to $\frac{1}{2z}$ instead of ∞:

$$\mathrm{MTF}(z) = \int_0^{\frac{1}{2z}} \mathrm{LSF}(x) cos(2\pi xz) dx \tag{5.6}$$

Calculating the MTFs from the same LSFs as before (fig. 5.8) leads to the curves shown in fig. 5.10. The MTFs in fig. 5.10 correspond to a single period instead of an infinite number of line pairs.

The MTF has a noticeable dependence on the orientation of the slit. When evaluating the number of line pairs per mm a system can resolve, this number conventionally corresponds to an MTF of 0.3. At this MTF value (as shown in fig. 5.9 and fig. 5.10), the variation with the orientation of the slit is below 5 % of the mean value. For the further discussion the spatial resolution is defined as the number of lp/mm at an MTF value of 0.3. With this definition a comparison of different

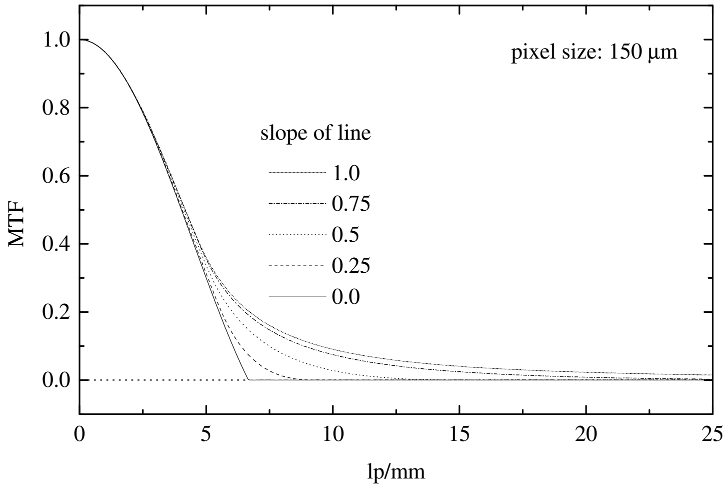

Figure 5.10: MTFs calculated by integrating over one period only. This eliminates the interference and therefore the oscillations.

pixel sizes and geometries can be performed. For square pixels and a slope of 0.5 the resolution as a function of the pixel size is plotted in fig. 5.11. For any given slope the spatial resolution at an MTF value of 0.3 is given by

$$\text{spatial resolution [lp/mm]} \quad = \quad \frac{k(\text{slope})}{\text{pixel size [mm]}} \tag{5.7}$$

where k(slope) is a constant, dependent only on the slope of the line and from the pixel symmetry it is sufficient to consider values of slope between '0' and '1'. k(slope) is plotted in fig. 5.12, the two curves representing the different limits of integration. In order to obtain a simple formula for calculating the spatial resolution of any pixel size at a given slope, an analytical expression for k(slope) is convenient. The curves in fig. 5.12 are well described by a function of the form

$$f(\text{slope}) = a\, e^{-b\left((\ln|\text{slope}|)^2\right)^c} + d \tag{5.8}$$

which has the desired symmetry properties. The choice of function is arbitrary, the only requirement is that it must be a good representation of k(slope). The fit to the data for infinite integration boundaries is shown in fig. 5.13. The maximum deviation of k(slope) from the calculated data points is 0.1%, (0.2% in the case of integrating over one period). The values of a, b, c and d are given in table 5.1. The numbers of digits quoted are chosen to have the same significance on the result while keeping the accuracy given by the fit of k(slope). Finally a theoretical limit

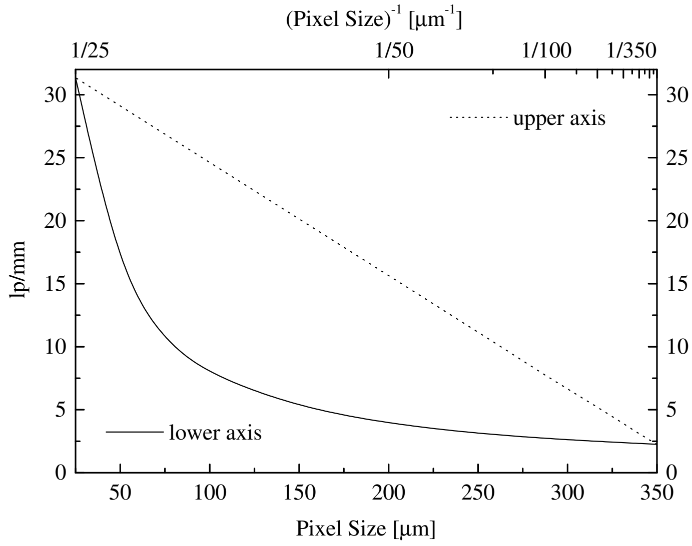

Figure 5.11: The maximum theoretically achievable resolution, for a slope of 0.5, is plotted against the size of a square pixel. The resolution is inversely proportional to the pixel size, shown in the dotted line.

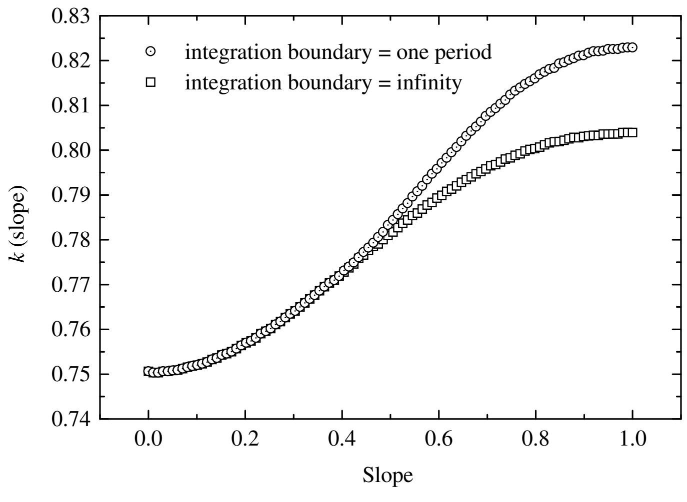

Figure 5.12: k(slope) is plotted for values between '0' and '1' for integration boundaries of one period and infinity.

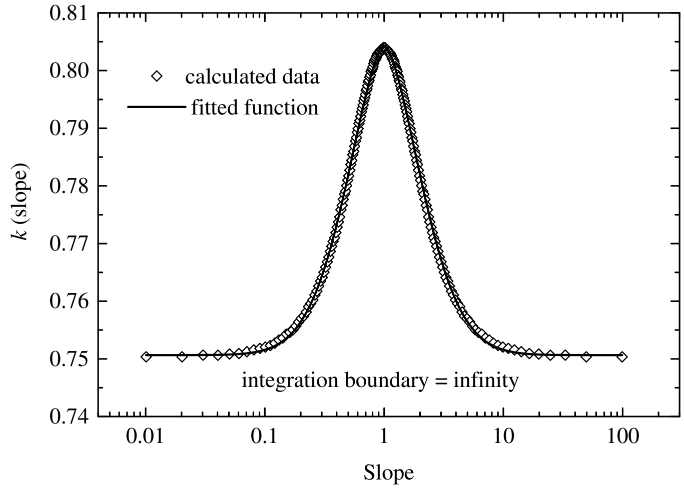

Figure 5.13: Calculated data points and fitted k(slope) function. The x-axis is logarithmic to show a wider range of slope values.

integration boundary	a	b	c	d
infinity	0.0532	1.037	0.852	0.7512
one period	0.0725	1.397	0.787	0.7519

Table 5.1: Values of the parameters determined for k(slope).

for the spatial resolution as a function of the pixel size and slope of the line can be calculated from

$$\text{Spatial-Res.}_{\infty}[\text{lp/mm}] = \frac{0.0532\, e^{-\left(1.037\,(\ln|\text{slope}|)^2\right)^{0.852}} + 0.7512}{\text{pixel size [mm]}} \tag{5.9}$$

$$\text{Spatial-Res.}_{\text{one p}}[\text{lp/mm}] = \frac{0.0725\, e^{-\left(1.397\,(\ln|\text{slope}|)^2\right)^{0.787}} + 0.7519}{\text{pixel size [mm]}} \tag{5.10}$$

for integration boundaries of infinity and one period respectively. The inaccuracy of the fit dominates the errors, the formulae agreeing with calculated values to <0.2%.

Pixel Geometry

Although so far only the square pixel geometry has been considered, in principle any geometry can be used. The next most common is the hexagonal or honeycomb structure. To draw a comparison between the theoretically achievable spatial resolution of different geometries, it is assumed that the areas of the pixels are the same. Instead of an hexagonal structure an evaluation was made of a circular structure as this has the highest symmetry and no slope dependence. The MTF of a circular and square pixel are shown in fig. 5.14. For the latter, the slope of the

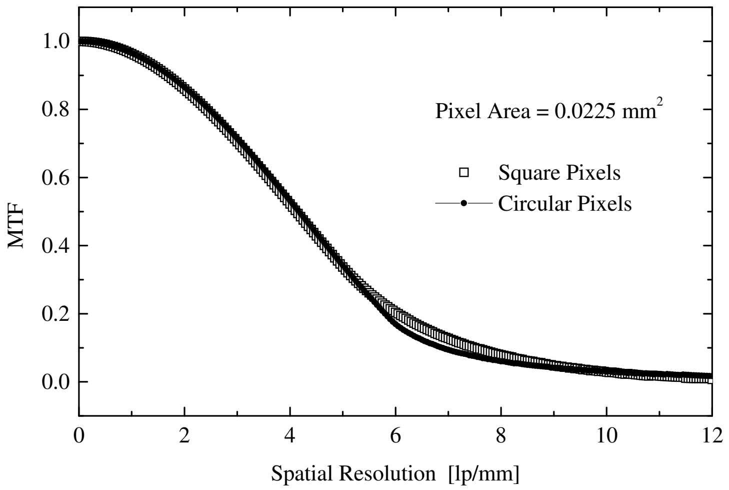

Figure 5.14: MTF of a circular and square pixel geometry with the same area. There is no significant difference.

line is 0.5. The dependence of the square pixel MTFs on the slope is far greater than the difference seen between the MTFs in fig. 5.14. It is concluded that there will be no significant difference in the spatial resolution between a square and hexagonal pixel geometry.

CTF and PSF

The **C**ontrast **T**ransfer **F**unction (CTF) is an analogous measure to the MTF.The only difference is a square wave input signal instead of a sine wave [Fro98]. This allows differently spaced bar patterns to be used to image the CTF directly.
The **P**oint **S**pread **F**unction (PSF) is consistently defined as the response of the system to a point input. The cross-section of the PSF should be identical to the LSF. For pixel detectors it is not practical to use the PSF because the number of data points is not competitive with what is more easily achieved with the LSF.

The Nyquist Frequency

A relevant measure is the Nyquist frequency, defined by

$$z_{\text{Nyquist}} = \frac{1}{2\Delta x}$$

where Δx is the sampling distance (related to the aliasing error). The Nyquist frequency is therefore the spatial frequency at which the LSF has 2 data points per line pair. The MTF (or CTF) ceases to have any physical meaning beyond the Nyquist frequency.

The behaviour of the MTF at the Nyquist frequency is shown in fig. 5.15. For

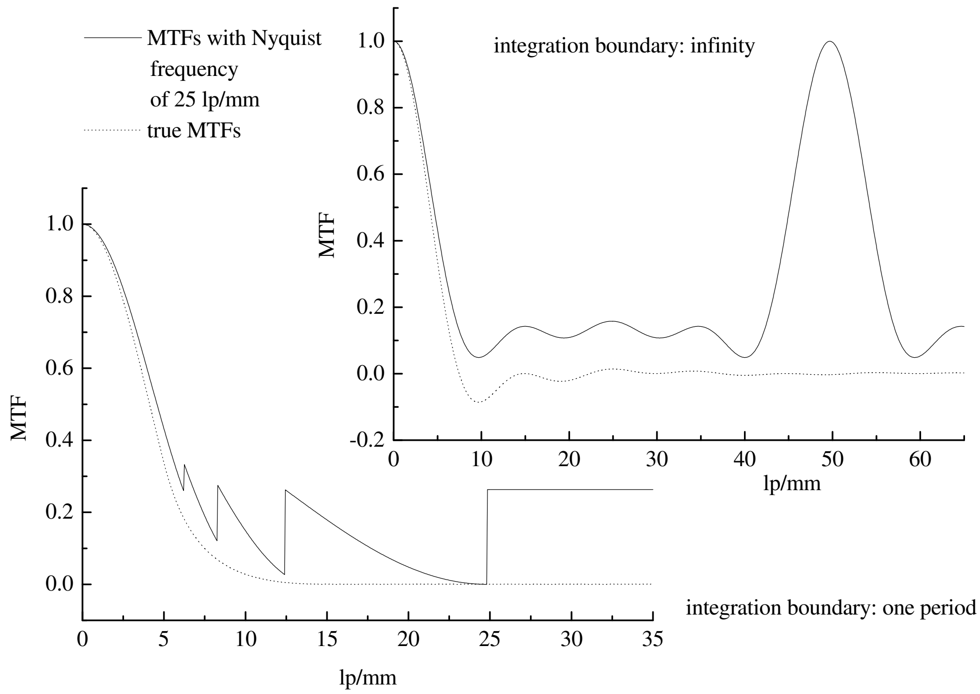

Figure 5.15: The graphs illustrate the limitation to the meaning of the MTF imposed by the Nyquist frequency. The upper and lower plot were calculated with integration boundaries of infinity and one period respectively.

measurements with pixel detectors the sampling distance is not constant and therefore the Nyquist frequency is not well defined. In practice this does not prove to be a problem since the maximum sampling distance can be kept small enough to obtain an accurate MTF in the region of interest. For increasing pixel sizes it may prove to be necessary to move the slit across the detector parallel to itself in order to get another set of data, thus reducing the sampling distance, thereby improving the aliasing error.

5.2.5 Measurement of the LSF and Experimental MTF

Images of a slit were taken in a 19.5 keV X-ray beam at the Daresbury SRS. A direct measurement of the slit width was not feasible[3]. An estimate is possible by comparing the measured number of counts with and without the slit in the beam. Without the slit the number of counts was approximately 5 times higher than with the slit, therefore the slit leaves about a fifth of the pixel area exposed, i.e. the width of the slit is about a fifth of the pixel size or 30 μm.
An image of the slit is shown in fig. 5.16, and the LSF extracted from these data is shown in fig. 5.17. The LSF extracted from the data in fig. 5.16 is shown in

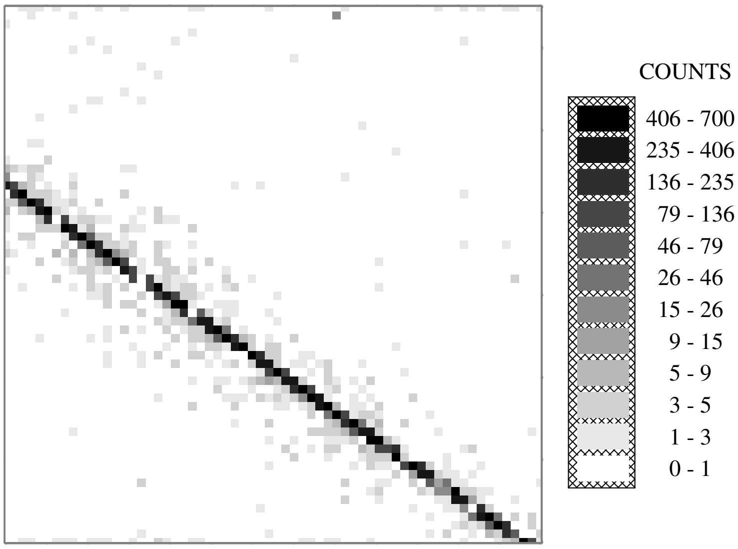

Figure 5.16: Image of a slit used for the calculation of the MTF. The gray scale corresponds to the log(counts) to make the low counts in pixels visible. The data was acquired with a threshold value of 35.

fig. 5.17 together with the fitted function.
The MTFs calculated from the LSF are plotted with the theoretical MTFs in fig. 5.18 and fig. 5.19 for integration boundaries of infinity and one period, respectively. From fig. 5.18 and 5.19 it is seen that the LAD1 has a spatial resolution of about 5.2 lp/mm. In fig. 5.19 the influence of the Nyquist frequency can be ob-

[3] This would have required to remove the slit, which was first aligned and then narrowed to the estimated width.

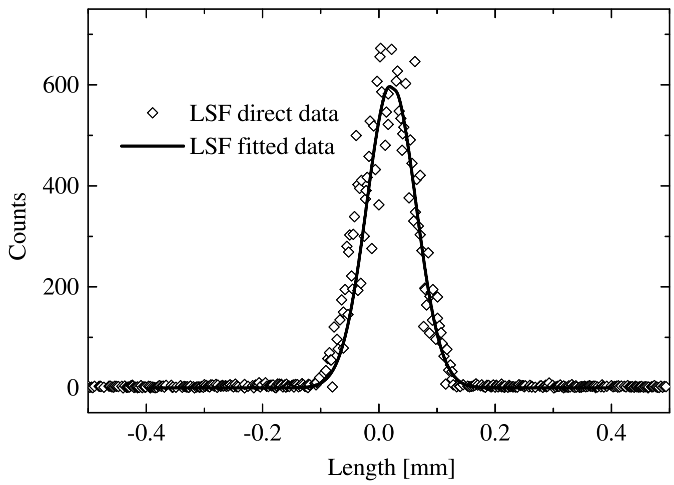

Figure 5.17: Experimental LSF with the fitted function.

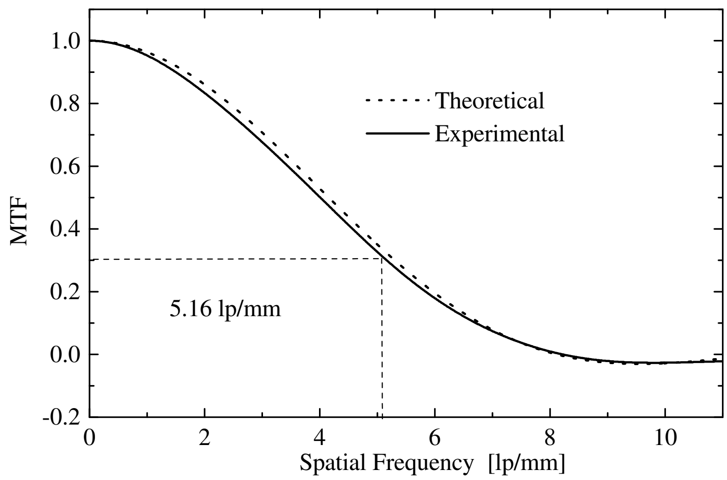

Figure 5.18: Experimental and theoretical MTFs for integration boundaries of infinity.

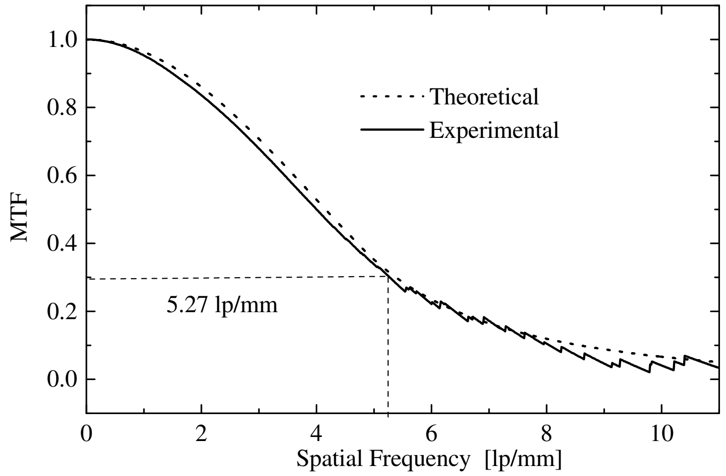

Figure 5.19: Experimental and theoretical MTFs for integration boundaries of one period.

served for spatial frequencies above about 5.5 lp/mm. The experimental MTFs are slightly lower than the theoretical curves, the spatial resolution is calculated to be 5.30 lp/mm (experiment: 5.16 lp/mm) and 5.37 lp/mm (experiment: 5.27 lp/mm) for integration boundaries of infinity and one period, respectively. Effects which could lead to a broadening of the LSF are charge sharing and the finite width of the slit.

Error Considerations for the MTFs

Figure 5.20 shows a plot of the spatial resolution as a function of the considered LSF width. The truncation error affects the result for LSF widths below about 200 μm. For the above MTFs the LSF was truncated around 400 μm.
The truncation error is negligible and can easily be reduced by extending the considered LSF width.
The aliasing error depends on the sampling distance of the LSF. This is not constant for the pre-sampling LSF. For the LSF in fig. 5.17 the mean sampling distance is 3.2 μm with a standard deviation of 1.5 μm. The corresponding Nyquist frequency is (156 ± 73) lp/mm. Figure 5.21 shows the experimental MTF from fig. 5.19 and a theoretical MTF with a Nyquist frequency of 156 lp/mm. The integration boundaries were chosen at one period, which makes the effect of the Nyquist frequency directly visible.

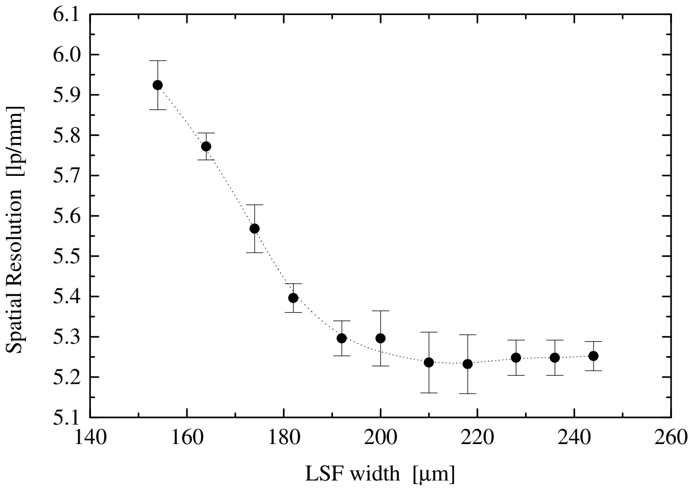

Figure 5.20: Plot of the spatial resolution as a function of the considered LSF width. The truncation error affects the results for a LSF width below about 200 μm.

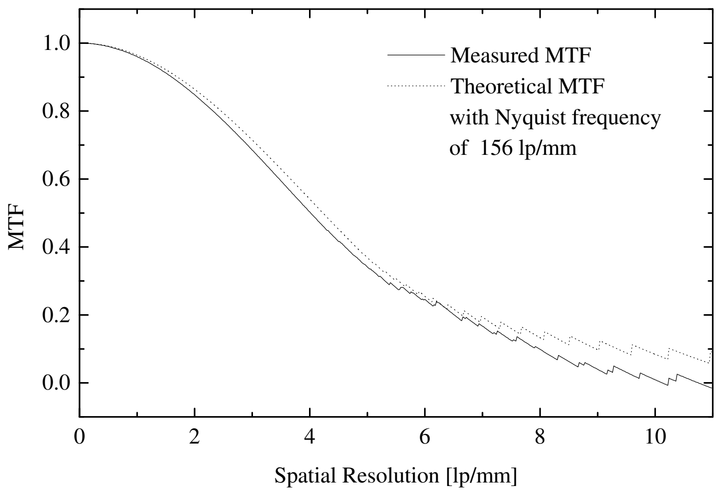

Figure 5.21: The graph shows the experimental MTF from fig. 5.19 and a theoretical MTF with a Nyquist frequency of 156 lp/mm.

To quantify the aliasing error the difference of the theoretical, true MTF and the theoretical MTF with a Nyquist frequency of 156 lp/mm, are plotted in fig. 5.22. The aliasing error increases the measured spatial resolution by 3 % at an MTF

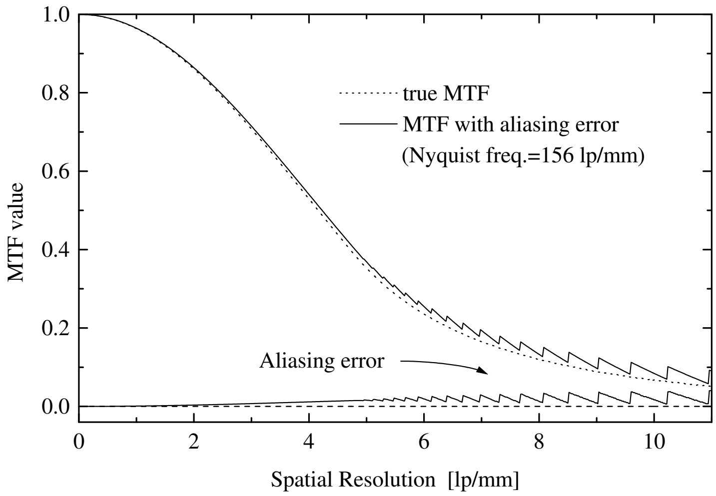

Figure 5.22: Theoretical MTFs showing the difference between the true MTF and the MTF with a Nyquist frequency of 156 lp/mm. At an MTF value of 0.3 the aliasing error increases the resolution be 3 %.

value of 0.3. Subtracting this error from the above stated spatial resolution of the LAD1, gives a final result of 5.1 lp/mm.
An estimation of the error of this value is gained by measuring the LSF and MTF at different threshold values set for the data acquisition. The spatial resolution as a function of the threshold is plotted in fig. 5.23. The range of threshold values (30-48) is selected to be above the noise but below the photon peak, see fig. 5.2. The mean value and standard deviation are used to give the final result for the spatial resolution of 5.1 ± 0.1 lp/mm.

The Fitting Method

The function used for fitting the data shown in fig. 5.17 is

$$f(x) = a_2\, e^{-\frac{1}{2}\left(\frac{a_1 - x}{a_3}\right)^2} + a_4\, e^{-\frac{|x-a_1|}{a_5}}. \tag{5.11}$$

The Fourier transform in spatial frequency is [Yin90]:

$$\mathrm{MTF}(y) = \frac{\sqrt{2\pi} a_2 a_3\, e^{-2(\pi a_3 y)^2} + \frac{2 a_4 a_5}{1+4(\pi a_5 y)^2}}{\sqrt{2\pi} a_2 a_3 + 2 a_4 a_5} \tag{5.12}$$

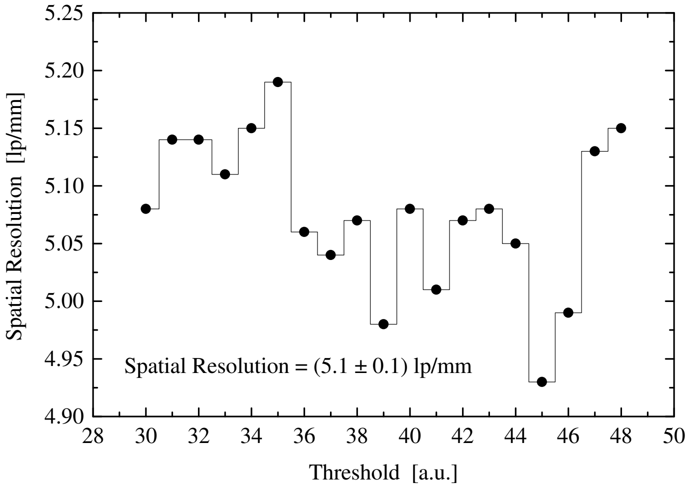

Figure 5.23: Plot of the spatial resolution as a function of the threshold.

The MTF given by equation 5.12 can be compared to the MTF calculated directly from the data according to equation 5.5. Figure 5.24 shows the MTFs derived from the fit using equation 5.12, the directly transformed data[4] and the theoretically calculated data.

The Fourier transform of the fitted function is significantly larger than the direct and theoretical MTF. The fit may be too narrow on the left hand side of fig. 5.17. The fitting method is assumed to be erroneous in this case. The reason for the poor agreement may also be due to the high fluctuations in the LSF data. These are significantly higher than would be expected from pure statistics. This is due to the variation of the pixel offsets and gains. The 3 bit threshold adjust is not sufficiently expandable to compensate for the variations occurring. Consequently different pixels are not directly comparable. A section of the line crossing the pixels and the measured threshold scans are shown in fig. 5.25, illustrating the variation in the pixel performances.

5.2.6 Résumé

The LSF and MTF have been used to define the spatial resolution. For square pixels an analytical formula has been derived allowing the calculation of a theoretical LSF and MTF.

[4]The directly transformed data is evaluated for an infinite number of periods, since this is equivalent to the Fourier transform given by equation 5.12.

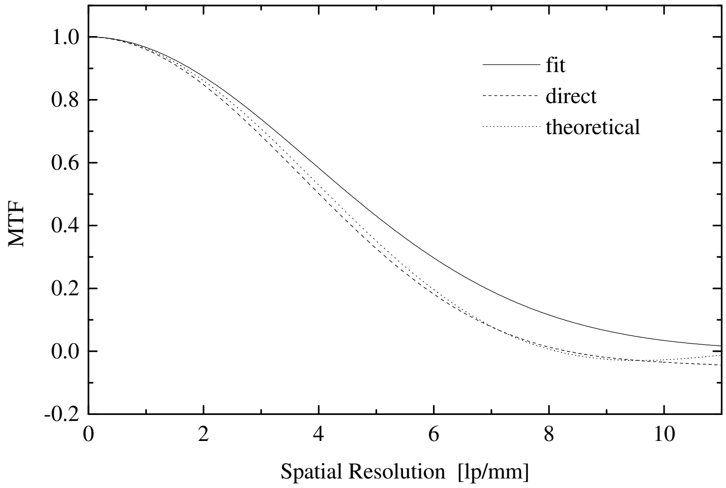

Figure 5.24: Comparison of the MTFs derived from the fit, the direct transform and the theoretical data.

A calculation of the MTF for a "circular" geometry shows no significant difference from square pixels. This leads to the conclusion that a hexagonal and square pixel geometry of equal pixel area will have virtually the same spatial resolution.
The resolution of the LAD1 was experimentally measured to be (5.1 ± 0.1) lp/mm; the theoretical prediction is 5.3 lp/mm.

5.3 Image Noise

5.3.1 Events in Photon Counting Systems

For a photon counting system this noise is due to a difference in the number of counts. The following occurrences influence the event registration and should therefore be considered with respect to their noise contribution:

1. The source will have a statistical variation in the number of particles emitted per exposure time (Poisson noise).

2. Not all particles hitting the detector will be absorbed.

3. The threshold of the read out discriminates events according to their signal height.

4. Noise events may exceed the threshold value and lead to false counts.

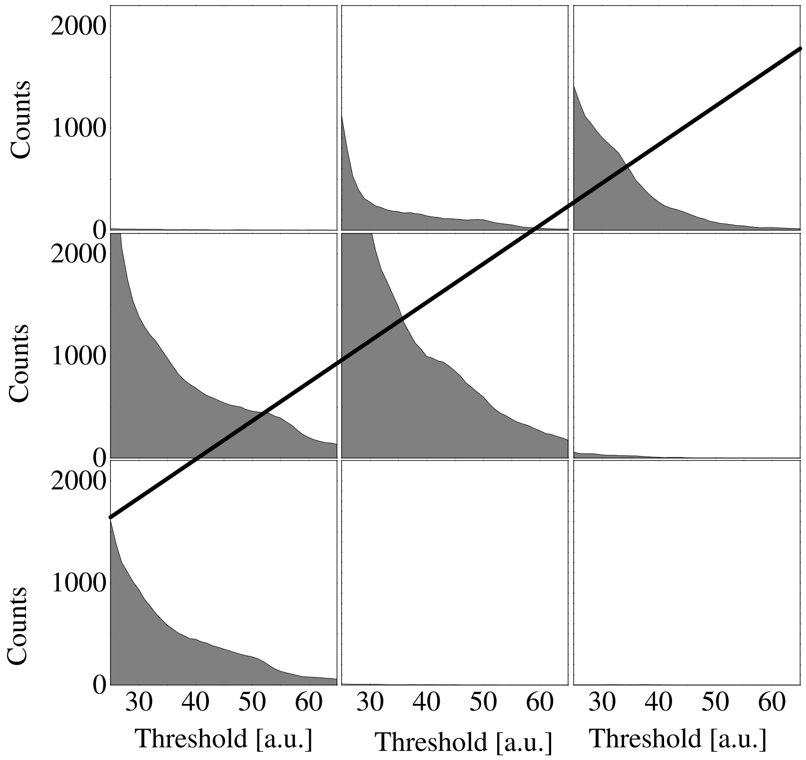

Figure 5.25: Plot of the line crossing nine pixels with each pixel showing its threshold scan. This illustrates the variation in the pixel performances, the pixel in the upper right corner should have the highest count rate but shows less than the centre pixel, which is due to a different offset and/or gain.

5. The rate dependent dead time leads to a reduction in the number of events registered.

These points will be addressed in the order mentioned.

Poisson Statistics

The emission of particles from a source obeys Poisson statistics:

$$p(k, \lambda) = \frac{\lambda^k}{k!}\, e^{-\lambda} \tag{5.13}$$

where $\lambda \in \mathbf{R}^+$ is the parameter of the Poisson distribution and $k \in \mathbf{N}_0^+$ the variable. So for a source with parameter λ the probability of k emissions is $p(k, \lambda)$.

The expectation value of k is

$$< k >= \sum_{k=0}^{\infty} k\, p(k,\lambda) = \sum_{k=0}^{\infty} k\, \frac{\lambda^k}{k!}\, e^{-\lambda} = \lambda\, e^{-\lambda} \sum_{k=1}^{\infty} \frac{\lambda^{k-1}}{(k-1)!} = \lambda. \tag{5.14}$$

A similar calculation as above yields:

$$< k^2 >= \lambda^2 + \lambda \tag{5.15}$$

and therefore the variance is

$$\mathrm{var}(k) =< (< k > -k)^2 >= \lambda. \tag{5.16}$$

So the standard deviation $\sigma = \sqrt{\lambda}$ and consequently the error on a number of counts is equal to the square root of the number of counts. This is referred to as Poisson noise and is a lower theoretical limit to the noise achievable with any detector.

Several Sources

Two sources a and b, with individual means λ_a and λ_b allow the calculation of the probability of observing k_a and k_b events. For a photon counting system it may be assumed that only the sum of the events $k_a + k_b = k$ will be registered and events from source a or b can not be distinguished. The total number of k events could be all of source b, or one of source a and the rest of source b, and so on. The total probability is given by [Bar89]

$$p(k) = \sum_{k_a=0}^{k} p(k_a,\lambda_a)p(k-k_a,\lambda_b) = \frac{(\lambda_a+\lambda_b)^k}{k!}\, e^{-(\lambda_a+\lambda_b)} \tag{5.17}$$

so the sum of two Poisson processes is another Poisson process. This can be extended to any number of Poisson processes.
Therefore any X-rays arriving at the detector will be Poisson distributed.

Absorption Properties of the Detector

As the absorption of X-rays obeys an exponential attenuation law with absorber thickness not all photons are detected. For a given detector the fraction of absorbed X-rays is only dependent on their energy. So if p_{E} is the energy dependent probability of absorbing a X-ray with energy E ($p_{\mathrm{E}} < 1$), then the mean number of absorbed X-rays is $\lambda_{\mathrm{E,abs}} = p \cdot \lambda_{\mathrm{E}}$ if λ_{E} is the mean number of X-rays impinging on the detector. What needs to be proven, is that the probabilities are still given by a Poisson distribution. This follows from the fact that the Poisson distribution is the limit of the binomial distribution for $n \to \infty$, where n is the number of trials. With n trials and an average of $\lambda_{\mathrm{E,abs}}$ events, the probability of getting an event

in a trial is $p = \lambda_{\mathrm{E,abs}}/n$, n is assumed so large that the probability of more than one event in a trial can be discounted.
The probability p_{b} of observing k events in the n trials is given by the binomial formula

$$p_{\mathrm{b}}(k; \lambda_{\mathrm{E,abs}}/n, n) = \frac{\lambda_{\mathrm{E,abs}}^k}{n^k} \left(1 - \frac{\lambda_{\mathrm{E,abs}}}{n}\right)^{n-k} \frac{n!}{k!\,(n-k)!} \tag{5.18}$$

As $n \to \infty$ with k finite the binomial formula 5.18 approaches Poisson's distribution.

$$p_{\mathrm{abs}} = \frac{\lambda_{\mathrm{E,abs}}^k}{k!}\, e^{-\lambda_{\mathrm{E,abs}}} \tag{5.19}$$

So the absorption properties of the detector or any other absorber maintain Poisson statistics, what changes is the parameter λ:

$$\frac{\lambda_{\mathrm{E}}^k}{k!}\, e_{\mathrm{E}}^{-\lambda} \qquad \to \qquad \frac{\lambda_{\mathrm{E,abs}}^k}{k!}\, e^{-\lambda_{\mathrm{E,abs}}} \tag{5.20}$$

The square root dependence of the standard deviation on the mean is maintained.

Influence of the Threshold

The threshold in a single photon counting detector will vary around its mean value (presumably according to a Gaussian distribution), similarly the height of the signal from equal energy X-rays will vary (giving a peak distribution with a certain energy resolution as is of interest in spectroscopic devices). If these two distributions overlap significantly, which they will for certain X-ray energies, then on average a certain proportion of events are not registered as their signal height falls below the threshold. The proportion of the signals lost is equal to the fraction of overlapping area, as shown in fig. 5.26. This has an effect similar to that of the absorption efficiency, equally a fraction of the X-rays are not detected and the parameter λ is lowered by the probability of missing an X-ray.
The threshold has therefore no effect on Poisson noise.

Noise Counts

If the noise is independent and random, the probability of getting a noise count in a given time interval will be constant. Then the binomial argument applies which leads to Poisson statistics.
Correlated noise counts may change the noise behaviour, which may lead to non-Poisson noise.

The Rate Dependent Dead Time

The dead time of a photon counting system is determined by the shaping and/or reset time. If more than one event occurs within that time then the excess events will not be registered. The probability of getting two or more hits within the

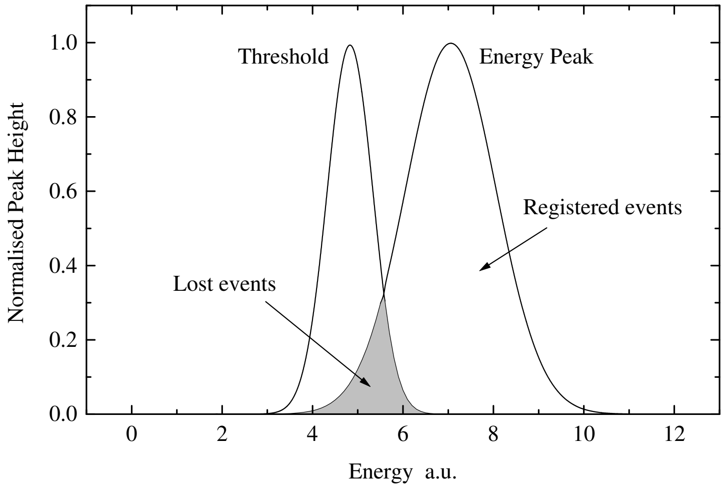

Figure 5.26: Illustration of the influence of the threshold on the event registration. For a given X-ray energy some of the events might fall below the threshold and will therefore not be registered.

shaping time is rate dependent. So the effective dead time increases with increasing rate.
At any given rate every photon will have the same probability of arriving within the dead time of the system. So again the probability is reduced and the binomial argument applies and no change of the noise behaviour is expected.
For a photon counting system Poisson noise should be the only noise source type.

5.3.2 Measurement of the Image Noise

Methods of Data Acquisition for Measuring the Image Noise

Two different ways of measuring the image noise seem reasonable.

1. A homogeneously illuminated detector should show the same signal in all pixels. The difference in the response between pixels should give the image noise.
   This allows the calculation of the image noise from one image. Several images are needed to observe the response to different photon rates.

2. A series of images taken under identical conditions allows the evaluation on a pixel by pixel basis. Each pixel should show the same signal for each exposure.
   Several images are needed in order to calculate the image noise from one

pixel. If the detector is illuminated inhomogeneously, the response to different input signals is acquired simultaneously.

The accuracy of the first measurement will rely on the homogeneity of the pixels and source. For the second approach it is vital to have identical conditions when taking the series of images.
The LAD1 does not show a particularly homogeneous response among different pixels, so the first method can not be applied. To assure identical conditions requires the exposure time to be constant. Since some error will always occur it is vital to keep the contribution of the timing error sufficiently low.

Contribution of the Timing Error

If the error in the exposure time dominates the overall statistical error, a linear dependence of the noise with dose is observed.
The mean number of experimentally observed counts λ will be $\lambda = r\,t$ where t is the exposure time and r is mean rate of the source reduced by any losses. If t has a Gaussian timing error Δt then the probability distribution $f(n,t)$ for the number of counts is

$$f(n,t) = \frac{(r\,t)^n}{n!}\, e^{-r\,t}\, \frac{1}{\sqrt{2\pi}\,\Delta t}\, e^{-\frac{(t-t_0)^2}{2\,\Delta t^2}} \tag{5.21}$$

where t_0 is the mean exposure time.
The expectation value for the number of counts n is

$$< n >= \int dt \sum_n n \frac{(r\,t)^n}{n!}\, e^{-r\,t}\, \frac{1}{\sqrt{2\pi}\,\Delta t}\, e^{-\frac{(t-t_0)^2}{2\,\Delta t^2}} = r\,t_0 \tag{5.22}$$

the second moment $< n^2 >$ is

$$< n^2 >= \int dt \sum_n n^2 \frac{(r\,t)^n}{n!}\, e^{-r\,t}\, \frac{1}{\sqrt{2\pi}\,\Delta t}\, e^{-\frac{(t-t_0)^2}{2\,\Delta t^2}} = r\,t_0 + r^2 t_0^2 + r^2 \Delta t^2 \tag{5.23}$$

The variance is

$$\mathrm{var}(n) =< n^2 > - < n >^2 = r\,t_0 + r^2 \Delta t^2 \tag{5.24}$$

So at a low rate and with accurate timing Poisson noise is observed, whereas for high rate and inaccurate timing the standard deviation on the number of counts increases linearly with increasing rate.
Approximating the timing error with a Gaussian assumes that the negative part of the integral ($t < 0$) can be neglected. This is valid for $t/\Delta t \gtrapprox 3$.

Experimental Verification

The photon counting properties of the ERD1 allow the verification of the timing error.
The data acquisition software can be run in continuous loops. The time it takes to

run one loop has an error Δt_D, which was measured to be $\Delta t_D = 2.16 \pm 0.13$ % of the mean running time of one loop. The error was acquired by measuring the running time of several thousand loops. By defining the exposure time as multiples of loops the timing error increases linearly (assuming Gaussian errors). According to the discussion above the standard deviation should show a non-Poisson, linear dependence on the observed number of counts. The experimental data are plotted in fig. 5.27. From the rate (72.0 $\pm$ 3.2 counts per loop) and the gradient from

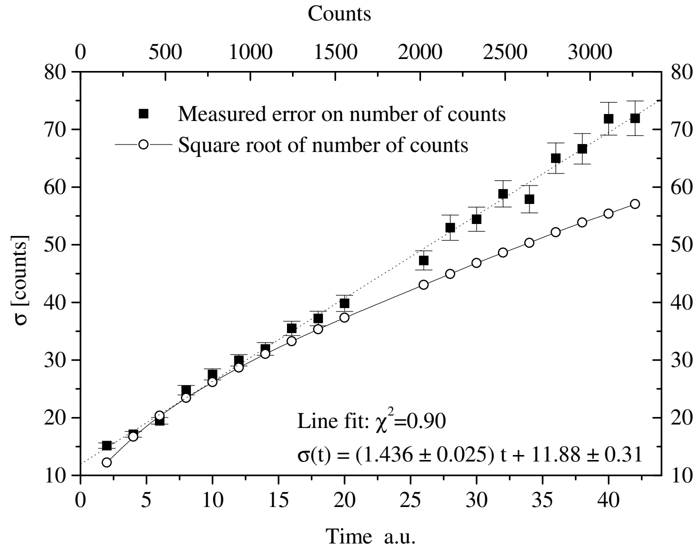

Figure 5.27: Image noise measured with the ERD1 system. The timing error increases linearly with the number of counts and dominates the noise.

the linear fit the timing error can be calculated. The experimental result from the image noise, $\Delta t_I = 1.99 \pm 0.95$ %, is consistent with the directly measured error Δt_D.

The image noise of the LAD1 was measured by acquiring 100 images of a slit under similar conditions. The nominal exposure time was 20 ms; the X-ray source was monochromatic with an energy of 19.5 keV (SRS). For each pixel the mean and standard deviation were calculated. The image of a slit, shown in fig. 5.28, includes pixels with different numbers of counts. For all pixels registering more than 5 counts, the mean number of counts is plotted against the variance in fig. 5.29. A linear fit to the data gives a slope of 0.968 ± 0.019. The pixels denoted as P1, P2 and P3 show a non-Poisson noise behaviour. Since they are outside the illuminated area, (see fig.5.28), they do not receive any photons and are assumed to be “noisy”.

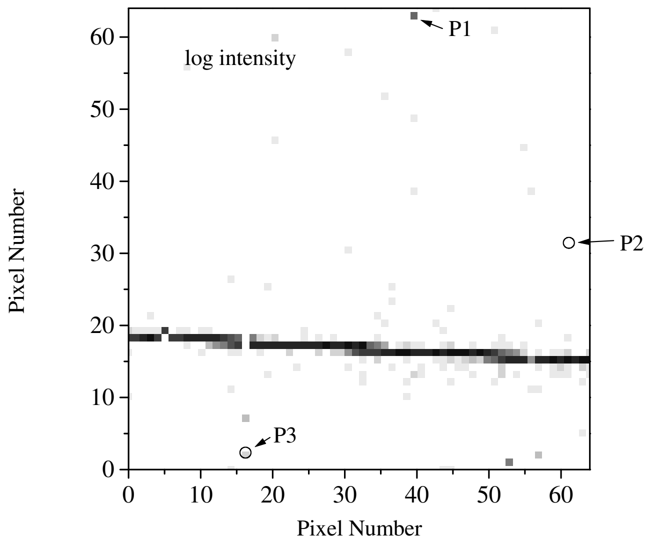

Figure 5.28: Image of the slit used for investigating the image noise. The highlighted pixels are noisy and show a non-Poisson noise behaviour.

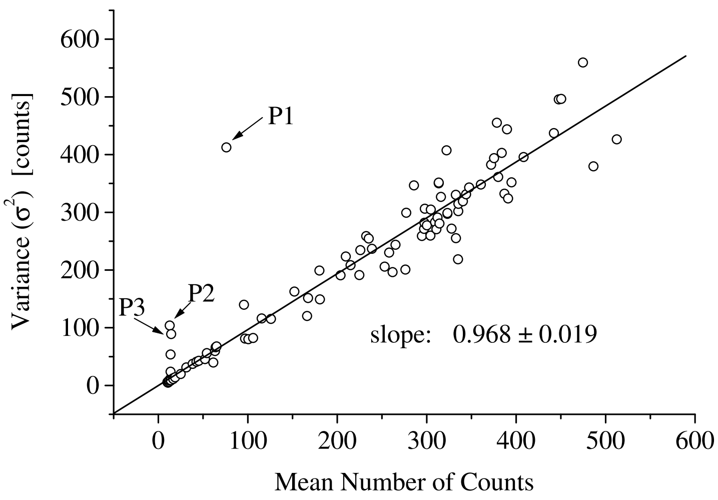

Figure 5.29: The variance is plotted against the mean number of counts. According to Poisson statistics this should give a line with a slope of one.

5.4 Rate Capability

For the LAD1 the rate capability is defined by the shaping time, which can be varied by adjusting the current in the feedback. The initially desired value was around 150 ns. To reduce variations in the pixel response larger shaping times were used.
Due to the Schmitt-trigger the LAD1 is paralysable, so for an increased source rate the number of registered events drops. This was investigated using a slit. For a narrow slit, such as that used for acquiring the LSF, only a small part of a pixel is exposed. By opening the slit the rate on the pixel is increased. An image of a slit with a width greater than the pixel size is shown in fig. 5.30. The

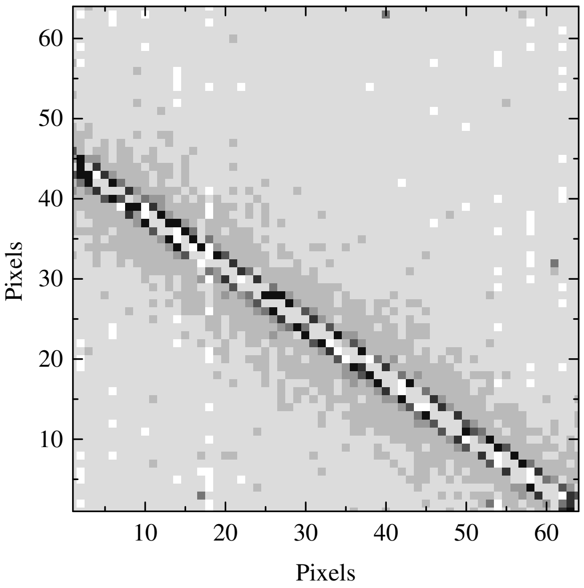

Figure 5.30
Image of a slit several times wider than the pixel pitch. The fully exposed pixels can not cope with the rate and are paralysed.

fully exposed pixels can not cope with the rate and are paralysed. The maximum counts are observed for pixels at the periphery of the slit, which are only partly exposed. The mean rate each pixel acquired is plotted in fig. 5.31. The graph is the histogrammed data shown in fig. 5.30, using a small binning. The highest rate counted by a pixel is 250 k per second (5000 counts in 20 ms). For a given input rate[5] the measured rate can be simulated as a function of the shaping time. In fig. 5.32 the response curves are shown for shaping times of 1.5, 1.75 and 2.0 μs. The maximum observed rate corresponds to a shaping time of around 1.7 μs. At this rate of 250 k counts/s the input rate is about 700 k counts/s.
The maximum observed rate is inversely proportional to the shaping time and should increase considerably with shorter shaping times.

[5] The input rate is the rate of events which are processed by the electronics.

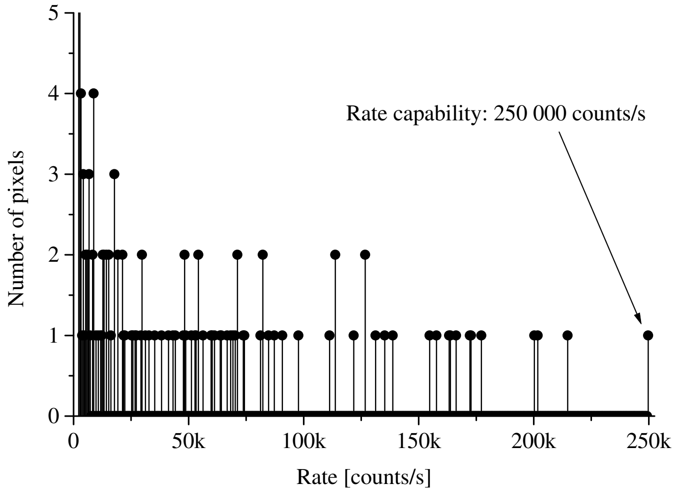

Figure 5.31: Histogram of the rate recorded for each pixel. The maximum rate is around 250 k counts per second.

5.5 Summary and Conclusion

The spatial resolution for pixel detectors was investigated theoretically leading to an analytical formula allowing the calculation of the spatial resolution based on the LSF and MTF. This also led to the prediction that the spatial resolution of a square and hexagonal pixel geometry will not differ significantly for equal pixel areas. For the LAD1 the theoretical value was determined to be 5.3 lp/mm, the experimental value of (5.1 ± 0.1) lp/mm is slightly lower which may be explained from the width of the slit and charge spreading.
It was shown theoretically that for a single photon counting imaging systems the image noise is expected to be given by Poisson statistics. This was confirmed by the experimental results from the LAD1.
The maximum rate capability achieved with the LAD1 was 250 kHz per pixel.

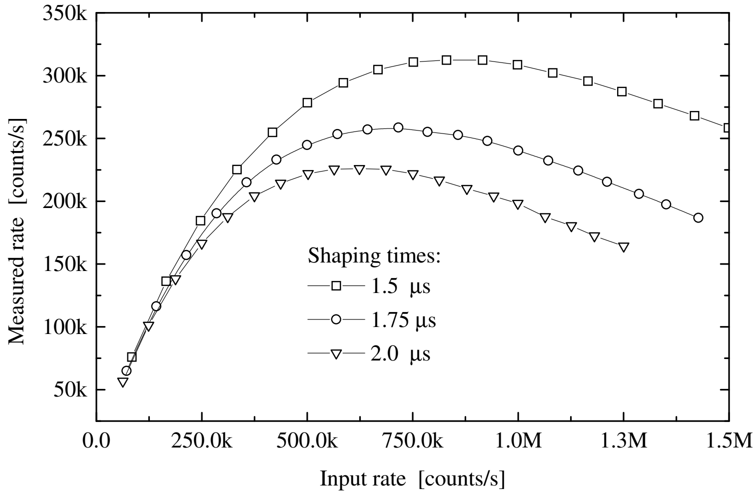

Figure 5.32: Simulation of the observed rate as a function of the input rate for three different shaping times.

Chapter 6

General Investigations

This chapter contains two sections. The first discusses the difference in contrast between ideal integrating and photon counting systems. The second is based on simulations and analytical calculations and discusses the small pixel effect and related phenomena.

6.1 Difference in Contrast in Ideal Integrating and Photon Counting Systems

6.1.1 Introduction

Recent developments in detectors for X-ray imaging are increasingly based on photon counting rather than the conventional charge integrating method, for reasons of a larger dynamic range and the ability to suppress low energy events (due to effects of charge sharing or leakage currents for example). An evaluation of the image quality can be achieved by comparing the contrast given by either system. A recent publication [Per98], based on Monte Carlo simulation studies indicates a better contrast for photon counting systems.
This chapter is intended to give a more general picture of the difference in contrast, which does not contradict the above mention work, but rather extends it.
The derivations below assume the following: Both the integrating and photon counting system are digital, giving a monochromatic picture (gray scale image). To enable a comparison it is also assumed that the images are normalised, i.e. both have values ranged between '1' and '0' (black and white respectively). This seems adequate for digital systems since the data can always be normalised to the full range, i.e. black to white.

6.1.2 Derivation of the Signal gained from Photon Counting and Integrating Systems

An X-ray source of various energies, will be described in what follows by a flux distribution $I(E_i)$. This function has the dimension s^{-1} as it refers to the number of photons of a certain energy emitted per unit time.

$$Source = I(E_i) \tag{6.1}$$

The signal gained from an integrating system can be described by:

$$Signal_{\mathrm{I}} = \sum_{i=1}^{n} I(E_i)\; E_i\; c \tag{6.2}$$

Where c is a constant. In terms of semiconductor detectors where the signal is the charge collected at the electrode, c is the inverse of the energy needed to create an electron hole pair.
The signal gained from a photon counting system is:

$$Signal_{\mathrm{C}} = \sum_{i=1}^{n} I(E_i) \tag{6.3}$$

This is simply adding up all the incoming photons.
Equations 6.2 and 6.3 can be considered to give the maximum signal, defined as '1'. An absorber will change the signal according to the following equations:

$$Signal_{\mathrm{I,abs}} = \sum_{i=1}^{n} I(E_i)\; E_i\; c\; f(E_i) \tag{6.4}$$

$$Signal_{\mathrm{C,abs}} = \sum_{i=1}^{n} I(E_i)\; f(E_i) \tag{6.5}$$

Where $f(E)$, a function that describes the absorber, is of the form:

$$f(E) = \prod_{k=1}^{m} e^{-\alpha_k(E)\rho_k w_k} = e^{-\sum_{k=1}^{m} \alpha_k(E)\rho_k w_k} \tag{6.6}$$

where $\alpha(E)$ is the energy dependent mass absorption coefficient of the material of density ρ and thickness w. The product (exponential sum) takes into account that the absorber might be composed of several materials of different thicknesses.
f has the following properties:

$$0 \leq f \leq 1 \qquad , \qquad E_i > E_j \Leftrightarrow f(E_i) > f(E_j) \tag{6.7}$$

The latter expression is true because α decreases with increasing energy (the absorption edge discontinuities in the photo electric effect are neglected).

The normalised signal can now be written as:

$$S_{\mathrm{I}} = \frac{\sum_{i=1}^{n} I(E_i)\ E_i\ c\ f(E_i)}{\sum_{i=1}^{n} I(E_i)\ E_i\ c} \tag{6.8}$$

$$S_{\mathrm{C}} = \frac{\sum_{i=1}^{n} I(E_i)\ f(E_i)}{\sum_{i=1}^{n} I(E_i)} \tag{6.9}$$

The constant c cancels from the expression for the integrating system. For the comparison of the two, it is convenient to introduce the parameter a_n, defined by:

$$S_{\mathrm{I}} = a_n S_{\mathrm{C}} \tag{6.10}$$

a_n depends on the number of different energies contributing to $I(E)$. If $a_n > 1$ then the photon counting system gives less intensity , if $a_n < 1$ the integrating system does.
Considering first a monochromatic source, it is expected that there will be no difference in the intensity as the amount of energy gathered by the integrating system is a multiple of the number of photons detected.
$n = 1$:

$$S_{\mathrm{I}1} = \frac{I(E_1)\ E_1\ f(E_1)}{I(E_1)\ E_1} = f(E_1) \tag{6.11}$$

$$S_{\mathrm{C}1} = \frac{I(E_1)\ f(E_1)}{I(E_1)} = f(E_1) \tag{6.12}$$

Therefore $a_1 = 1$ and there is no difference in the intensity, as expected.
In the general case where n different energies are involved, the procedure is the same. So equation 6.10 may be written

$$\frac{\sum_{i=1}^{n} I(E_i)\ E_i\ f(E_i)}{\sum_{i=1}^{n} I(E_i)\ E_i} = a_n\ \frac{\sum_{i=1}^{n} I(E_i)\ f(E_i)}{\sum_{i=1}^{n} I(E_i)} \tag{6.13}$$

or

$$\sum_{j=1}^{n} I(E_j) \sum_{i=1}^{n} I(E_i)\ E_i\ f(E_i) = a_n \sum_{j=1}^{n} I(E_j)\ f(E_j) \sum_{i=1}^{n} I(E_i)\ E_i \tag{6.14}$$

Each side of this equation has n^2 terms, and any term on either side can be identified by $(..)_{ij}$. Comparing the terms $(..)_{ij} + (..)_{ji}\ \ i \neq j$ on either side of the equation gives:

$$\begin{gathered} I(E_j)I(E_i)E_i f(E_i) + I(E_i)I(E_j)E_j f(E_j) = \\ a_{n,ij}\ [I(E_j)f(E_j)I(E_i)E_i + I(E_i)f(E_i)I(E_j)E_j] \end{gathered} \tag{6.15}$$

where $a_{n,ij}$ is defined in a similar way as a_n. This leads to the expression

$$a_{n,ij} = \frac{E_i f(E_i) + E_j f(E_j)}{E_i f(E_j) + E_j f(E_i)} \tag{6.16}$$

Defining $E_i = p_E E_j$ and $f(E_i) = p_f f(E_j)$, with $p_E, p_f > 0$. From the above it follows that $p_E \gtrless 1 \Leftrightarrow p_f \gtrless 1$. Using these relations in equation 6.16 yields:

$$a_{n,ij} = \frac{p_E p_f + 1}{p_E + p_f} \quad > 1 \tag{6.17}$$

In the case of $i = j$, $p_E = p_f = 1$ and the result is trivial, $a_{n,ii} = 1$. To illustrate that all n^2 terms have been considered exactly once, the terms $(..)_{ij}$ may be treated as elements of an $n \times n$-matrix. Equation 6.16 takes all elements into account that are not on the diagonal of the matrix, each giving $a_{n,ij} > 1$, whereas all diagonal terms give $a_{n,ii} = 1$.
Consequently the integrating system always shows a higher signal than the photon counting system.

Comment

It was assumed that no absorber was shielding the detector hence 1 (maximum intensity) was defined as

$$\begin{aligned} Signal_{\mathrm{I}} &= \sum_{i=1}^{n} I(E_i)\, E_i\, c \\ Signal_{\mathrm{C}} &= \sum_{i=1}^{n} I(E_i) \end{aligned} \tag{6.18}$$

for the integrating and photon counting system respectively. If the maximum signal seen with the detector is not the pure source but that seen through some absorber, this will not make any difference to the above calculations as $I(E)$ can simply be redefined. Similarly the absorption properties of the detector can be taken into account by redefining $I(E)$. This is possible since the detector is an absorber and therefore commutative.

6.1.3 Renormalisation

In the above derivation 0 intensity was defined as zero photons detected. This will in general not be the case as some X-rays might be detected through any thickness of absorber. Therefore the normalisation would differ from the above. The above expressions would then change to the renormalised equations:

$$S_{\mathrm{I,renorm}} = \frac{S_{\mathrm{I}} - S_{\mathrm{I,min}}}{1 - S_{\mathrm{I,min}}} \tag{6.19}$$

$$S_{\mathrm{C,renorm}} = \frac{S_{\mathrm{C}} - S_{\mathrm{C,min}}}{1 - S_{\mathrm{C,min}}} \tag{6.20}$$

Where

$$S_{\mathrm{I,min}} = \frac{\sum_{i=1}^{n} I(E_i)\ E_i\ f_{\mathrm{min}}(E_i)}{\sum_{i=1}^{n} I(E_i)\ E_i} \tag{6.21}$$

and

$$S_{\mathrm{C,min}} = \frac{\sum_{i=1}^{n} I(E_i)\ f_{\mathrm{min}}(E_i)}{\sum_{i=1}^{n} I(E_i)} \tag{6.22}$$

f_{min} is the absorber which will absorb most and therefore give the least intensity. Equations 6.19 and 6.20 simplify to

$$S_{\mathrm{I,renorm}} = \frac{\sum_{i=1}^{n} I(E_i)\ E_i\ (f(E_i) - f_{\mathrm{min}}(E_i)}{\sum_{i=1}^{n} I(E_i)\ E_i\ (1 - f_{\mathrm{min}}(E_i))} \tag{6.23}$$

$$S_{\mathrm{C,renorm}} = \frac{\sum_{i=1}^{n} I(E_i)\ (f(E_i) - f_{\mathrm{min}}(E_i))}{\sum_{i=1}^{n} I(E_i)\ (1 - f_{\mathrm{min}}(E_i))} \tag{6.24}$$

Defining

$$J := I\ (1 - f_{\mathrm{min}}) \qquad g := \frac{f - f_{\mathrm{min}}}{1 - f_{\mathrm{min}}}$$

leads to equations similar to 6.8 and 6.9:

$$S_{\mathrm{I}} = \frac{\sum_{i=1}^{n} J(E_i)\ E_i\ c\ g(E_i)}{\sum_{i=1}^{n} J(E_i)\ E_i\ c} \tag{6.25}$$

$$S_{\mathrm{C}} = \frac{\sum_{i=1}^{n} J(E_i)\ g(E_i)}{\sum_{i=1}^{n} J(E_i)} \tag{6.26}$$

From the definition of g it is clear that $0 < g < 1$, however in order to conclude that in the renormalised case the integrating system will give a higher intensity than a photon counting device, it must be shown that, for any E_i, E_j, with $E_i > E_j$, $g(E_i) > g(E_j)$. This follows from the earlier assumption that $E_i > E_j$ gives $f_i > f_j$, by subtracting f_{min} and dividing by the positive number $1 - f_{\mathrm{min}}$ on either side

$$g(E_i) = \frac{f(E_i) - f_{\mathrm{min}}}{1 - f_{\mathrm{min}}} > \frac{f(E_j) - f_{\mathrm{min}}}{1 - f_{\mathrm{min}}} = g(E_j) \tag{6.27}$$

This allows the conclusion that an ideal charge integrating system will always give a higher signal than a photon counting system.

6.1.4 Difference in Contrast

The contrast of an absorber *df* can be defined as the gradient of the equations 6.8 and 6.9 with respect to the absorber[1]. For a linearly increasing absorber the exponential behaviour is plotted in fig. 6.1.

The difference between the responses is banana shaped, therefore as both curves

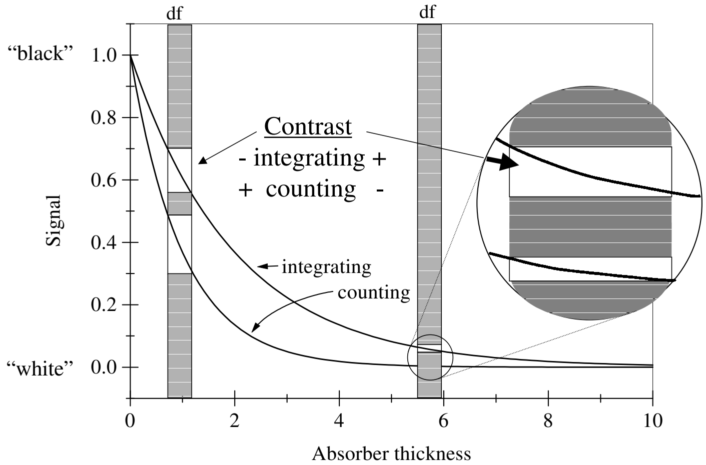

Figure 6.1: Response of a photon counting and an integrating system with linearly increasing absorber. A given absorber df at the low absorbing side will give a higher contrast for the photon counting device, whereas the same absorber at the highly absorbing side will show more clearly in the integrating system.

start and end at the same point (in the renormalised case) the average gradient must be the same. As the gradient of the photon counting system is higher for lower absorber thicknesses, the integrating system must give a higher contrast for thick absorbers, as illustrated in fig. 6.1.

6.1.5 Experimental Verification

The experimental verification used the ERD1 system, described in section 3.1. This 16 by 16 pixel array detector outputs the analogue value corresponding to

[1]The absorber may change in density and/or thickness. A linearly increasing absorber corresponds to a linearly increasing exponent in the absorption function (not necessarily a linearly increasing thickness).

the energy of the detected X-ray as well as the pixel number. This allows a direct comparison of the photon counting and integrating read-out using the same data. A copper wedge with a maximum thickness of 0.06 cm was used as an absorber, see fig. 6.2. For the measurements half of the detector was active, i.e. an array of 8 by 16 pixels, with a pixel size of 300 μm by 300 μm. 16 different shades of gray

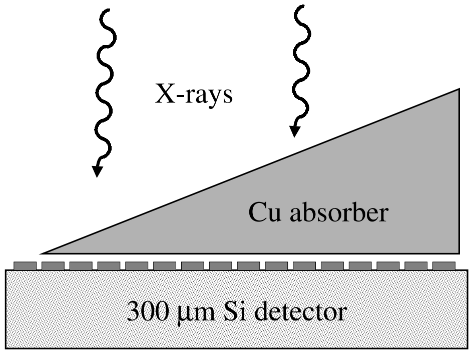

Figure 6.2
Schematic set-up of the detector with the copper absorber. The detector was homogeneously illuminated with X-rays.

are expected, each shade given from a row of 8 pixels. In order to achieve higher statistics data from these 8 pixels were combined. The source was a distribution of discrete lines from a variable X-ray source, in which an ^{241}Am source excites a Cu, Rb, Mo, Ag, Ba or Tb target which then emits characteristic X-rays. The following lines were used for the measurement: 22.10 keV (K_α of Ag), 32.06 keV (K_α of Ba), 44.23 keV (K_α of Tb) and 50.65 (K_β of Tb).
To simulate an ideal detector the data for each line were cut, so that only the photo peak contributes to the image. The energy resolution of the detector is around 1 keV so the K_β peaks of Ag and Ba could be omitted.
For each line the intensity of the brightest point (no absorber) was normalised to 1. Thus the energy distribution of the source weighted with the detector absorption is:
$I(E)\ A_{\text{detector}} = \delta(E-22.10) + \delta(E-32.06) + \delta(E-44.23) + \delta(E-50.65)$
where A_{detector} is the absorption function of the 300 μm thick Si detector. The data needed for the calculation were taken from ref. [NIST]. The results of the measurement are shown in fig. 6.3 and fig. 6.4 for the direct and the renormalised case, respectively. The theoretically calculated curves are included in the graphs.

The error bars for the experimental data are due to statistics. Any errors arising from the placement and non-linear increase in thickness of the absorber are neglected. Averaging over slightly different absorber thicknesses is also neglected, as well as the fact that not all X-rays are normal to the detector surface.
From the data displayed in fig. 6.4 the image of the object shown in fig. 6.5 can be extracted. The resulting images are shown in fig. 6.6. The numbers correspond to the signal acquired in each area. The photon counting mode shows a higher contrast in the left part of the image, whereas the integrating mode prevails on the right side.

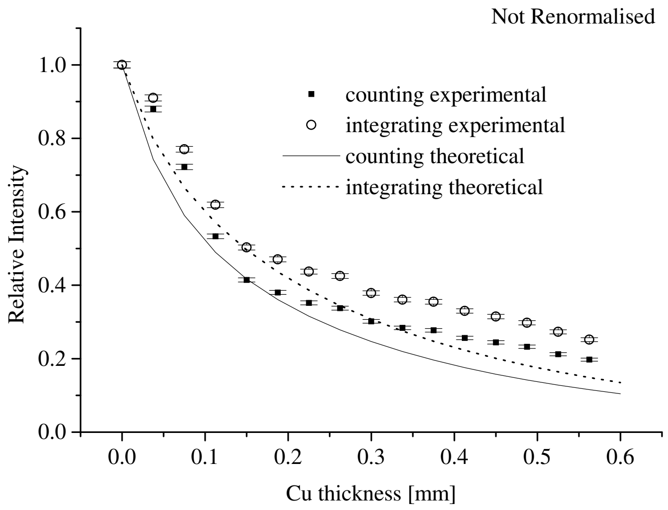

Figure 6.3: Comparison of the theory with the experiment for the non-renormalised case.

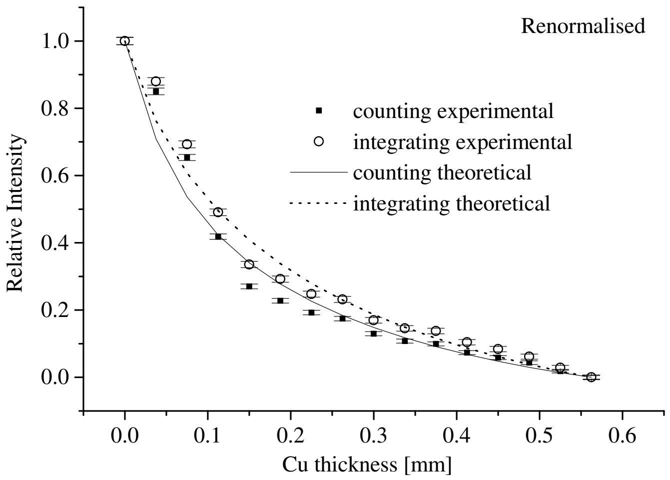

Figure 6.4: Comparison of the theory with the experiment for the renormalised case.

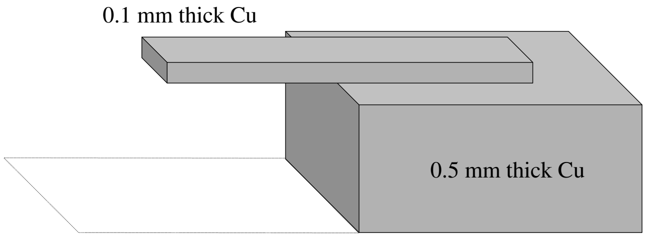

Figure 6.5
Object corresponding to the image shown below, fig. 6.6.

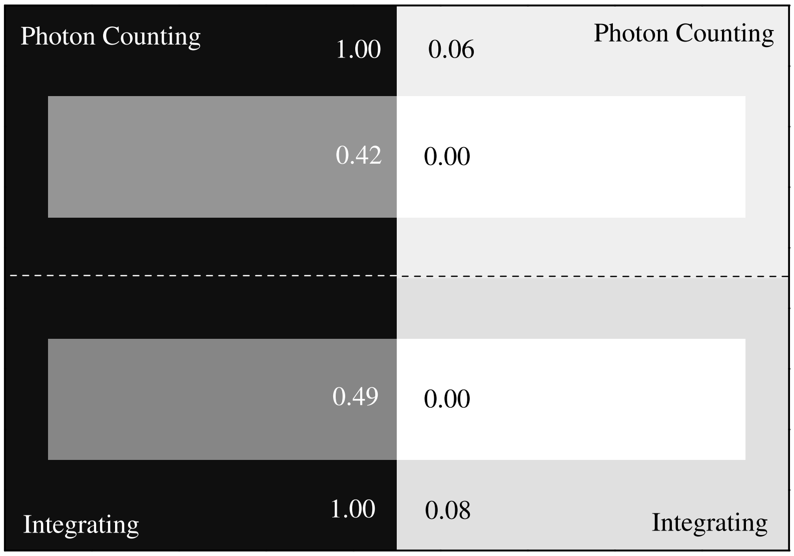

Figure 6.6: Image showing the difference in contrast for integrating and photon counting systems. The numbers correspond to the signal seen in each area. The images were put together from the experimental data plotted in fig. 6.4.

6.1.6 The Definition of Contrast

In the above discussion the contrast was defined as the difference in gray scale, i.e.

$$\text{Contrast}_1 = \text{SIGNAL(background)} - \text{SIGNAL(object)}. \tag{6.28}$$

This may be considered a valid and reasonable definition.
The following definition of contrast is however more common:

$$\text{Contrast}_2 = \frac{\text{SIGNAL(background)} - \text{SIGNAL(object)}}{\text{SIGNAL(background)}} \tag{6.29}$$

This definition is identical to the above if SIGNAL(background)=1, i.e. this is the maximum signal. A straightforward choice between the two definitions is not trivial, as illustrated in fig. 6.7 in which each of the four rows shows objects which have the same contrast. Both definitions have some validity. Column 1 and 4 use

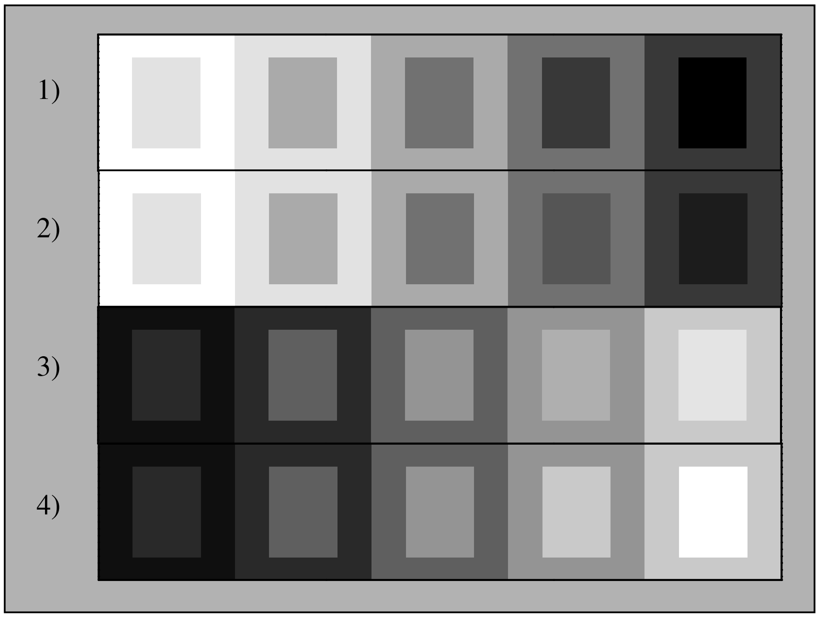

Figure 6.7: The four rows each contain five objects which all have the same contrast. Row 1 and 4 use the definition of equation 6.28, row 2 and 3 of equation 6.29.

the definition of equation 6.28, row 2 and 3 of equation 6.29. All objects have a contrast of 0.2. Row 1 is the inverse image of row 4 and row 2 the inverse of row 3. The background signal varies from 1.0 (far left) to 0.2 (far right) in all rows and the object signal varies correspondingly.
Applying the definition from equation 6.29 to the above calculations proves to be

difficult in the general case. The contrasts of the integrating and photon counting systems may be written as

$$\begin{aligned} C_\mathrm{I} &= 1 - \frac{\sum_{i=1}^{n} I(E_i)\ E_i\ f_2(E_i)}{\sum_{i=1}^{n} I(E_i)\ E_i\ f_1(E_i)} \\ C_\mathrm{C} &= 1 - \frac{\sum_{i=1}^{n} I(E_i)\ f_2(E_i)}{\sum_{i=1}^{n} I(E_i)\ f_1(E_i)} \end{aligned} \tag{6.30}$$

for the integrating and photon counting system, respectively, where f_1 and f_2 are the absorption functions leading to SIGNAL(background) and SIGNAL(object) respectively.
A similar approach to that used above yields

$$\frac{\sum_{i=1}^{n} I(E_i)\ E_i\ f_2(E_i)}{\sum_{i=1}^{n} I(E_i)\ E_i\ f_1(E_i)} = b_n\ \frac{\sum_{i=1}^{n} I(E_i)\ f_2(E_i)}{\sum_{i=1}^{n} I(E_i)\ f_1(E_i)} \tag{6.31}$$

where b_n is a constant analogous to a_n. In this case however $b_n > 1$ would directly indicate a better contrast for the photon counting system and $b_n < 1$ would favour the integrating mode.
A solution is possible under the assumption that $f_2(E_i) = f_1(E_i)\, f_3(E_i)$ where

$$0 \le f_3 \le 1 \qquad \text{and} \qquad E_i > E_j \Leftrightarrow f_3(E_i) > f_3(E_j). \tag{6.32}$$

So f_3 has the properties of an absorber function and could be an absorber. Defining $J(E_i) = I(E_i)\, f_1(E_i)$ and substituting this in equation 6.31 leads to

$$\frac{\sum_{i=1}^{n} J(E_i)\ E_i\ f_3(E_i)}{\sum_{i=1}^{n} J(E_i)\ E_i} = b_n\ \frac{\sum_{i=1}^{n} J(E_i)\ f_3(E_i)}{\sum_{i=1}^{n} J(E_i)}. \tag{6.33}$$

This is equivalent to equation 6.13 and therefore $b_n > 1$, which means that a photon counting system will always show a better contrast than the integrating mode, according to the definition of equation 6.29.
The definition from equation 6.29 is unsatisfactory when SIGNAL(object)=0. The contrast would always be 1, regardless of SIGNAL(background). A major difference is that this definition allows any number of objects within one image which all have the same contrast. This is not possible with the definition of equation 6.28.

6.1.7 Conclusion

Here only ideal systems have been considered, with no charge sharing and complete charge collection efficiency. Any deteriorating effects from multiple scattering, electronic noise, charge collection inefficiency and charge sharing have been neglected. It may be concluded that the difference in contrast varies, depending on the definition of contrast. However fig. 6.6 shows that the contrast of an object may be better in the photon counting or integrating system depending on the background.

6.2 The Small Pixel Effect

The small pixel effect is investigated on the basis of simulations and analytical calculations. The drift and weighting fields and potentials were simulated in MEDICI [MED99] and allow the calculation of the induced charge for any mean free drift lengths of the carriers. This allows the study of effects in semiconductor detectors which are experimentally tedious or impossible (changing the mean free drift length) to measure.
Three different effects are discussed: charge sharing, unipolar sensing and the small pixel effect.
Direct simulation of the CCE is simple but not practical if a large number of different drift lengths and interaction points are considered (the simulation requires a substantial amount of time to run). MEDICI is a 2-dimensional simulation package, so edge effects are correctly simulated but corner effects are not taken into account. The results are therefore for a strip detector with various strip widths rather than for a pixel geometry. The effect is the same however and collecting contacts will be referred to as pixels.

6.2.1 Considered Geometries

A 300 μm thick Si detector with pixel sizes of 100, 50 and 10 μm was simulated. Two different biasing conditions are investigated, full depletion and massive over depletion (bias voltage = 10 times full depletion voltage). The simulated width is 200 μm in all cases, the exact geometry of the devices is given in fig. 6.8. The three different pixels sizes will be referred to as large, medium and small and the two biasing conditions as full depletion and over depletion.
The signal is extracted from the central pixel. Neumann boundary conditions are imposed on the sides, so the normal component of the electric field is zero at the sides of the simulated section. Terminating the pixels exactly at their centre is therefore accurate since the normal component of the electric field must vanish for symmetry reasons. This is true for the large and medium pixel size. For the small pixels it is assumed that only the adjacent pixel will effect the fields, so that the continuous metallisation is a valid approximation.
Although only one specific dimension is considered here, the results can be scaled to any detector thickness. The results only depend on the ratio of the pixel size to the detector thickness. Similarly the mean free drift length can be expressed in units of the detector thickness.

6.2.2 Calculation of the Charge Collection Efficiency

The drift field allows the calculation of the flow lines, i.e. the average path along which the charge carriers move. The weighting potential is then used to calculate the CCE as a function of the mean free drift lengths of the carriers moving towards

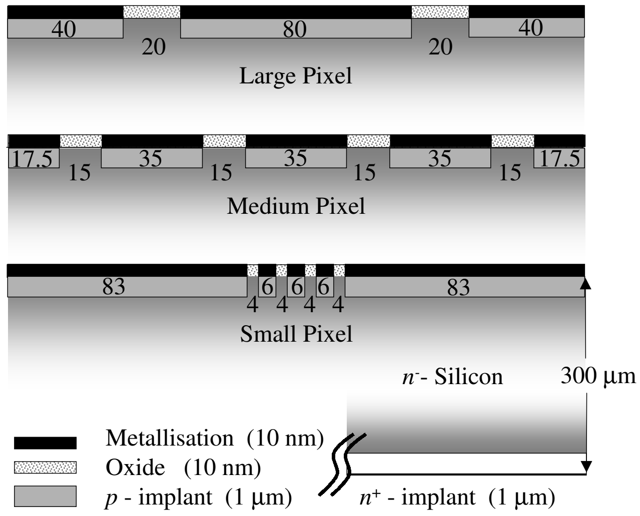

Figure 6.8: Dimensions of the three simulated geometries.

and away from the pixel. The flow lines for the three different pixel sizes are shown in fig. 6.9. These lines are extracted from the simulated drift fields. At any point the field is calculated from the 4 closest nodes by linear interpolation. The calculation of the CCE uses the weighting potentials rather than the weighting fields. The weighting potentials for the three different pixel sizes and two biasing conditions are shown in fig. 6.10. Using the flow lines or path of the carriers and weighting potentials to calculate the CCE reduces the 2-dimensional problem to 1-dimension. The CCE is given by

$$\mathrm{CCE} = \sum_{i=k}^{n} dQ_i \, dV_{w,i} + \sum_{j=0}^{k} dQ_j \, dV_{w,j} \tag{6.34}$$

where n is the number of steps along the carrier's path[2] , dV is the difference in the weighting potential across the step and dQ is the charge moving along the path. k is the index which corresponds to the interaction point and the two sums in equation 6.34 correspond to the two carriers, one moving towards the other away from the collecting contact.
If $dQ = 1$ for all steps (no charge loss) then CCE=1, since the weighting potential is normalised. In general dQ is given by

$$dQ_l = e^{-d_l/\lambda_l} \qquad l \in \{1, 2\} \tag{6.35}$$

[2]Several thousand steps are calculated for each path, with the step size varied in inverse proportion to the magnitude of the weighting potential, so that the amount of signal generated for each step does not fluctuate too strongly.

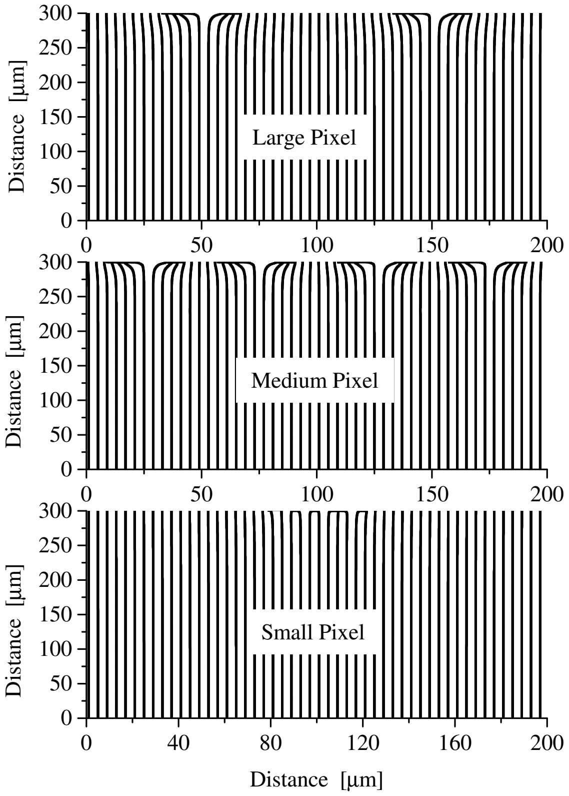

Figure 6.9: Flow lines of the drift field for the three different pixel dimensions.

where λ_l is the mean free drift length and d_l is the distance from the interaction point.
An example is illustrated in fig. 6.11, which shows the interaction point, the generated signal, dQ, the maximum signal and the weighting potential as a function of the position in the 300 μm thick Si detector. The carrier drifting towards the back contact (carrier 1) hardly generates any signal since the weighting potential is small. The loss of the carriers (straight line) does not significantly affect the CCE since the weighting potential is negligible close to the back contact. Carrier 2 which moves towards the pixel travels only half the distance but generates most of the signal. The CCE in the above example is around 24 %. The weighting potential strongly increases closer to the pixel. The loss of charge in that region leads to the low CCE.

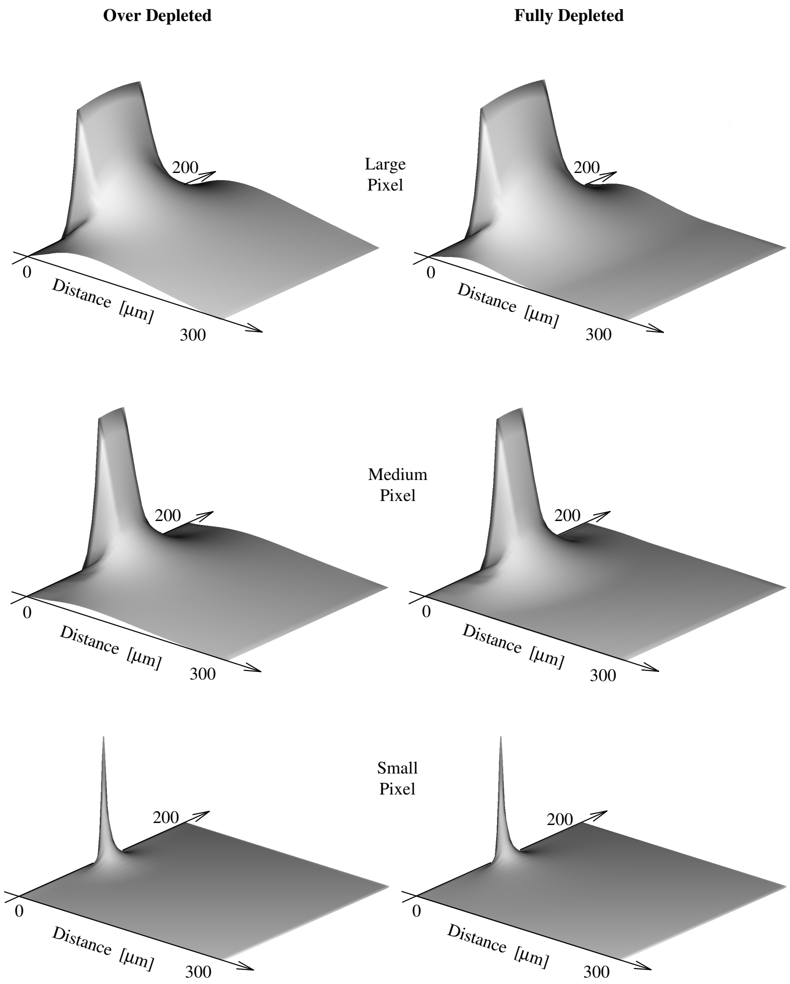

Figure 6.10: Weighting potential for the three different pixel sizes. The left and right column show the weighting potentials for over and full depletion, respectively.

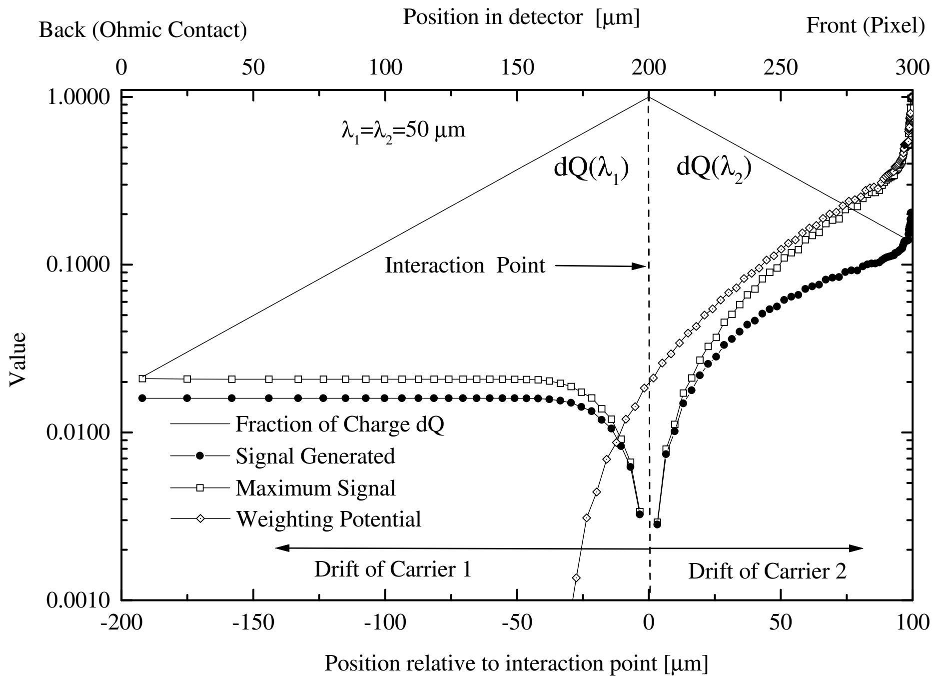

Figure 6.11: Illustration of the signal generation. Due to the loss of the carriers (straight line) the signal generated (solid circles) along the carriers paths is less than the maximum signal (open squares).

6.2.3 Charge Sharing

Since no spread of the charge cloud is considered charge sharing will only occur due to the mean free drift length of the carriers. The interesting regions are those close to the pixel edge. Fig. 6.12 shows the weighting potentials close to the centre of the pixel gap (1 μm from either side of the pixel boundary). The travelled distance is larger than the detector thickness since the carriers travel parallel to the pixel surface before reaching the contact. The weighting potentials in fig. 6.12 show how the main part of the collected charge is induced during the final section of the carrier's path, when it travels parallel to the contacts. Charge sharing occurs if the carriers are lost before passing through the critical region. A carrier moving just outside the pixel boundary will generate a similar signal to one moving just inside, if they are both lost before entering the critical region then both will give rise to a similar signal.
The medium pixel size is used as an example. Fig. 6.13, 6.14 and 6.15 show the CCE for all interaction positions across the detector for different mean drift lengths of the carriers.

For long mean free drift lengths, fig. 6.13, an interaction outside the pixel area has no net effect on the pixel. For unipolar detectors, fig. 6.14, a negative signal

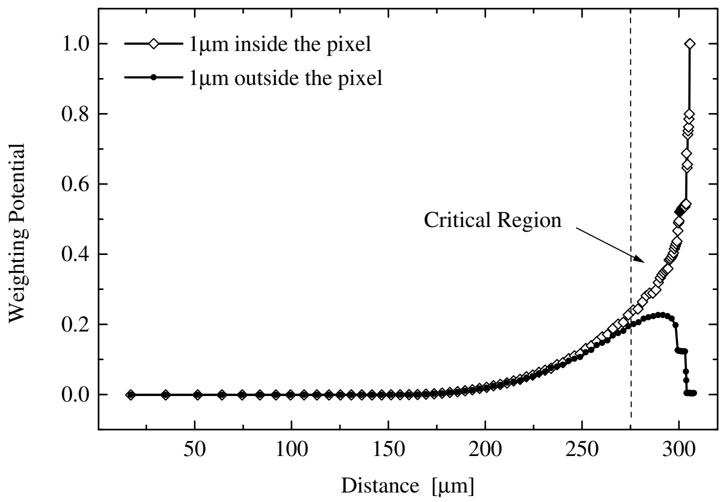

Figure 6.12: Weighting potentials close to the pixel boundary. The region close to the pixellated side is critical. Only in that region will the main signal be generated or lost.

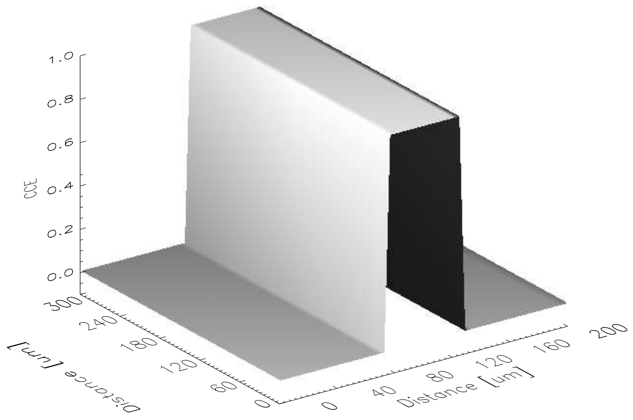

Figure 6.13
CCE across the detector for long mean free drift lengths (1 m) of both carriers. Any interaction below the pixel is fully collected. No signal is seen if the interaction occurs outside the pixel area.

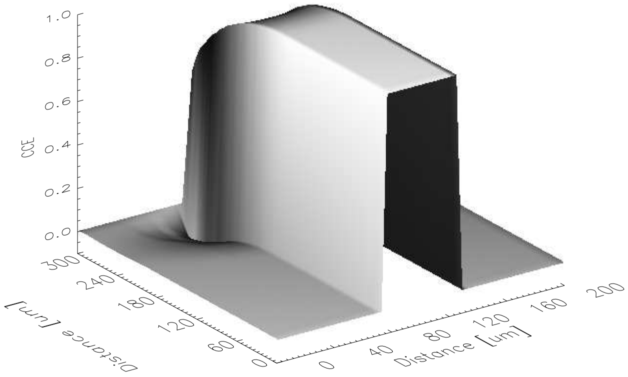

Figure 6.14
CCE across the detector for single carrier mobile carrier. The mean free drift length of the carrier moving towards the pixel is large (1 m) the other is zero. Negative or positive signal may be generated depending on the interaction position.

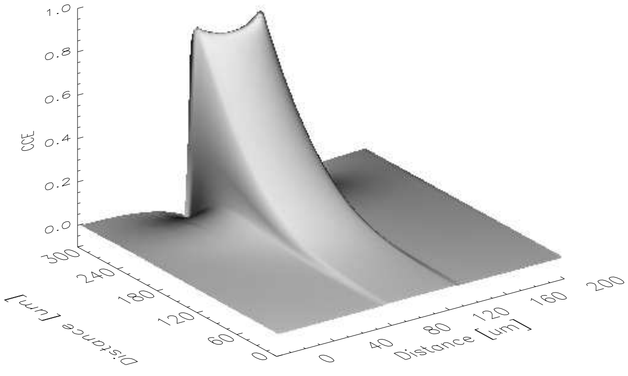

Figure 6.15
CCE across the detector for mean free drift lengths of 50 μm for both carriers. Charge sharing occurs due to the loss of the carriers around the region of high weighting fields, just outside the pixel area (humps on either side of pixel region).

is induced on the pixel if the interaction occurs outside the pixel and in a region with a high weighting potential. Short mean free drift lengths of both carriers, fig. 6.15, can result in a negative or positive (charge sharing) signal being induced, depending on the weighting potential around the interaction point.

6.2.4 Unipolar Sensing

Unipolar sensing is used in materials, such as Cd(Zn)Te which have a high mean free drift length of one carrier and a poor mean free drift length of the other. By significantly reducing the signal contribution of the poor carrier, the spectral and imaging performance can be enhanced. This is achieved by concentrating the weighting field along the path of the carrier with the long drift length, which can be realised by using small pixels, which concentrate the weighting field close to the collecting electrode.
Fig. 6.16(a)-6.16(f) show the pulse height spectra for the different pixel sizes and biasing conditions. The absorption is assumed to be constant over the whole detector and the carrier with the long mean free drift length is collected. The mean free drift lengths of the carriers are 0 and 1 m for the carrier moving towards the back and pixellated contact, respectively. The integrated signal, i.e. the percentage of all charge generated inside the pixel is given in each plot. This is what an integrating imaging system would acquire.
The fully depleted cases always show a better performance, which is due to the weighting field being more constrained to the pixellated contact[3]. The performance increases with smaller pixel size for the same reason. So for a unipolar detector the performance can be increased by decreasing the pixel size and concentrating the weighting field close to the pixel.
For low energy X-rays which are absorbed soon after entering the detector the CCE can be virtually 100 % for all interactions, provided the carrier with the long mean free drift length travels across the device.

6.2.5 The Small Pixel Effect

In fig. 6.16(a)-6.16(f) the peak in the pulse height spectra is always at 100 % CCE, because the carrier generating the signal is not lost. If the mean free drift lengths of the carriers are not sufficient to provide full collection the peak in the pulse height spectra will shift to a lower CCE. For the case of similar mean free drift lengths for both carriers similar pulse height spectra are plotted in fig. 6.17(a)-6.17(f). With decreasing pixel size the maximum CCE increases. This is referred to as the “small pixel effect” and is used to improve the CCE of the photo peak.

[3]This is the case because the mean free drift length of the carriers is the same. For a given detector the performance will increase with higher bias voltage because the mean free drift length (velocity) will increase, unless it is operated in the saturation region.

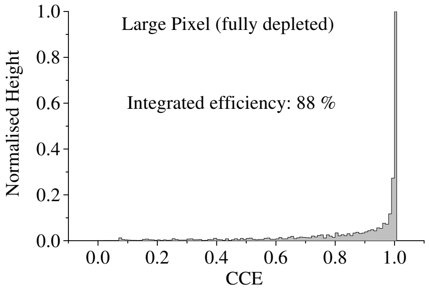

(a) Pulse height spectrum for the large pixel, fully depleted.

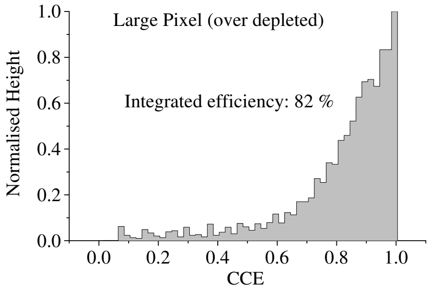

(b) Pulse height spectrum for the large pixel, over depleted.

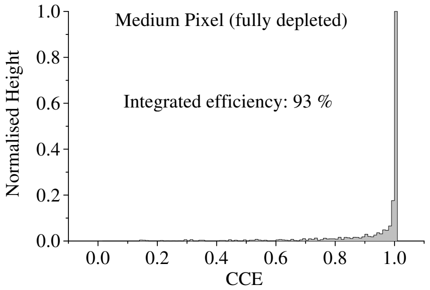

(c) Pulse height spectrum for the medium pixel, fully depleted.

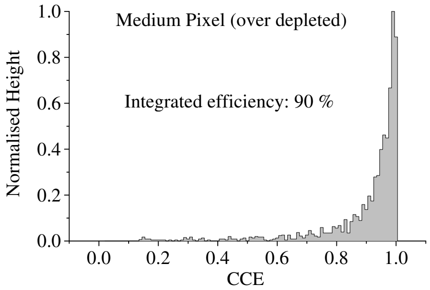

(d) Pulse height spectrum for the medium pixel, over depleted.

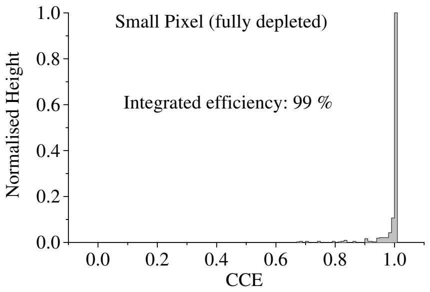

(e) Pulse height spectrum for the small pixel, fully depleted.

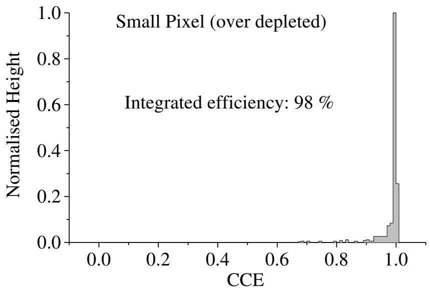

(f) Pulse height spectrum for the small pixel, over depleted.

Figure 6.16: Pulse height spectra of the different sized pixels for a unipolar detector.

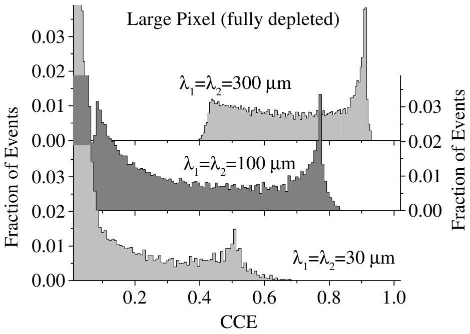

(a) Pulse height spectra for the large pixel, fully depleted.

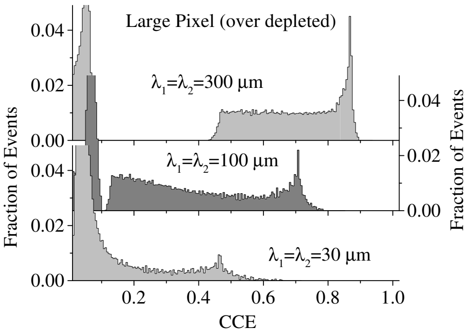

(b) Pulse height spectra for the large pixel, over depleted.

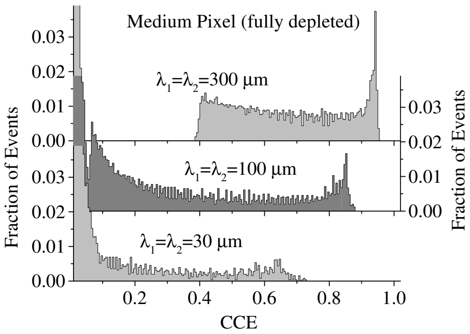

(c) Pulse height spectra for the medium pixel, fully depleted.

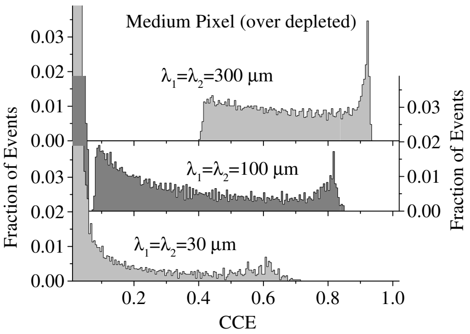

(d) Pulse height spectra for the medium pixel, over depleted.

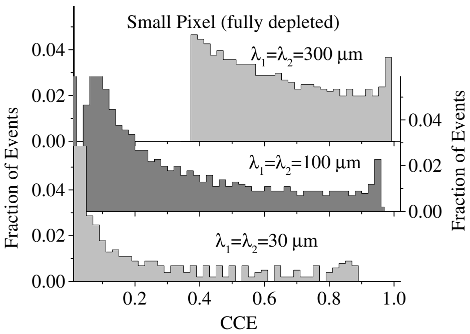

(e) Pulse height spectra for the small pixel, fully depleted.

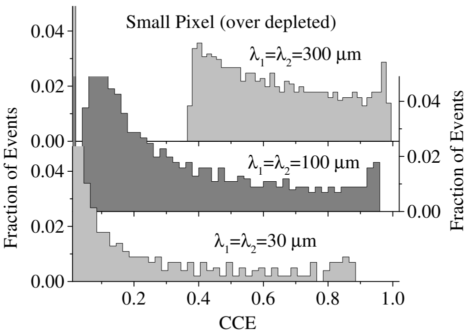

(f) Pulse height spectra for the small pixel, over depleted.

Figure 6.17: Pulse height spectra of the different sized pixels for various mean free drift lengths of the carriers.

The peak to background ratio in fig. 6.17 is lower for smaller pixels due to the fact that proportionally less events contribute to the maximum signal.

6.2.6 Résumé

Three effects in semiconductor detectors were investigated on the basis of simulations and analytical calculations. If the mean free drift length of the carriers are not sufficient to give full collection, then charge sharing can occur with neighbouring pixels, both as a positive and negative signal.
It was demonstrated how the pixel size and bias condition effect the performance of unipolar detectors. The small pixel effect was studied for various mean free drift lengths, showing the improved spectral performance with decreasing pixel sizes.
All the above results assume that the charge integration time does not influence the output signal (no ballistic deficits) and that de-trapping does not contribute to the signal (de-trapping time $\gg$ shaping time).

Chapter 7

Active Pixel Detector for Ion Beam Profiling

This chapter describes a detector for ion beam profiling and discusses experimental results obtained in two different implanters. The signal measured by the graphite detector is the charge carried by the ions in the beam. Other than the previously discussed detectors, the sensor is made of graphite and the interaction of the ions with the graphite have deteriorating effects (secondary electron emission). Of interest is the ion current (number of ions arriving in time) which is given purely by the positive charge carried by the ions. When these are absorbed in the graphite they charge up the graphite which allows the measurement of the ion beam current.

7.1 Introduction

This chapter describes a very different system to the ones discussed previously. The detector, however, uses the read out technology developed for X-ray pixel detectors. One of the capabilities of semiconductor X-ray pixel detectors is the parallel sampling of a lot of channels (up to several thousand) at high speed (image acquisition time < 1 ms). A read out chip, based on the integrating method, proves to be applicable to this very different field of ion beam profiling[1]. The aim here is to measure the current, spatial distribution and time evolution of an ion beam.
With increasing device density in silicon technology, tighter control of process parameters are required [SIA97]. Non-uniform implants in silicon processing can decrease the yield of useful devices, so accurate knowledge of the implanter's performance is very desirable. Commonly employed profilers use Faraday cups or wires to scan the beam. By swinging a lever with several Faraday cups through

[1] The idea and proposal were put forward by Mahfuzur Rahman, Dept. of Physics and Astronomy, University of Glasgow, G12 8QQ, Scotland UK.

the beam, the beam current is measured and some information on the beam profile is gained. Such a system is not "real time". In situ measurement can be achieved by moving two wires, at right angles to each other, through the beam. The information retrieved in such a way is limited and no accurate beam profile can be acquired.
In the following a prototype graphite pixel detector is described, which allows real time acquisition of the ion beam current and profile. An ASIC pixel chip used for the read out was designed at Mitthögskolan, Sweden [MHSe].
This read out chip was initially designed for X-ray imaging and has been modified to suit the special requirements for the application described here. The pixel inputs were changed to allow wire bonding which allows the separation of the electronics from the sensor. Test results with the very low energy ion implanter at the University of Salford [Bou91],[Orr91] and the implanter at the University of Surrey [Sur] are presented.

7.2 Experimental Setup

7.2.1 Design Considerations

The detector must be mounted inside a vacuum, so an interface to the air side is necessary. It was chosen to mount the read out electronics on the air side to allow easy access and to avoid contamination of the implanter. A multi-pin feed-through connects each pixel from the detector to an input on the read out. The high-end output is sampled with a PC based National Instruments ADC card which is addressed with LabView software.
Tests were carried out at the implanter at the Universities of Salford and Surrey. Both beams were $^{40}Ar^{+}$ ions, the energy was 10 keV at Salford and varied at Surrey (60, 80 and 100 keV).

7.2.2 The Graphite Detector

High density graphite is suitable as a detection material in ion implanters since it has a low sputtering yield and a high thermal and electrical conductivity. The ions absorbed in the graphite deposit their charge which is measured by the read-out electronics. The tested device has cylindrical graphite pixels mounted on a graphite back plane. A photograph of the detector is shown in fig. 7.1. A simple design is used for the prototype detector. The pixel diameter is 8 mm, the backplane is 50 mm by 50 mm in size, the side walls are 10 mm thick. Each pixel and the back plane are connected with kapton coated wires to a pin of the feed-through on the flange, as shown in fig. 7.2. Commercial implanters need smaller pixels and a larger detector area. Applied Materials require a pixel pitch of around 7 mm and an active area of 20 cm by 20 cm for their machines [AM00].
The tested device was designed for a "proof of principle". The current sensor is

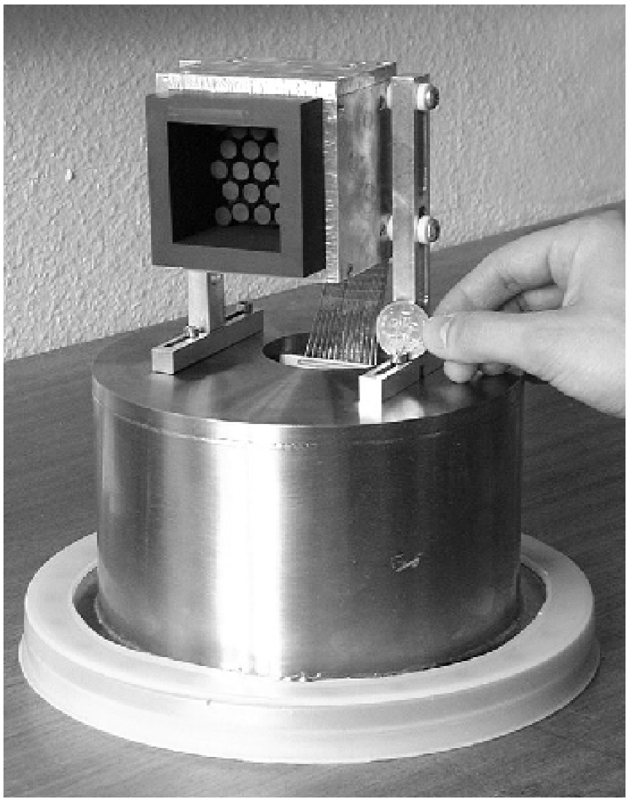

Figure 7.1
Photograph of the graphite detector mounted to the flange, as used for the Salford machine.

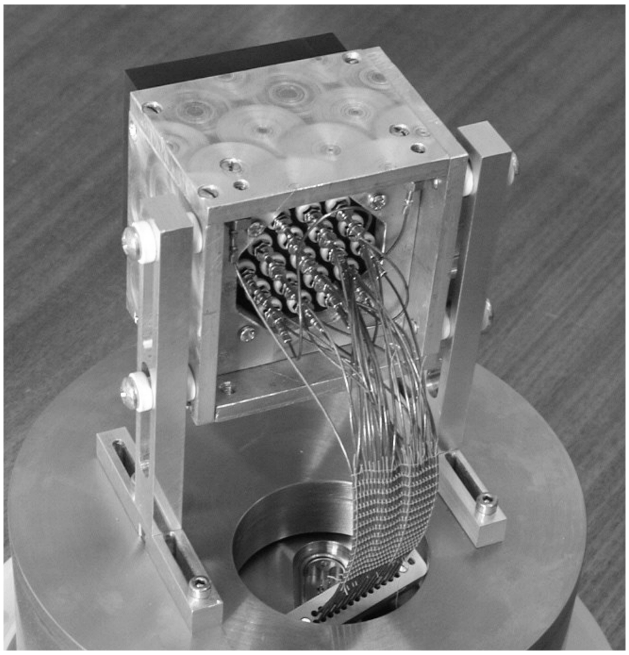

Figure 7.2
Photograph of the back of the detector, each pixel is separately wired to a pin on the feed-through.

not cooled; no magnetic field is present around the detector, so secondary electrons are lost unless they are collected by the side planes.

7.2.3 The Electronics

Tests were carried out with two sets of read out electronics. The first uses discrete components as current to voltage converters with 100 kΩ feedback resistors. The 16 channels are processed in parallel on a 16-channel ADC card. The frame rate is about 7 Hz, limited by the ADC card and the software. This read out was only used for the initial tests at Salford.
The second read out uses a 100 pixel charge integrating ASIC chip[2] designed under Europractice [EuPr]. Each pixel contains a current mirror to decouple the input from the capacitor charge and provides a gain of 0.5 to allow higher currents. The capacitors are specified at 0.5 nF and are externally gated to control the dynamic range and adjust for the beam current. The read out is non-destructive, the reset is applied globally. The circuit diagram for one pixel cell is shown in fig. 7.3. The current, if not integrated onto the capacitor, is added on a summation node. A

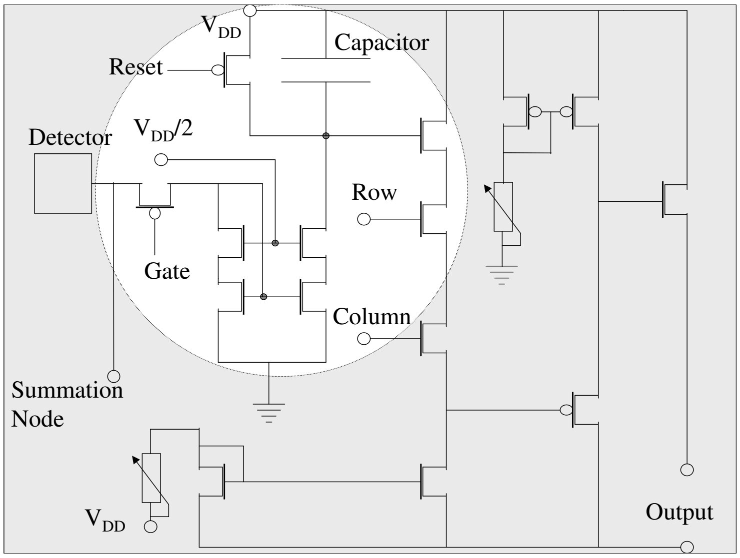

Figure 7.3: Circuit diagram of each pixel cell on the 100 pixel read out chip.

photograph of part of the ASIC is shown in fig. 7.4. The capacitors cover most of the pixel area which is 500 x 500 μm^2.

[2]The chip was designed by Munir Abdallah, ITE Dept., Mid Sweden University, SE-851 70 Sundsvall.

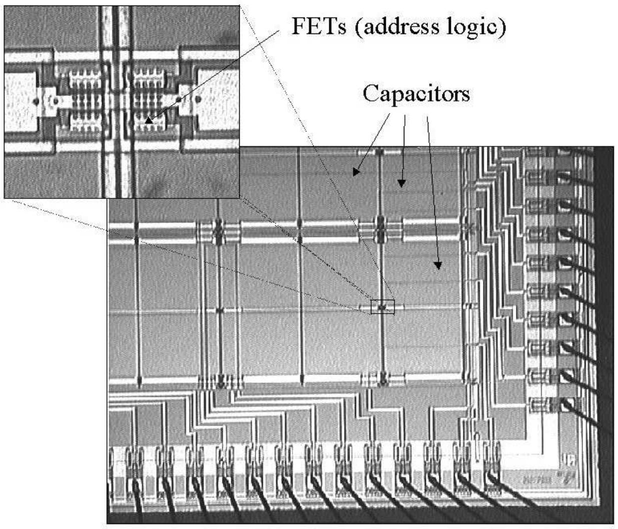

Figure 7.4: Photograph of part of the ASIC showing the bond pads and several pixels. The capacitors cover most of the pixel area.

The ASIC is mounted on an interface board[3], which links the detector to the PC.

7.3 Measurements

7.3.1 Calibration

The simple read out using the discrete components, shows a uniform behaviour for all pixels (uniformity better than 0.1 %). The performance was measured with a current source, the response is linear over a dynamic range $> 10^3$. The ASIC chip was similarly tested with a current source, the response of a pixel receiving 6 μA input current is shown in fig. 7.5. The exposure time is 1 ms. A line was fitted to the data in the range of 0.1 ms and 1.0 ms, which shows a linear response with a maximum deviation of around 3 %. The exposure time is set according to the expected current of around 5 μA per pixel. The input-output characteristics for an exposure time of 1 ms are shown in fig. 7.6. The system response is linear for input currents between 1 μA and 6 μA. The chip shows some variation between pixels (standard deviation $\sigma = 12$ %). A gain map was used for compensating the differences. Since the output is offset (by about 3 V), see fig. 7.5 and 7.6, the gain variation can be adjusted by the formula (offset-signal)/(offset-calibrate), where

[3]The interface boards and main parts of the software were designed by Julien Marchal, Dept. Physics and Astronomy, University of Glasgow, G12 8QQ, Scotland UK.

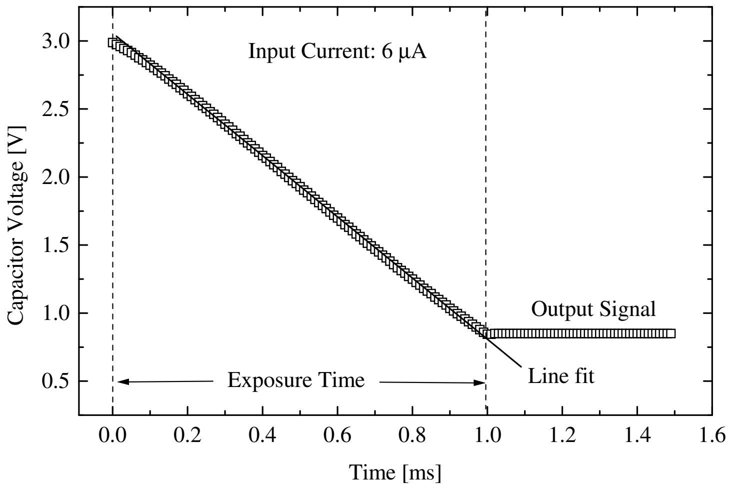

Figure 7.5: Response of a pixel receiving 6 μA input current with an exposure time of 1 ms. After an initial deviation ($\approx$ 0.1 ms) the response is linear. The line was fitted between 0.1 ms and 1.0 ms.

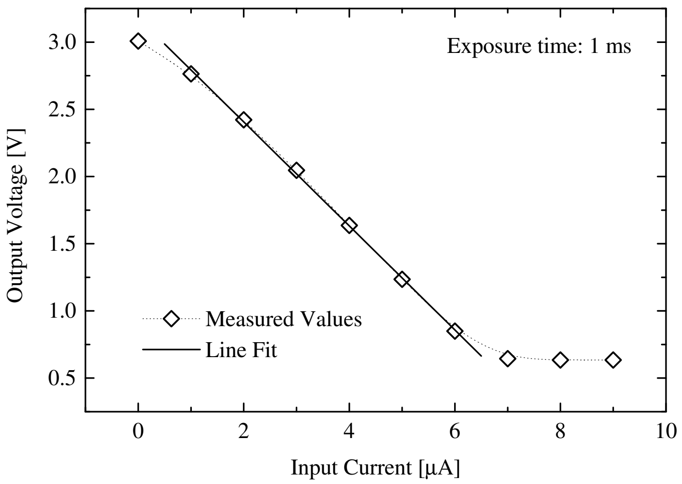

Figure 7.6: Input-output characteristic for 1 ms exposure time. The response is linear for input currents between 1 μA and 6 μA.

the calibrate signal provides the information on the gain of each pixel.

7.3.2 Tests at the Implanter in Salford

The measurements were done at the very low ion beam facility at Salford University. In order to use both read out electronics only 16 channels (pixels) were connected. The beam current was first measured using a standard Faraday cup. This was then replaced with the graphite pixel detector. No beam parameters were changed so the beam current is expected to be similar to what was measured with the Faraday cup. This allows a rough estimation of the accuracy of the current measured with the graphite pixel detector.
The first 60 seconds of the current measurement performed with the simple circuit are shown in fig. 7.7. (The beam is turned on after about 5 seconds.) The beam

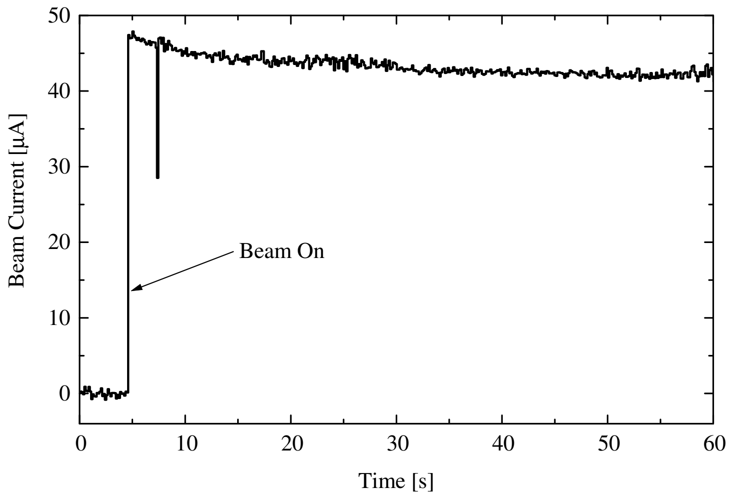

Figure 7.7: Current measured with the graphite pixel detector. The ion beam was turned on about 5 s after the start of the acquisition.

current is expected to be around 50 μA. The measured values converge to 43 μA. For the 100 pixel integrating chip, the summation node for the overall current measurement was not sampled, so only the profiling properties were investigated. Due to the limited size of the detector, the beam was focussed (this increased the current to around 70 μA). The ion beam was then scanned across the detector. A sequence of images of the beam at various positions is shown in fig. 7.8. These data were taken with the ASIC read out. The images show the beam moving across the detector from left to right. A full period of the beam scan included the beam moving back to its initial position. Fig. 7.9 shows the ion beam current measured

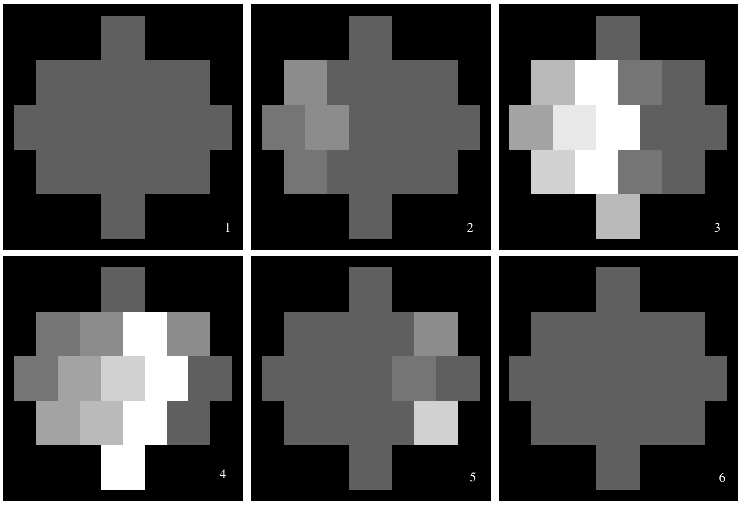

Figure 7.8: Sequence of images showing the ion beam moving across the graphite detector. The data were taken with the ASIC chip.

in time. The two current peaks correspond to the beam being swept from one side of the detector (left peak) to the other (right peak). Accordingly the peaks are expected to have a mirror symmetry around the turning point of the beam. This behaviour is seen in fig. 7.9, the time axis is offset with respect to the beam movement.
From the signal on individual pixels the beam speed can be derived, it was measured to be (4.8 ± 0.4) cm/s. The measured beam profile is oval shaped, roughly 10 cm in height and 4 cm wide.

7.3.3 Tests at the Implanter in Surrey

The measurements at the implanter in Surrey were all performed with the ASIC read out. The data acquisition was improved (new DAQ hardware and software) allowing a frame rate of up to about 45 Hz. The summation node was sampled after each image acquisition, giving a measurement of the overall current on the detector.
The initial tests described above seem to confirm the feasibility of using the detector for ion beam profiling. However, a major issue which has not been addressed is the emission of secondary electrons. Due to the large beam size and only very rough knowledge of the beam current, any effects of secondary electron emissions are not seen. The advantages of the implanter at Surrey are the ability to focus the beam onto a single pixel and the independent measurement of the beam current

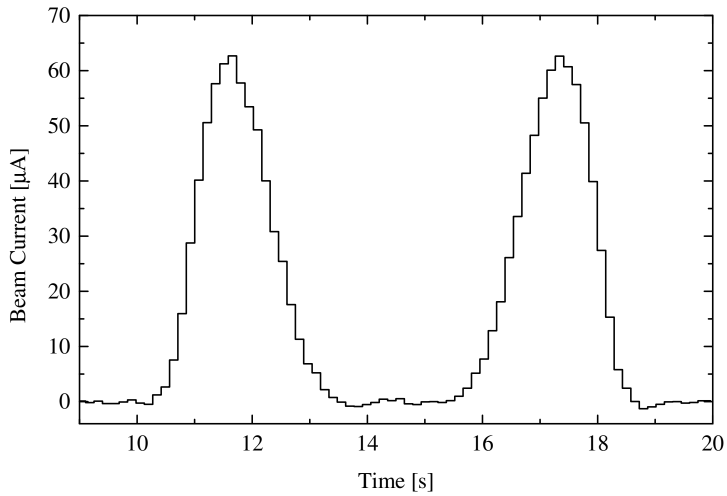

Figure 7.9: Beam current measured while sweeping the beam across the detector. The two peaks correspond to the beam moving from one side to the other and back again.

while the detector is in place. The focusing of the beam on a single pixel is shown in a sequence of images in fig. 7.10. The focussed beam was then swept across the centre five pixels. Fig. 7.11 illustrates the scans of the beam across the detector. The lower scan, across the centre of the detector, corresponds to the data shown in fig. 7.12 and fig. 7.13. A sequence of images taken from the upper scan is shown in fig. 7.14. The current is sampled from the summation node between frames. The overall beam current measured with the detector includes all the pixels and the backplane with the side walls. The current measured for the scan across the centre of the detector is shown for three different ion energies in fig. 7.12. The current measured with a Faraday cup was 11 ± 2 μA. The measured beam current with the detector was significantly higher as seen in fig. 7.12. The variations in the current follow the detector profile. This was used to scale the distance axis. Secondary electrons which are lost increase the measured current. Where the beam passes next to a pixel onto the back plane, secondary electrons are more likely to be picked up by the pixel and the excess in the measured current is not as severe. Since the side walls are significantly higher than the pixels (5 cm vs. 2 cm), less secondary electrons escape at the sides than in the centre of the detector.

The signal acquired on each of the five pixels and the back plane are shown in fig. 7.13(a)-7.13(f). The acquired raw data are voltages sampled with the ADC card, due to the gain map corrections the plotted values are not the direct outputs of the chip and therefore no units are given in fig. 7.13. The background in

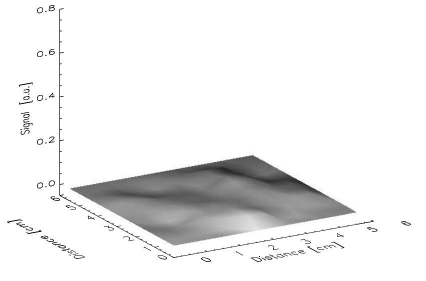

(a) Plot of the unfocused beam, showing a low signal across the detector.

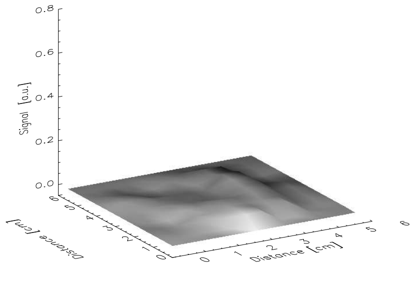

(b) Plot of the beam profile 2 s after the start of the focusing

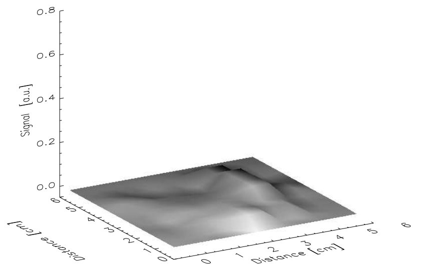

(c) Plot of the beam profile 4 s after the start of the focusing.

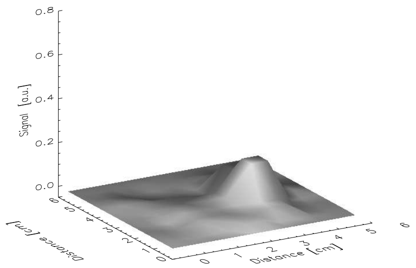

(d) Plot of the beam profile 6 s after the start of the focusing.

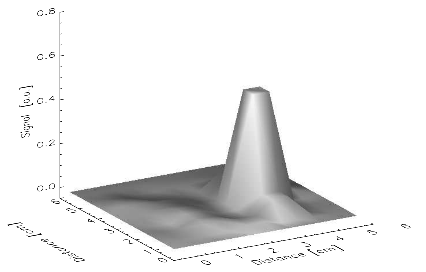

(e) Plot of the beam profile 8 s after the start of the focusing.

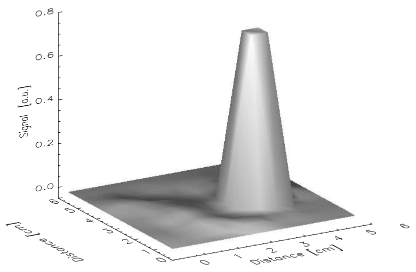

(f) Plot of the beam focussed on a single pixel.

Figure 7.10: Sequence of images showing the focusing of the beam onto a single pixel.

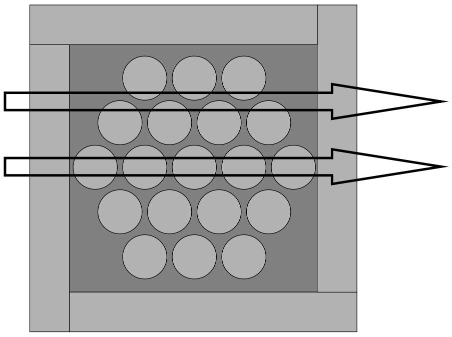

Figure 7.11
Illustration of the scans across the detector. The lower scan corresponds to the data plotted in fig. 7.12 and fig. 7.13. The data from the upper scan is plotted in the sequence of images in fig. 7.14.

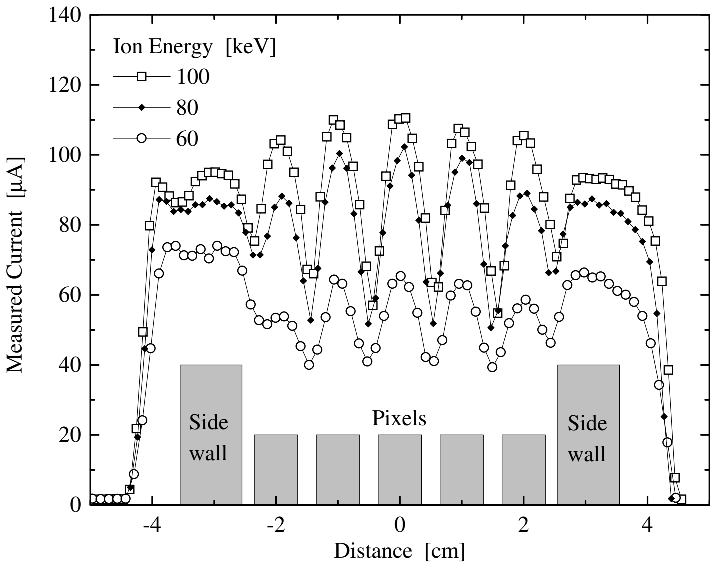

Figure 7.12: Overall measured beam current as the beam is swept across the centre of the detector. The beam current measured with a Faraday cup was 11 ± 2 μA. The excess and variations in the measured current are due to secondary electron emission.

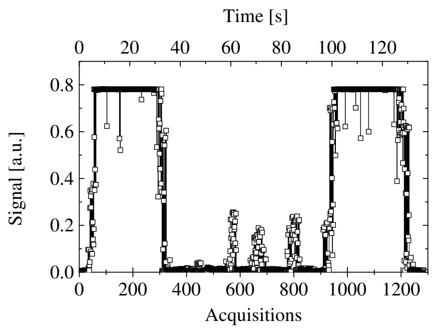

(a) Signal measured on the back plane as the beam is swept across the centre of the detector.

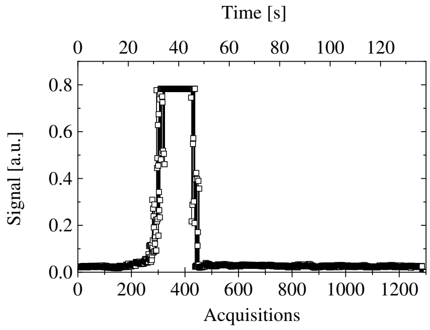

(b) Signal measured on the far left pixel as the beam is swept across the centre of the detector.

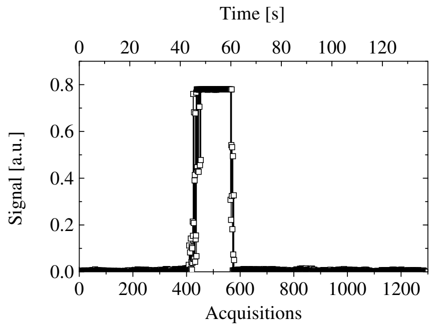

(c) Signal measured on the medium left pixel as the beam is swept across the centre of the detector

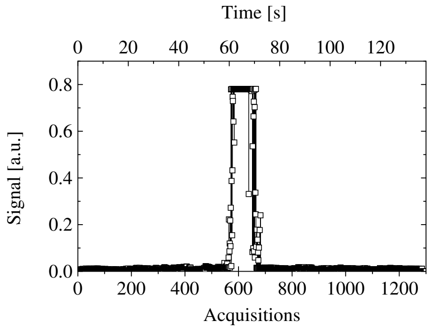

(d) Signal measured on the centre pixel as the beam is swept across the centre of the detector

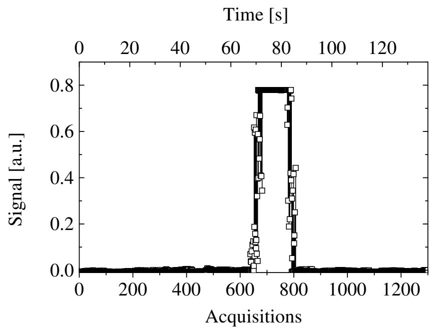

(e) Signal measured on the medium right pixel as the beam is swept across the centre of the detector.

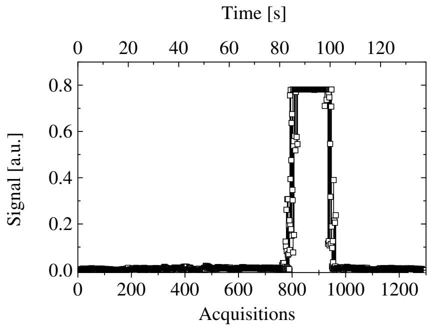

(f) Signal measured on the far right pixel as the beam is swept across the centre of the detector.

Figure 7.13: Pulse height spectra of the different sized pixels for a unipolar detector.

fig. 7.13(a) shows the profile of the detector, where the side walls are hit all the current is received by back plane. While the pixel gaps are also seen, the received current is lower due to the size of the beam which is still partly illuminating the pixels. These "switch on" as expected when the beam passes over them.
The difference between fig. 7.12 and fig. 7.13 is that in the first case the current is measured from the summation node, whereas in the latter case the data are the signals from the individual pixels. The frame rate in fig. 7.13 is 9.5 Hz due to a time delay added by the software in order to limit the amount of data acquired ($\approx$ 15 kB/s at maximum rate).
The number of acquisitions per pixel varies in fig. 7.13, the centre pixel being narrower than the outer ones. This is because the step size of the beam is not constant: the beam sweeps faster across the centre than the edges.
A scan between two rows of pixels, as illustrated in fig. 7.11, is shown in fig. 7.14. The beam can be seen to pass from the left to the right hand side illuminating the

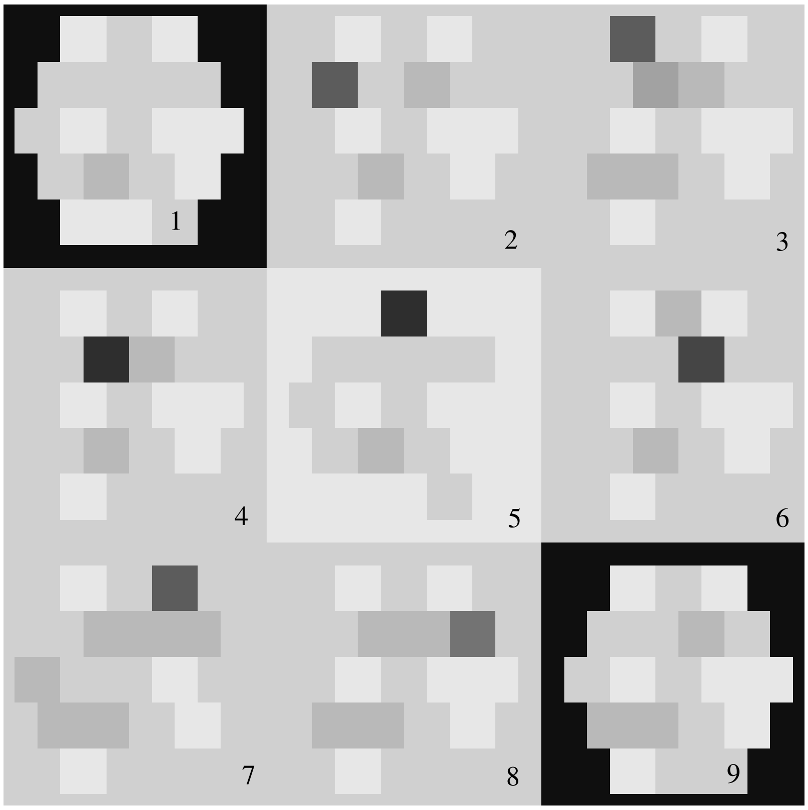

Figure 7.14: Sequence of images showing the beam sweeping across the detector, between two rows of pixels.

pixel from the lower and upper row as it passes across them.

7.4 Conclusions and Future Work

A graphite pixel detector has been successfully tested as an ion beam profiler in two implanters at the Universities of Salford and Surrey. Real time beam profiling was demonstrated. Effects of secondary electron emission were investigated for different beam energies showing an increase for higher ion energies. Quantitative investigations of secondary electron emissions are planned with the next iteration of the detector.

The development of a new graphite detector is underway. The number of pixels will be increased to 400, their size reduced to 4 mm (5 mm pitch). This detector should give sufficient spatial resolution over an area of 10 cm^2. A new version of the ASIC is planned. The main modification is an adjustable gain on each pixel which allows adjustment on the hardware for any variation between pixels. Additionally pixels can then be set to be sensitive to a different current range, allowing a higher dynamic range of the overall system.

7.5 Acknowledgements

This work has been possible only due to the input of a number of people. Some have been mentioned, such as the project leader Mahfuzur Rahman, the chip designer Munir Abdallah and my colleague Julien Marchal with whom the test were performed. I would also like to thank the physicist running the implanters, which are Jaap Van den Berg at Salford and Ahmed Nejim at Surrey, for their time and help with the experiments.

Summary

Three detector systems were investigated, namely two hybrid semiconductor X-ray pixel detectors and a graphite pixel detector for ion beam profiling.
The ERD1 (**E**nergy **R**esolving **D**etector) is designed for room temperature X-ray spectroscopy. It was characterised with laboratory X-ray sources in the energy range between 6 and 60 keV and at the Daresbury synchrotron radiation source of the CLRC. The ERD1 uses an array of 16 by 16 pixels. This allows the coverage of a larger area ($\approx 1/4$ cm^2) without increasing capacitive noise and also increases the rate capability. The 256 pixels show some variation in their gain and offset. It was shown that these variations can be accurately compensated by correcting for the differences in gain and offset for each pixel. Images of diffraction lines and pulse height spectra from a $KNbO_3$ crystal were simultaneously acquired at the synchrotron radiation facility in Daresbury. The energy spectra show the primary beam energy and the Nb fluorescence at an energy of 16.6 keV. The spectral performance was investigated with laboratory X-ray sources, from which the electronic noise was determined to be 227 ± 43 eV.
A quantitative evaluation of charge sharing was achieved for the ERD1, which has a pixel size of 300 x 300 μm^2. Single, double and treble clusters were investigated. It was shown that treble clusters are negligible, but that double clustering is of the order of several % (up to about 10 %) depending on the X-ray energy and the energy threshold set for charge sharing. The energy dependent study of these effects showed that the dominant contribution to charge sharing is diffusion rather than the range of the photo-electron. A simple model was proposed on the basis of which the average charge cloud distribution was extracted.
The LAD1 (**L**arge **A**rea **D**etector) is designed for X-ray imaging, primarily for applications in synchrotron radiation sources. A single chip module (64 by 64 array of 150 μm square pixels) was characterised at the synchrotron radiation source in Daresbury. The spatial resolution was studied on the basis of the LSF and MTF and was determined to be (5.1 ± 0.1) lp/mm. Theoretical derivations of the spatial resolution for pixel detectors lead to an analytical expression which allows the calculation of the spatial resolution as a function of the pixel size, predicting a resolution of 5.3 lp/mm for the LAD1. The image noise was studied both experi-

mentally and theoretically. It was shown that for a single photon counting system, such as the LAD1, the noise should be given by Poisson statistics. This prediction was confirmed with measurements performed with the LAD1. The rate capability was experimentally determined to be about 250 k counts per pixel per second. A simulation of the paralysis of the read out at high rates related the maximum rate to a shaping time of around 1.7 μs.
Miscellaneous studies relevant to semiconductor pixel detectors were carried out experimentally, theoretically and on the basis of simulations. The difference in contrast between ideal single photon counting and charge integrating imaging detector was derived theoretically and measured experimentally with the ERD1. It was shown that the contrast of an object depends on the background absorption in the region of the object. The conventional definition of contrast, (background-signal)/background), led to the conclusion that, in some cases, the ideal photon counting system will give a better contrast than the ideal integrating device.
The small pixel effect was studied on the basis of simulations and analytical calculations. The drift and weighting fields and potentials were simulated in MEDICI and were used to calculate the charge collection efficiency as a function of the mean free drift lengths of the charge carriers. Charge sharing due to carrier loss was studied for different mean free drift lengths and related to interaction points in the detector. The usefulness of unipolar sensing in materials with very different mean free drift lengths for electrons and holes was illustrated for different biasing conditions and pixel sizes. The small pixel effect was investigated for various mean free drift lengths of the carriers and two different bias conditions. It was illustrated how the charge collection efficiency of the photo peak is increased by reducing the pixel size.
The third pixel detector was designed for ion beam profiling. This graphite pixel detector uses the modified read out electronics of a charge integrating ASIC, initially designed for X-ray imaging. This system was successfully operated in two implanters at Salford and Surrey Universities. Real time beam profiling with a frame rate of up to 45 Hz was demonstrated. The system acquired the beam profile and current for different beam energies. Effects of secondary electron emission could be studied by scanning the ion beam across the detector. The results from this prototype system achieved the desired "proof of principle" and has led to the continuation of this work for a second iteration of the detector and read out.

Appendix A

Software for the Data Analysis

All programs were written in LabView. The read out of the ERD1 and ion beam detector is purely based on LabView, primarily for reasons of compatibility with the DAQ cards. For convenience the data analysis software was also written in LabView.
Although the data acquisition of the LAD1 is based on C^{++} and IDL [IDL], the data are saved in a binary format which can be loaded in LabView.
Several programs were written for various, mainly minor tasks such as displaying images and spectra, or selecting the data for the charge sharing. The only two programs to be mentioned here are the software for the adjustment of the pixel to pixel gain and offset variations (ERD1) and for the calculation of the LSF and MTF (LAD1).

A.1 Software for the Adjustment of the Pixel Variation

The software for the adjustment of the variation among pixels includes:

Part1:

1. Selection of the pixel data
2. Histogramming the data for each pixel
3. Selecting the region(s) of interest (ROI)
4. Fitting a Gaussian curve to the peak(s)

Part2:

5. Taking the peak position and performing a linear fit to the data for the 256 pixels (calibration).

6. Using the complete calibration data to adjust any data set for variations among pixels.

For the normal acquisition mode the data written to file is a set of two columns, the first giving the analogue value of the signal in volts, the second the address of the pixel hit. The first step outputs a matrix of 256 columns, (one for each pixel), where the row number is given by the maximum counts a pixel received and the contents are the analogue values of the pixel signals. For the next step a histogramming subroutine was written, as all which were recently available were not considered adequate[1].
In order to allow accurate and fast fitting the initial values of the fit parameters are calculated from the data. The first derivative of the histogram, an example

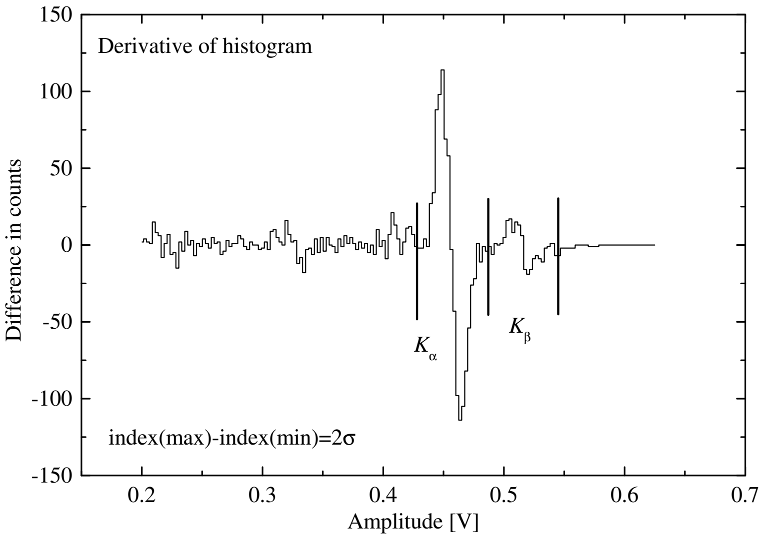

Figure A.1: Example of the first derivative of a histogram. The maximum and minimum give the initial value of the standard deviation σ.

is shown in fig. A.1, has a maximum and minimum at one σ from the centre of the peak. This value of σ is used to calculate the ROI and as initial value for

[1] When histogramming the bin size should be matched to that of the data (ADC binning) in order to avoid erroneous spikes in the pulse height spectra.

the Gaussian fit. The centre of the peak x_0 is calculated from the five bins with the highest counts; the area is estimated from the peak height and the number of counts in the ROI. A least-squares method is used for fitting, the minimisation of the χ^2 is done numerically.
The result of a fit is shown in fig. A.2. The errors are derived from the χ^2. All

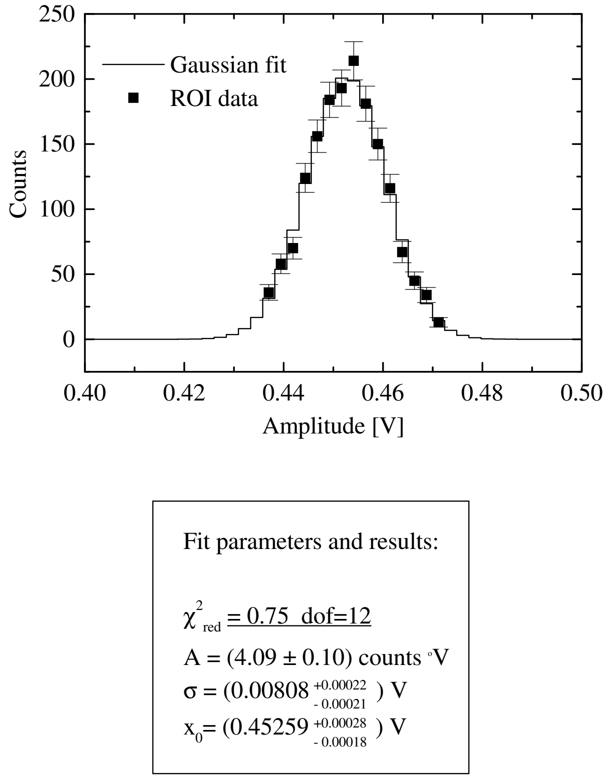

Figure A.2: An example of a fitted Gaussian curve plotted with the experimental data in the ROI.

results of a fit are written to file for the 256 pixels. These data are then used to calibrate each pixel, i.e. fit a linear curve to the peak position vs. peak energy. This fit is calculated since the χ^2 can easily be minimised analytically [Bar89]. The fit parameters are then used to convert the output voltage of a pixel to an energy. Since this is performed for each pixel individually, any variations among pixels are adjusted.

A.2 Software for the Calculation of the LSF and MTF

The data containing the information on the LSF is a matrix, each cell containing the value of the signal acquired from the corresponding pixel. In the case of the LAD1 the data were taken with a threshold scan, so a 3-dimensional matrix is acquired, the third dimension corresponding to the threshold. So an initial choice of the desired threshold is necessary which returns the matrix containing the image of the slit. The following calculations are then performed:

Part1: LSF

1. Selection of the data for a line fit.
2. Fitting a line, extracting the position and angle of the slit.
3. Selecting the data of interest.
4. Adjusting the data according to the position and angle of the slit.

Part2: MTF

5. Fitting a function to the LSF data (optional).
6. Fourier transforming the LSF.

The first two steps are vital, if the line fit is inaccurate the LSF width is erroneously increased. A set of pixels (typically equal to the number of pixels in a row) is selected according to their signal height. A line fit is performed and the position of the selected pixels with respect to the line is evaluated. Any pixel which lies beyond a certain distance from the line (typically three pixels) is assumed to be noisy and is discarded. A second line fit is then performed which is assumed to be accurate (insufficiencies in this part can only lead to poorer resolutions).
The data of interest are selected according to their distance from the slit. Only a few pixels per column or row are significant for the LSF (if all the pixels are included the background counts will give rise to errors in the MTF). This choice of the region of interest is related to the truncation error. Once the data of interest are selected, they are adjusted according to the parameters from the line fit. Any overall background can be subtracted, if present. The LSF is then directly transformed giving the MTF.

Appendix B

Comments on the Weighting Field

The concept of the weighting field and potential was introduced in the theory chapter in section 2.3. There has been some controversy over the following question: Is the weighting field purely a geometrical factor (derivable from the Laplace equation) or must the space charge be taken into account (necessity of using the Poisson equation)?
Throughout this work it has been assumed that Poisson's equation is required to calculate the correct weighting field. Section 6.2 which was concerned with the small pixel effect clearly made use of the Poisson equation (otherwise there would be no difference in the weighting fields for different bias conditions). Also the derivation in the theory chapter (section 2.3) included the space charge. This is justified in the following.

The most convincing reason is that the experimental data supports the use of Poisson's equation and disagrees with a purely geometrical weighting field.
A good Si detector will have virtually 100 % CCE. If this detector is only partly depleted, then according to the Laplace equation some of the weighting field will be in a region which is inactive (very low drift field). So any charge generated in the depleted region will drift until it either reaches the contact or the low field region. According to Laplace's equation the CCE is then less than 100 % because the weighting field in the inactive part has not contributed to the signal.
Fig. B.1 shows the peak positions of the Ag K_α and K_β lines as a function of the reverse bias voltage[1]. A similar measurement is to plot the CCE of minimum ionising particles (MIPS) as a function of the depletion width. Such data is given in ref. [Bea98] and the CCE shows a linear dependence on the depletion width. So any charge generated in the depleted region is *fully* collected, which is in support

[1]These data were provided by Keith Mathieson, University of Glasgow, G12 8QQ Scotland UK.

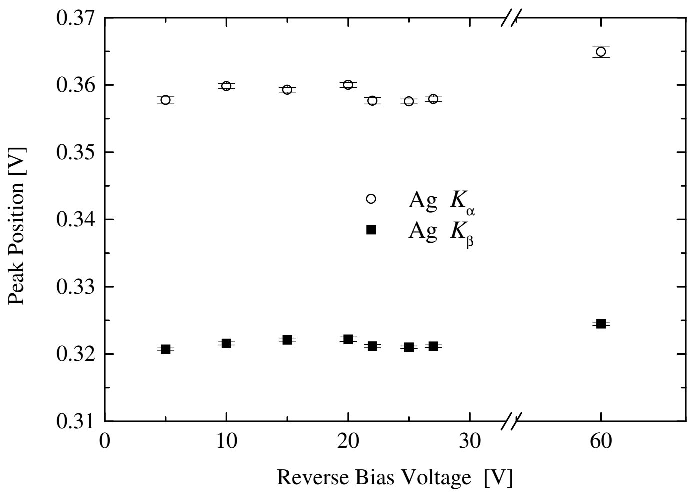

Figure B.1: The peak positions of the Ag K_α and K_β lines are plotted as a function of the reverse bias voltage. There is no significant decrease of the CCE at low bias voltages. The weighting field is therefore not correctly predicted by using Laplace's equation.

of Poisson's equation.
If considering Poisson equation, the weighting field is the normalised field (which is calculated by applying the bias voltage to the pixel of interest and dividing the acquired field by the applied voltage). The weighting field is always concentrated in the active region of the detector. The above experimental results agree with this[2].
If the weighting field were purely geometrical then the CCE for the spectra in fig. B.1 would decrease with decreasing depletion width (the detector is fully biased at around 35 V). Part of the weighting field would be in the inactive region and the CCE should be correspondingly less. Accordingly the MIP data would show a CCE proportional to the square of the depletion width, assuming a constant weighting potential. So the experimental data disagree with a weighting field derived from the Laplace equation and are strongly supporting the use of Poisson's equation.
Additionally a purely geometrical weighting field violates energy conservation. This follows directly from the derivation in section 2.3.

[2]It is important to note that the shaping time will eliminate any slow signal (in the order of μs or longer) for the ERD1. The same is true for the data presented in ref. [Bea98].

Bibliography

[Ali80] R. C. Alig, S. Bloom, C. W. Struck, “Scattering by ionization and phonon emission in semiconductors”, Phys. Rev. B, Vol 22, no. 12, (1980).

[Ame72] Amersham (The Radiochemical Centre), Data sheet 11162 for “Variable energy X-ray source, code AMC.2084”, (1972).

http://www.amersham.co.uk/

[AM00] Applied Materials Limited, Implant Division, Foundry Lane, Horsham, West Sussex RH13 5PY England, Personal Correspondence, April (2000).

[Bar89] R. J. Barlow, “Statistics”. John Wiley & Sons Ltd, (1989).

[Bea98] L. Beattie et al., “Charge collection efficiency in heavily irrdatiated silicon diodes”, Nucl. Instr. Meth. A 412, pp. 238-246, (1998).

[Ber99] G. Bertuccio et al., “Integration of Front-End Electronics with GaAs Pixel Detectors: experimental and feasibility analysis”, IEEE Trans. Nucl. Sci., 46, pp. 1209-1214, (1999).

[Bou91] A. Bousetta, J. A. van den Berg, R. Valizedah, D. G. Armur, P. C. Zalm, “Ultra low energy (100 - 2000 eV) boron implantation into crystalline and silicon-preamorphized silicon.” Nucl. Instr. Meth. Phys. Res. B 55, p. 565 (1991).

[Bro79] Bronstein, Semendjajew, “Taschenbuch der Mathematik” Verlag Harri Deutsch, p. 671 (1979).

[Cav63] G. Cavalleri, G. Fabri, E. Gatti, V. Svelto, “On the induced charge in semiconductor detectors”, Nucl. Instr. Meth. 21, pp. 177-178, (1963).

[Cav71] G. Cavalleri, G. Fabri, E. Gatti, V. Svelto,“Extension of Ramo’s theorem as applied to induced charge in semiconductor detectors”, Nucl. Instr. Meth. 92, pp. 137-140, (1971).

[Doi72] Kunio Doi, K. Strubler, "Truncation error in calculating the MTF of radiographic screen-film systems from the line spread function" Phys. Med. Biol., Vol. 17, No. 2, p. 241 (1972).

[Dys90] N. A. Dyson, "X-rays in atomic and nuclear physics", 2nd edition, Cambridge University Press, (1990).

[EuPr] Europractice, Homepage: "http://www.europractice.com/index.html".

[Fie00] M. Fiederle et al., "CdTe and (Cd,Zn)Te as detector materials", Nucl. Instr. Meth. A, proceedings of the '2nd international workshop on radiation imaging detectors', submitted (2000).

[Fer86] R. Fernow, "Introduction to experimental particle physics", Cambridge University Press, (1986).

[Fir96] R. B. Firestone, V. S. Shirley, "Table of Isotopes", John Wiley & Sons, Inc. (1996).

[Fro98] C. Fröjdh, P. Nelvig "Performance criteria for x-ray imaging sensors" Physica Medica, Vol XIV, Suppl. 2, (1998).

[IDL] **I**nteractive **D**ata **L**anguage, is a trademark of Research Systems Inc., Homepage: "http://www.rsinc.com".

[IC86] "Modulation Transfer Function of Screen Film Systems" ICRU Report 41, (1986).

[Kim91] H. Kim, H. S. Min, T. W. Tang, Y. J. Park,"An extended proof of the Ramo-Shockley theorem", Solid State Elec. Vol. 34, No. 11, pp. 1251-1253, (1991).

[Kno00] G. F. Knoll, "Radiation Detection and Measurement", 3rd edition, John Wiley & Sons, Inc., (2000).

[Kra88] Kenneth S. Krane, "Introductory Nuclear Physics", John Wiley & Sons, Inc., (1988).

[Lau95] S. Lauxtermann, "Integrierte GaAs MODFET Elektronic zur Auslese von Strahlendetektoren", Inaugural-Dissertation, Albert-Ludwigs Universität Freiburg, (1995).

[Lec96] P. Lechner, et al., "Pair creation energy and Fano factor of silicon in the energy range of soft X-rays", Nucl. Instr. Meth. A 377, pp. 206-208, (1996).

[Lec01] P. Lechner, et al., "Silicon drift detectors for high count rate X-ray spectroscopy at room temperature", Nucl. Instr. Meth. A 458, pp. 281-287, (2001).

[Lit97] A. M. Litke, “An advanced pixel detector”, Nucl. Instr. Meth. A, 386, pp. 167-171, (1997).

[Luk00] P. N. Luke et al., “Noise in CdZnTe Detectors”, NSS-Lyon, Trans. Nucl. Sc., IEEE, submitted Oct. (2000).

[Lut99] G. Lutz, “Semiconductor Radiation Detectors”, Springer Verlag, (1999).

[Lor88] P. Lorrain, D. Corson, F. Lorrain, “Electromagnetic Fields and Waves”, 3rd edition, W. H. Freeman and Company, (1988).

[NIST] NIST, “National Institute for Standards and Technology” (USA), Internet page: http://physics.nist.gov/PhysRefData/

[Mar69] M. Martini, G. Ottaviati, “Ramo’s theorem and the energy balance equations in evaluating the current pulse from semiconductor detectors”, Nucl. Instr. Meth. 67, pp. 177-178, (1969).

[Mat01] K. Mathieson, “Modelling Semiconductor Pixel Detectors”, PhD thesis, University of Glasgow, G12 8QQ Scotland UK, (2001).

[McG94] D. S. McGregor et al., “Evidence for field enhanced electron capture by EL2 centers in semi-insulating GaAs and the effect on GaAs radiation detectors”, J. Appl. Phys. 75 (12), June (1994).

[MED99] Medici User’s Manual, Version 1999.2, Avant Corporation, TCAD Business Unit, (1999).

[Medi2] Medipix2, Internet page: “http://medipix.web.cern.ch/MEDIPIX/”

[MHSe] Mid Sweden University, “http://www.mh.se”.

[Orr91] K. G. Orrman-Rossiter, A. H. Al-Bayati, D. G. Armur, S. E. Donelly, J. A. van den Berg, Nucl. Instr. Meth. Phys. Res. B 59/60, p. 197 (1991).

[Owe00] A. Owens et al.,“The hard X-ray response of epitaxial GaAs detectors”, Nucl. Instr. Meth. A, 442, pp. 360-363, (2000).

[Par00] K. B. Parnham, C. Szeles, “Semi-insulating CdZnTe crystals for X-ray and γ-ray detection application”, preprint submitted to Nucl. Instr. Meth. A, (2000).

[Pas98] M. S. Passmore, “GaAs resistive gate CCDs”, Diploma thesis, University of Freiburg, Germany, (1998).

[Per98] E. Pernigotti, “Comparison between integrating readout systems and single photon counting systems for digital mammography”, Physica Medica, Vol XIV, Suppl. 2, (1998).

[Rad88] V. Radeka, "Low-noise techniques in detectors", Ann. Rev. Nucl. Part. Sci., 38, pp. 217-277 (1988).

[Ram39] S. Ramo, "Currents induced by electron motion", P.I.R.E. 27, pp. 584-585, (1939).

[Rog97] M. Rogalla, "Systematic Investigation of Gallium Arsenide Radiation Detectors for High Energy Physics Experiments", Inaugural-Dissertation, Alber-Ludwigs Universität Freiburg, (1997)
Published by Shaker Verlag GmbH (1998).

[Rog99] M. Rogalla, "Formation of a quasi-neutral region in Schottky diodes based in semi-insulating GaAs and the influence of the compensation mechanism on the particle detector performance", Nucl. Instr. Meth. A, 434, pp. 44-56, (1999).

[Rho88] E. H. Rhoderick and R. H. Williams, "Metal-Semiconductor Contacts", Oxford Science Publications, p. 106, (1988).

[Sch95] T. E. Schlesinger, R. B. James, "Semiconductors for Room Temperature Nuclear Detector Applications", Semiconductors and Semimetals Vol. 43, Academic Press, (1995).

[Sel96] P. Seller, "Noise analysis in linear electronic circuits", Nucl. Intr. Meth. A, 367, pp. 229-241 (1996).

[Sel98] P. Seller et al., "Silicon pixel detector for X-ray spectroscopy", SPIE 3445, EUV, X-ray and Gamma-ray Instrumentation for Astronomy IX, p. 584, (1998).

[Sel99] P. Seller et al., "Two approaches to hybrid X-ray pixl array readout", SPIE Vol 3774, Detectors for Crystallography and Diffraction Studies at Synchrotron Sources, July (1999).

[Sel00] P. Seller et al., "Photon counting hybrid pixel detector for X-ray imaging", Nucl. Instr. Meth. A, 455, pp. 715-720, (2000).

[Sha01] K. S. Shah, "X-ray imaging with PbI_2-based a-Si:H flat panel detector", Nucl. Instr. Meth. A 458, pp. 140-147, (2001).

[SIA97] "The National Technology Roadmap for Semiconductors Technology Needs", Semiconductor Industry Association, 72 (1997).

[Spi99] H. Spieler, "Introduction to Radiation Detectors and Electronics", LBNL,
http://www-physics.lbl.gov/s̃pieler/physics_198_notes_1999/index.html, (1999).

[Spr50] K.H. Spring, "Photons and Electrons", John Wiley & Sons, Inc., (1950).

[SRS] Synchrotron Radiation Source at Daresbury, Homepage: "http://srs.dl.ac.uk".

[Sur] Ion Beam Facility at the University of Surrey, Homepage: "http://www.ee.surrey.ac.uk/Research/SCRIBA/".

[Sze81] S. M. Sze, "Physics of Semiconductor Devices", 2nd edition John Wiley & Sons, Inc., (1981).

[Tab96] T. Tabata et al., "An analytic formula for the extrapolated range of electrons in condensed materials", Nucl. Instr. Meth. B, 119, pp. 463-470, (1996).

[Tai80] W. H. Tait, "Radiation Detection", Butterworth & Co Publishers Ltd, (1980).

[Wil73] R. Williams, E. Lawson,"Formation of current pulses in semiconductor nuclear radiation detectors", Nucl. Instr. Meth. 113, pp. 597-598, (1973).

[Wit00] J. H. Wittke, "Electron interaction with matter", http://jan.ucc.nau.edu/w̃ittke/Interact.html#Effect, (2000).

[Yin90] Fang-Fang Yin, Maryellen L. Giger and Kunio Doi, "Measurement of the presampling modulation transfer function of film digitizers using a curve fitting technique", Med. Phys. 17 (6), p. 962, Nov/Dec (1990).

Index